Sea Surface Temperature and Convection in Tropical Radiative Convective Equilibrium

Brittany Dygert

A dissertation
submitted in partial fulfillment of the
requirements for the degree of

Doctor of Philosophy

University of Washington

2025

Reading Committee:

Dennis Hartmann, Chair

Cecilia Bitz

Dargan Frierson

Program Authorized to Offer Degree:
Atmospheric Science

University of Washington

Abstract

Sea Surface Temperature and Convection in Tropical Radiative Convective Equilibrium

Brittany Dygert

Chair of the Supervisory Committee:
Dennis Hartmann
Department of Atmospheric Sciences

Tropical convection has significant implications for the global climate, and it is helpful to study convection in an idealized framework. This work uses a general circulation model in tropical radiative convective equilibrium, a popular idealized framework for studying the tropics in which convection is approximately balanced by radiative cooling, to explore the interactions between sea surface temperature and convection. This work is divided into three chapters. The first chapter explores inter-annual variability in these idealized tropical model experiments and how this cycle is fueled by the coupling between sea surface temperature and convection. The second chapter focuses on how ocean heat transport could impact the climate's response to increased forcing. Finally, the third chapter explores the role of sea surface temperature and the sea surface temperature gradient in setting the vertical distribution of convection and circulation.

TABLE OF CONTENTS

Page

LIST OF FIGURES

Chapter 1

INTRODUCTION

Tropical convection is a critical piece of our climate's response to warming. It is a significant source of uncertainty under climate change and encompasses a wealth of complex phenomena from the El Niño Southern Oscillation (ENSO) to hurricanes. The interaction between sea surface temperature and convection is of particular interest. In particular, the pattern of warming in the Pacific is thought to have an effect on the global climate sensitivity and radiation budget (Dong, Proistosescu, Armour, & Battisti, 2019). This has been called the 'pattern effect on climate sensitivity'. Because observations are subject to the natural complexity and noise of our climate system, we use a general circulation model in an idealized framework to better focus on the physical mechanisms underlying these interactions. The framework we use for these experiments is global radiative convective equilibrium (RCE): a useful idealized framework in which convection is approximately balanced by radiative cooling, which is a good approximation in the tropics (Manabe & Wetherald, 1967). RCE is often used in climate models with both fixed and interactive sea surface temperatures (SST) to study convection (Wing, Emanuel, Holloway, & Muller, 2017; Bretherton & Khairoutdinov, 2015). We similarly use idealized models specifically to explore the interactions between sea surface temperature, convection, and large-scale circulation. Using this framework, this thesis is divided into chapters addressing each of the following questions:

- What are the physical mechanisms that govern the inter-annual variability of organized convection and sea surface temperature contrast in the model?
- How does ocean heat transport impact the mean climate and its response to increased forcing?
- How does the sea surface temperature distribution impact the vertical structure of the

circulation and convection?

1.0.1 Inter-annual Variability of Organized Convection

Previous studies have shown that convection tends to aggregate and divide the domain into a moist convecting region and a dry subsiding region (Wing, 2019; Wing et al., 2017). If the SST is allowed to change by introducing a slab ocean model, the circulation oscillates between a relatively disaggregated, weak SST contrast state and a high SST contrast, highly aggregated state (Coppin & Bony, 2017). We use a global climate model with no rotation, uniform insolation and a slab ocean model to investigate the mechanisms of this oscillation in Chapter 2. The frequency of the cycle between a state of organized convection and strong SST contrast and a state of relatively disorganized convection and lower SST contrast is dependent on the mixed layer depth; at the 50 m depth used in our experiments, this cycle has an interannual time scale (Coppin & Bony, 2017, 2018). This cycle is the subject of the first chapter of this work (Dygert & Hartmann, 2023). The mean state is explored in more detail in Hartmann and Dygert (2022a). This chapter seeks to show that

- Atmospheric transport from the warm region responds to the skewness of the surface temperature distribution and leads to the termination of the high SST contrast state.

- Circulation influences low cloud amount through its effect on humidity above the boundary layer.

- The inter-annual oscillation is strongest for sea surface temperatures roughly like the current tropics, and is much less for cooler or warmer climates.

1.0.2 Effects of Ocean Heat Transport

In the Tropics, divergence of ocean heat transport supports low SST in regions where it occurs, causing an increased SST contrast. This SST contrast has important effects on the tropical and global climate. In Chapter 3, we introduce fixed ocean heat transports that move energy below the surface to see how this affects the mean state of the model described in Chapter 2. The SST distribution plays a significant role in organizing and strengthening convection, even in the absence of ocean dynamics. To explore the potential role of ocean heat transport without significantly increasing the complexity of these experiments, the ocean heat transport is represented using a simple, external heating applied to the slab ocean. Still using RCE, we include a specified ocean heat transport analogous to what is seen in the tropical Pacific. These results are then compared with the control experiments that do not include a specified ocean heat transport. These experiments explore the effects of ocean heat transport on the global mean SST, as well as the climate sensitivity in response to forcing. This chapter will demonstrate that:

- For temperatures similar to the current tropics, ocean heat transport cools the climate primarily by increasing the efficiency of longwave cooling.

- For cooler temperatures, ocean heat transport can induce a cold, high-temperature-contrast climate driven by increased low cloud abundance.

- As the climate is warmed from this cold, high-SST-contrast state, a sudden transition to a much warmer, lower SST contrast state occurs, as the low clouds over the cold SST greatly decrease.

- For temperatures greater than about 310 K, the climate becomes more sensitive, even in the presence of ocean heat transport, at roughly the same temperature as the case without ocean heat transport.

1.0.3 Vertical Structure of Atmospheric Circulation

In our model experiments, we see shallow and deep circulation cells that flow from the warm SST to the cooler SST. The relative strength of the shallow circulation compared to the deep circulation increases with both mean SST and with SST contrast. In Chapter 4, we conduct fixed SST experiments where we measure the separate effects of mean SST and SST gradients on the relative strengths of the shallow and deep circulations. The circulation plays a critical role in setting the moisture distribution and consequently the efficiency of outgoing longwave radiation (Hartmann, Dygert, Blossey, Fu, & Sokol, 2022a). The vertical distribution of the circulation is significant for the organization of convection both in our and other experiments (Bretherton & Khairoutdinov, 2015). Similarly, Lutsko and Cronin (2024a) find a transition to a double cell structure in Mock-Walker cell experiments at sufficiently high sea surface temperatures. Outside of idealized models, tropical shallow circulations have also been shown in both observations and reanalysis data (Zhang, McGauley, & Bond, 2004; Zhang, Nolan, Thorncroft, & Nguyen, 2008a; Schulz & Stevens, n.d.). So, the Chapter 4 investigates the separate effects of SST and SST gradient on the shallow atmospheric circulation. These experiments use prescribed sea surface temperature distributions instead of the slab ocean used in the previous two chapters. This is done to enable differentiation between the effects of mean SST and SST range on the shallow circulation strength. This chapter finds:

- Both warming the average sea surface temperature and increasing the sea surface temperature gradient increase the strength of the shallow circulation.

- Warming the sea surface temperature strengthens shallow circulations primarily by enhancing shallow convection relative to deep convection.

- Increasing the sea surface temperature gradient strengthens shallow circulations primarily by enhancing shallow longwave cooling in the subsiding zone.

These three chapters attempt to address the underlying mechanisms governing the interactions between sea surface temperature, convection, and atmospheric circulation in an idealized framework. Chapter 2 sets the groundwork for the following chapters, exploring sea surface temperature's role in the organization of convection and the variability generated by these interactions. Because the sea surface temperature distribution is a product of both the atmosphere and ocean dynamics, Chapter 3 expands on the first by addressing the role of ocean heat transport in this framework. This chapter uses a simplified representation of this ocean heat transport as a specified surface heating to avoid overly increasing the complexity of the original experiments. Finally, Chapter 4 uses prescribed sea surface temperature distributions to study the impact of mean SST and SST range on the shallow circulation strength. Specifically, this chapter addresses the indirect role of sea surface temperature through its effects on boundary layer longwave cooling and shallow convection.

Chapter 2

CYCLE OF LARGE-SCALE AGGREGATION

The following chapter was published as:

Dygert, B. D., Hartmann, D. L. (2023). The Cycle of Large-Scale Aggregation in Tropical Radiative-Convective Equilibrium. Journal of Geophysical Research: Atmospheres.

2.1 Introduction

The interactions among convection, circulation and sea surface temperature (SST) in the tropics impact tropical storms, interannual variations in regional climate, the global energy budget of Earth, and the structure of climate change. The pattern and magnitude of tropical SST variations has been shown to affect the emergence of the global warming signal through its effect on clouds (C. Zhou, Zelinka, & Klein, 2016). Specifically, low clouds over the cooler tropics will be more reflective if the tropical SST contrast increases, producing a negative pattern effect feedback (Andrews et al., 2018a). In addition, the rate of warming over the warm pool in the western Pacific is important for global cloud feedback and regional climate responses, because the warm region has an effect on the global atmosphere (Dong et al., 2019). Therefore, understanding convection and SST interactions in the tropics and their role in controlling the SST contrast in the tropics are critical to estimating future warming and its impacts.

To study the thermodynamic interactions in a simplified setting, we employ a global aquaplanet climate model in which insolation is uniform, rotation is set to zero and the atmosphere interacts with a slab ocean model. Despite the lack of ocean dynamics in such a model configuration, the domain divides between warm convective regions and cooler subsiding regions in which the SST contrast is comparable to those observed within the Tropics (≈5K). If the heat capacity of the ocean is sufficient, these regions are robust and evolve slowly (Reed, Medeiros, Bacmeister, & Lauritzen, 2015; Popke, Stevens, & Voigt, 2013). This aggregation has important effects on climate sensitivity by modifying the emission temperature (Pierrehumbert, 1995) and influencing the cloud properties (Bony et al., 2016). Mechanism denial experiments have shown that longwave feedbacks between clouds and water vapor are necessary to trigger self-aggregation (Wing et al., 2017; Bretherton, Blossey, & Khairoutdinov, 2005; Tompkins & Craig, 1998), although details can differ across models and with global mean SST.

Hartmann and Dygert (2022b) investigate the time-mean climate and its sensitivity in the simulations discussed here. In this paper, we seek to better understand the oscillations of this global climate about its mean state, which are characterized by variations in the global SST contrast, circulation and climate feedbacks. In this way we get a better view of the positive feedbacks that lead to growing SST contrast and the counteracting processes that damp SST contrast when it becomes large.

Coppin and Bony (2017) found that for mixed layer depths greater than about 10m their model exhibited cyclic variability with periods on the order of a year or more. They found a similar growth in the subsiding region and increase of the warm pool temperature that we find here, followed by a collapse of the warm SST values before beginning another cycle. They also noted that the global mean temperature decreases when the SST contrast is large. Drotos, Becker, Mauritsen, and Stevens (2020) investigate the cyclic behavior in the ECHAM6.3 model and find that the SST gradient builds a strong capping inversion in the subsiding region which leads to an increase in low cloud fraction and a large global cooling event as part of the cycle. Coppin and Bony (2018), however, find that SST gradients actually limit the increase in low cloud cooling caused by self aggregation alone.

Although these studies use general circulation models (GCMs), similar RCE experiments with ocean mixed layers have also been conducted in cloud resolving models. Tompkins and Semie (2021) found that interactive SST delayed the onset of convective aggregation while Huang and Wu (2022) represent convective aggregation with interactive SST as a competition between the moisture convection feedback and the convection SST feedback. These feedbacks will play an important role here as well, although we focus less on the onset of convective aggregation and instead focus on the oscillation between aggregated and dis-aggregated states over a much longer timescale.

In this paper we use the oscillation within the model to focus on the mechanisms that maintain the warmest SSTs and their potential impact on the SST pattern. We particularly focus on the role of the atmospheric energy transport between the rising and subsiding regions in constraining the SST contrast, and how this changes with warming. We find that the instability that leads to increasing SST contrast ends when atmospheric energy transport away from the warm region induces strong cooling of the warm SST by enhanced evaporation combined with shading of the surface by deep convective clouds. Simultaneously, a decrease in cloud fraction and evaporation occurs over the cooler regions. As the SST contrast increases and the subsiding region expands, the peak surface winds and evaporation move toward warmer SSTs. This reduces the low clouds over the coolest SST regions where subsidence of warm, dry air increases entrainment drying. Positive skewness of the SST distribution marks the period when transport efficiently cools the warm SST, low clouds decrease in the subsiding region and the SST distribution returns to a more equable state.

The model and methods are described in Section 2.2 and an overview of the cycle is given in Section 2.3. The compositing procedure and results are described in Section 2.4 and Section 2.5 describes the changes in the oscillation as the SST is increased.

2.2 Model Experiments and Methods

The model used here is Geophysical Fluid Dynamics Laboratory's (GFDL) Atmosphere Model (AM2.1) with a slab ocean (SOM) (Anderson et al., 2004; Delworth et al., 2006). The rotation rate is set to zero and the insolation is globally uniform. CO_2 is set to 324 ppm and CH4 to 1650 ppb. Ozone is fixed to its tropical mean value. A horizontal spatial resolution of 2° latitude by 2.5° longitude, 32 vertical levels, and a time step of 900 seconds were used for the control experiments. A 50-meter deep slab ocean is used. The diurnal cycle is included. These are the same simulations as described in Hartmann and Dygert (2022b).

Seven experiments with incoming solar radiation corresponding to latitudes of 26, 28, 30, 33, 36, 38, and 45 at equinox will be discussed here. This yields four hot climates, two climates corresponding to the present-day tropics and a climate with the surface temperature of the present-day global average (289K), Table 2.1. Each experiment was run long enough to produce 40 years of stable climate for analysis after an initial spin up period. These experiments are denoted by their approximate global average sea surface temperature. For example, the control experiment with an insolation of 342 Wm^{-2} is called “C302.”

In addition to these control experiments, we performed two experiments in which surface enthalpy fluxes or atmospheric radiative heating rates throughout the column are homogenized horizontally. As seen in similar fixed SST experiments, making either the radiative cooling or surface fluxes uniform suppresses convective aggregation–greatly decreasing the SST contrast and its associated cyclic variability (Bretherton et al., 2005).

We will use an index of SST difference between warmest and coolest 20% of area ($Tdif$) to characterize the cycle and we will also divide the domain into subsiding and rising regions by using the mass average of the pressure velocity to define the subsiding regions and subsiding fraction (SF). We also use area averages over the regions of upward and downward motion.

To understand the energy transfer between the ascending and descending regions throughout the cycle, we will define the gross moist stability (GMS) to be the mass integrated flux divergence of moist static energy (MSE). Our use of GMS is for convenience and to loosely tie our analysis to more rigorous and theoretical uses of the terminology (Neelin & Held, 1987; Raymond, Sessions, Sobel, & Fuchs, 2009).

$$GMS = \frac{1}{g}\int_0^{P_s} \nabla \cdot (MSE\,\mathbf{V})\,dP \tag{2.1}$$

Here $\mathbf{V}$ is the horizontal velocity vector and P is the pressure. The units of GMS are Wm^{-2}. We can compute the GMS point by point, and we can average over the area of rising motion. By using the GMS averaged over the region of upward motion ($GMSup$), we can measure how the circulation is influencing the energy balance in the upward region.

2.3 Overview of the Cycle

We center our analysis on the effects of the SST contrast and use the difference between the top and bottom 20 percent of SST, weighted by area, as our metric for describing the

Table 2.1: Mean values for control experiments.

Case	SST	Tdif	Precip	SF	RH	OLR	Albedo
C289	288.7	6.10	2.83	0.58	48.9	234.7	0.24
C302	302.1	6.96	4.18	0.63	47.0	266.7	0.22
C304	303.5	8.03	4.46	0.65	46.0	271.5	0.22
C307	306.8	9.74	5.13	0.67	44.6	284.7	0.22
C309	309.2	11.14	5.60	0.67	43.6	295.1	0.22
C313	312.9	8.93	6.06	0.68	43.1	306.0	0.21
C318	318.4	6.29	6.39	0.75	42.8	317.3	0.19

cycle and call it $Tdif$. By using the SST contrast as the compositing variable, we can look in more detail at how each component of the atmosphere varies with respect to the range of SST. This choice is to some extent arbitrary, since most quantities vary with the same period and all are coupled, but on fast time scales the atmosphere responds to the SST, so that we regard SST contrast as more of a control variable than subsiding fraction, which, from a causality perspective, we will consider a response to the SST distribution. We will also consider composites of subsiding fraction and skewness of the SST distribution.

To illustrate the degree of periodicity in the simulations, we show the power spectra of four variables in Figure 2.1. The temporal variance is proportional to the area under the curves. Most other variables, including the global mean precipitation and high cloud fraction, show similar changes in temporal behavior across the seven control cases. These spectra were computed with a Hamming window with a length of 64 months and 50% overlap from 480 months of model data, so each spectral estimate has a minimum of 15 degrees of freedom. Linear trends were removed from each segment prior to computing the spectra.

The spectra in Figure 2.1 show that the variance of SST contrast is very small for the cold case C289 and for the second hottest case C313. For the hottest case, C318, the variance increases again, but is more characteristic of white noise than a preferred period.

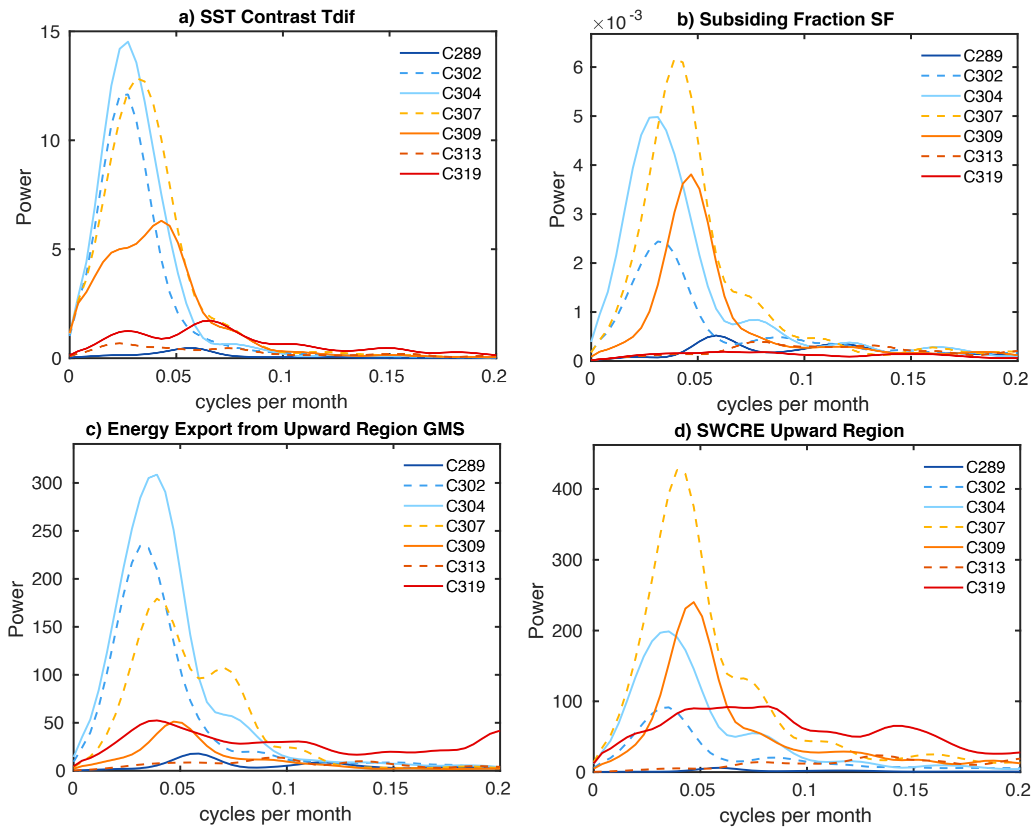

Figure 2.1: Power spectra for the seven control cases of a) $Tdif$, b) Subsiding fraction (SF), c) Atmospheric energy export from the region of rising motion ($GMSup$) and d) Shortwave cloud radiative effect (SWCRE) in the region of upward motion.

A preferred period of about 30 months occurs for the intermediate cases, with the strongest variance for the cases that are similar to, or slightly warmer than, the present-day tropics. The frequency of the oscillation increases somewhat as the climate is warmed, and evidence of a higher harmonic appears as a side lobe to the main peak, notably for the energy export from the region of rising motion in the C307 case.

If starting from a uniform SST, random instability will result in convection that leads to a warming and moistening of the same region in which this convection is occurring. In regions without convection, radiative cooling will support subsidence, drying of the free troposphere and radiative cooling to balance convective heating elsewhere in the domain.

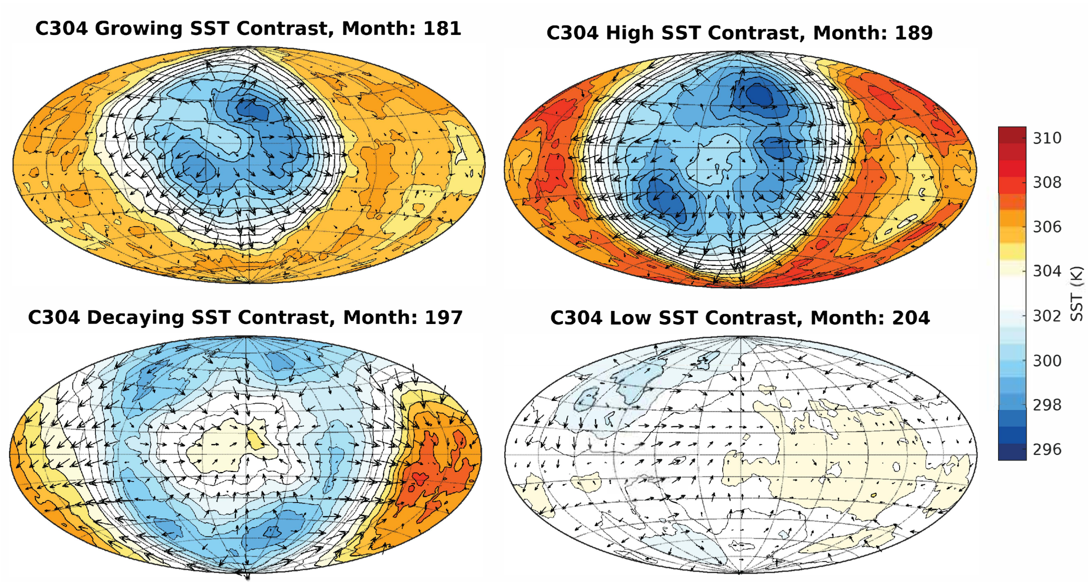

Figure 2.2: Monthly-mean snapshots from one cycle of case C304 of SST and reference-level winds at different stages in the SST contrast cycle: Growing, Maximum, Decaying and Low SST contrast. Hammer equal-area projection is used.

The feedback between moisture, radiation and circulation causes the domain to divide into regions with convection and regions of cooler SSTs with subsidence (Emanuel, Wing, & Vincent, 2014). The SST increases under the moist region and cools under the dry region. The SST distribution then cycles between times of low SST contrast and high SST contrast.

To illustrate the spatial structure of the oscillation, we show maps of the SST and low-level winds for case C304 in Figure 2.2. The scale of the SST contrast tends to assume the largest possible scale with one warm area and one cooler area. The cycle is illustrated with maps from the growing phase, the maximum contrast phase, the decaying phase and the subsequent low-contrast phase when the SST is most equably distributed. Each phase is separated by about 8 months. During the growth phase the SST distribution is negatively skewed and strong winds over the colder SST lead to an expansion of the cold region while the warm region maintains pockets of very high SST. In this particular case, as the cold region expands, winds weaken in the center of the cold region and the SST there begins to increase. Higher surface winds invade the warmer SST regions during the decay phase and the distribution of SST becomes positively skewed, with a relatively small region of very warm SST and a larger region of cooler SST. This evolves to the state of low SST contrast, at which time another cycle of SST contrast growth begins.

2.4 Compositing the Cycle

To understand how key variables change with SST, compositing of the cycle is performed relative to the parameter $Tdif$, the difference between the warmest and coldest 20% of SST by area. The time series of monthly $Tdif$ values is first smoothed with a broad band-pass filter centered on the frequency in which the cycle has the maximum amplitude. A 6th order Butterworth band-pass filter with cuts at 0.04 and 0.02 of the Nyquist frequency were used on monthly data. The maxima of this timeseries then define the key dates for the the compositing analysis, and a lagged compositing analysis is performed of the unfiltered variables of interest, so the filtering is only used to choose the key dates.

Diagnosis of the energy balances will be key to understanding the mechanisms of the cycle. Neglecting storage of energy in the atmosphere, energy balance requires that,

$$GMS \approx SWnet_{TOA} - OLR - SHB \tag{2.2}$$

where GMS is the net energy export by atmospheric transport , $SWnet_{TOA}$ is the net incoming solar radiation at the top-of-the-atmosphere (TOA), OLR is the outgoing longwave radiation, and SHB is the surface heat balance,

$$SHB = SWnet_{sfc} + LWnet_{sfc} - (LE + SH) \tag{2.3}$$

where SHB is also the energy storage in the ocean, $SWnet_{sfc}$ is the net solar absorption, $LWnet_{sfc}$ is the net longwave into the surface and LE and SH are the fluxes of latent and sensible heat away from the surface by turbulent motions.

Rearranging (2.2) we can also write,

$$SHB \approx Rnet_{TOA} - GMS \tag{2.4}$$

where $Rnet_{TOA}$ is the net radiation balance at TOA. Equation 2.4 indicates the key role of atmospheric energy transport in controlling the surface heat balance. The trigger mechanism for strong atmospheric heat transport from the warm to the cool region will be shown to be a key determinant of the cycle. The atmospheric transport does not peak at the time of maximum SST contrast, but rather at a time determined by the positive skewness of the SST distribution and large subsiding fraction. That the maximum atmospheric transport occurs after the time of maximum SST contrast and persists as the SST contrast decreases is critical to the oscillation.

Note here that our definition of the energy budget is an approximation based on the assumption that the atmospheric energy storage is small. On the time scale we are using here, atmospheric storage of energy is very small compared to the overall atmospheric energy transport. In addition, using GMS calculated directly by the definition given in Equation 3.1, rather than as a residual, does not alter our results.

2.4.1 Composites in SST versus Time Space

We will first show the cycle in an SST histogram framework. Global data are binned by 0.25K SST increments for each monthly mean. These data are then composited relative to the time of maximum SST contrast. A probability distribution of SST can be formed at each lag by dividing the area-weighted number of hits in each SST bin by the total number of area-weighted hits.

Figure 2.3 shows composites of area percent and surface energy balance component anomalies as functions of SST and lag from the month of maximum SST contrast for case C304, Figure 2.3a can be found for all cases in the supplemental material. Minus lags are before and positive lags are after the maximum in $Tdif$. A contour of 10 for the pdf of area fraction means that 10% of the area is the same temperature to within 0.25K. The energy flux anomalies are from the unweighted average of all the values in the composite, which is given as text near the bottom of each panel. The actual values at each SST-lag point in the plot can thus be found by adding the mean to the contour value. This was done so that the magnitude of the anomalies in panels b to d can be plotted with the same contour interval to show the relative importance of the variations in different energy flux components, despite their very different mean values. Also shown as lines on these plots

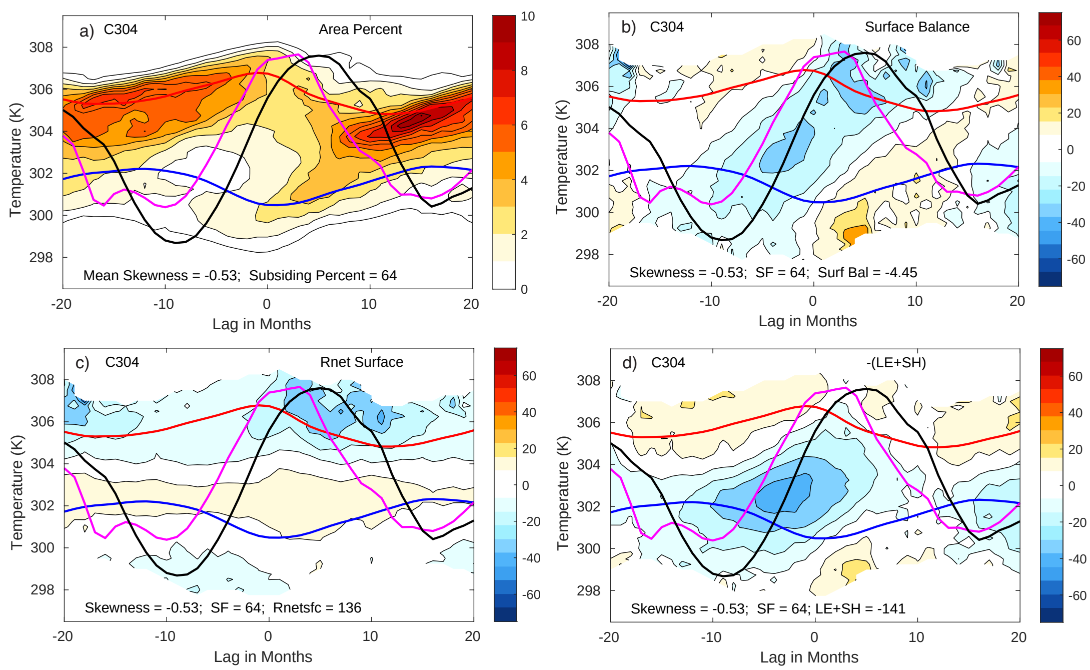

Figure 2.3: Composites of a) SST pdf in percent, b) Surface heat balance anomalies, c) Net Surface Radiation anomalies and d) surface turbulent cooling anomalies as functions of lag relative to the time of maximum SST contrast. Surface flux anomalies are in Wm^{-2}. The red line represents the average of the top 20% of SSTs, while the blue line represents the bottom 20% of SSTs. The black line is the anomaly of the skewness of the SST pdf times ten. The magenta line is the anomaly in the percent of the area that is subsiding. The values of subsiding fraction and skewness anomalies have an appropriate temperature added to them for plotting in the SST lag space.

are the temperatures of the warmest and coolest 20% of area. Anomalies of the percent subsiding area and the skewness of the SST pdf (times ten) are also shown, plotted with an addition to make them appear within the diagram. The range of variation for each can be obtained from the temperature difference between the maximum and minimum of the curve, then dividing the skewness difference by 10. So the range of skewness over the cycle in Figure 2.3 is about 0.9 and the range of subsiding fraction is about 7%.

Figure 2.3a shows that ten months before the maximum $Tdif$, most of the domain is covered by warm SSTs of a nearly uniform value. This warm region warms further, but decreases in area coverage as a region of cool SST develops that is about 6K colder than the warm pool. This trend continues until at maximum $Tdif$ the pdf is bimodal, positively skewed, and the subsiding area fraction is approaching its largest value. After maximum $Tdif$ is reached, shortwave cloud shading and enhanced evaporation strongly cool the surface of the warm region, and decreased evaporative cooling warms the cold region. By ten months after maximum $Tdif$, a new warm pool has formed at a cooler temperature and the process repeats.

Figures 2.3b-d show the anomalies in the surface energy budget terms. A region of negative net heat balance propagates from the cold to the warm SSTs as Tdif approaches and then passes its maximum value (lag 0). Surface turbulent and cloud radiative effects collaborate at the extremes of SST distribution with radiation dominating the variation at high temperatures and surface turbulent flux variations dominating at low temperatures. The effect of low clouds in the cool region is weaker than in some other simulations, notably Drotos et al. (2020).

Figure 2.4 shows TOA energy budget quantities and -GMS, the convergence of atmospheric energy transport in Wm^{-2}. The net radiation and net cloud radiative effect (NCRE) vary little over the warmest water during the cycle, in general agreement with a weak net cloud radiative effect in observations (Harrison et al., 1990). A mechanism to keep TOA NCRE small in a climate model with a mixed layer has been tested by (Wall, Hartmann, & Norris, 2019). Atmospheric transport and shortwave cloud radiative effect cool the warm region strongly during the period when the temperature of the warmest water is declining (Figures 2.4b,d). SWCRE is mostly offset by LWCRE at TOA, but the enhanced export

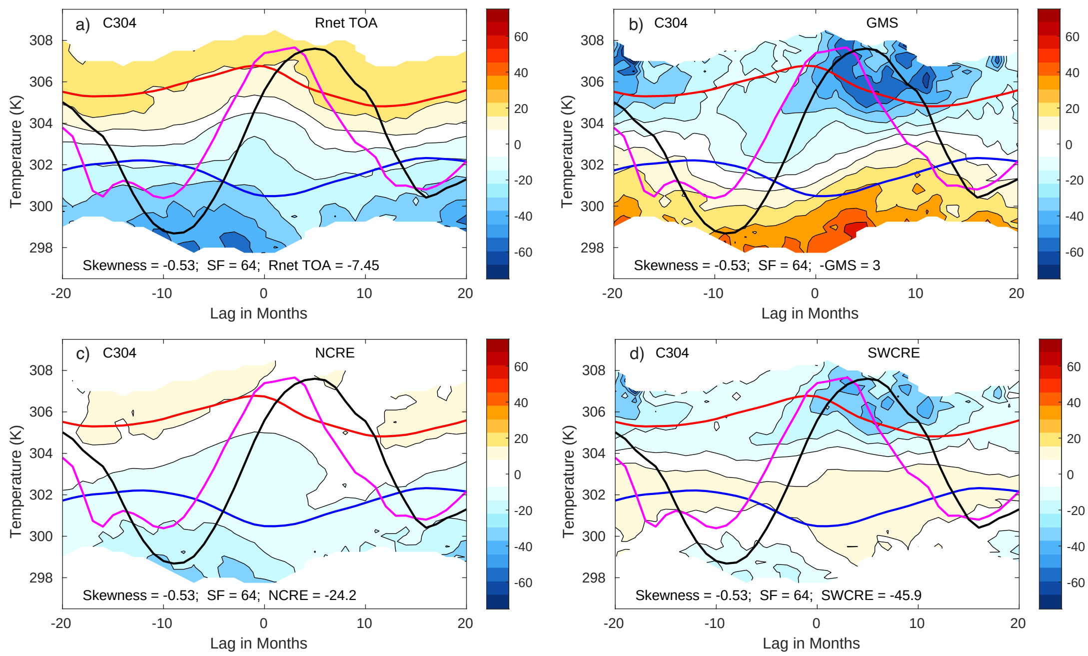

Figure 2.4: As in Figure 2.3 except, a) Net TOA Radiation anomaly, b) -GMS net atmospheric energy export anomaly plotted with negative sign, c) Net cloud radiative effect anomaly and d) Shortwave cloud radiative effect anomaly.

of energy by atmospheric transport facilitates the cooling of the surface, as atmospheric energy export is balanced by enhanced evaporative cooling of the surface (Eqn 2.4). NCRE anomalies become significantly negative over the coolest regions, but these cool regions occupy a very small fraction of the total area. The proximate cause of the strongest cooling of warm SST is marked by a strong increase in atmospheric export, which peaks after the maximum SST is achieved and continues until the SST distribution is at its most equable. This atmospheric energy export is correlated with with positive skewness of the SST distribution.

To summarize the section,

1. The SST gradient grows in the beginning of the cycle as low clouds and surface evaporation cool the subsiding region and the greenhouse effect warms the ascending region.

2. As the SST contrast grows, the subsiding fraction and area of coldest SSTs grows.

The shrinking warm pool and expanding cold pool are represented by the increasing skewness of the SST distribution.

3. The increasing skewness of the SST distribution then leads to a strong increase in atmospheric energy transport away from the warm pool.

2.4.2 Streamfunction Composites

In the previous section it was shown that atmospheric transport of energy plays an important role, especially during the time when the warmest SST values are cooling rapidly. In this section we will investigate the circulation between the warm and cool areas using a streamfunction. Hartmann and Dygert (2022b) binned the model data by SST and plotted the data by the fraction of the area occupied by SST from coldest to hottest. Since the coordinate is then proportional to area, we can compute and plot a streamfunction as a function of pressure in this coordinate system. This reveals that the overturning circulation has two circulation cells, a lower one that is tied to surface processes and the decline of humidity above the boundary layer, and a deep circulation that is driven by the heating and cooling in the upper troposphere and tends to remain at a fixed temperature as the climate is changed. In Figures 2.5a,e,f,m,q we show these streamfunction plots for the prior weak, growth, maximum, decay and posterior weak gradient phases of the SST contrast for case C304.

During the time when the SST contrast is increasing fastest (Figure 2.5e-h), the lower and upper circulation cells are centered in the relatively cool SST region with a narrow region of subsiding motion over the cool SST and a broad region of weak upward motion over the warmer SST. The shallow circulation is stronger than the deep circulation cell. The net heating rate (Figure 2.5f) that balances the shallow circulation is driven by radiative cooling over the coolest SSTs with a relatively shallow convective heating over the intermediate SST values. Low fractions of high cloud extend across the warmest 60% of SST area (Figure 2.5g) and the region of low mid-tropospheric relative humidity is confined to a small region of low SST values. A sharp decline in relative humidity occurs near the top of the boundary layer (Figure 2.5h). A maximum in the relative humidity occurs in the lower troposphere

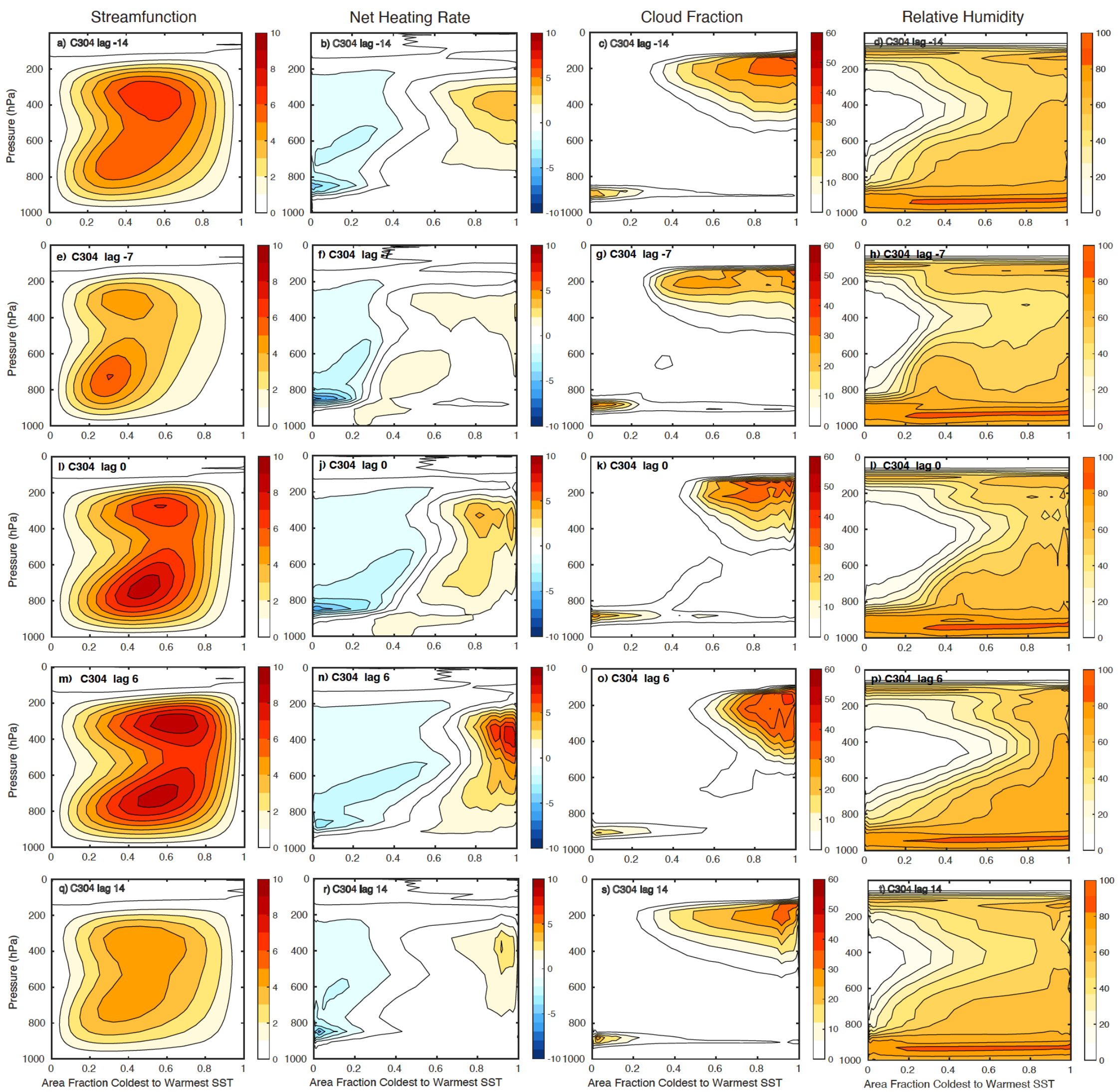

Figure 2.5: Streamfunction ($10^{11} kgs^{-1}$), Diabatic Heating Rate ($Kday^{-1}$), Cloud Fraction (%) and Relative Humidity (%) as functions of pressure and SST Area Fraction for the preceding small gradient phase (lag=-14, a-d),growth phase (Lag=-7 months, e-g), maximum SST contrast (lag=0, i-l.), decay phase (lag=+6 months, m-p) and proceeding small gradient phase (lag=+14, q-r).

at intermediate values of SST, and is associated with the upward branch of the shallow circulation. The growth phase is thus composed of a small area of intense downward motion and a larger area of weak upward motion and relatively thin, but widespread high cloud. The downward motion is especially strong in the lower troposphere, where it is driven by radiative cooling at the top of the boundary layer and in the air above, which becomes drier with altitude. This shallow circulation driven by radiative cooling at the top of the boundary layer is consistent with the radiatively-driven large-scale instability that separates the flow into rising and subsiding regions described by Emanuel et al. (2014), except that it is limited to a shallow circulation.

As the cycle progresses toward maximum SST contrast at lag=0 (Figures 2.5i-l), the lower and upper circulation cells both strengthen and move toward warmer SST as the downward region expands in area and the upward motion over the warmest SST increases in strength. The center of the lower overturning cell moves from 0.3 to 0.5 SST area fraction, compared to the growth phase. The diabatic heating and the relative humidity distributions also shift consistently with the overturning circulation. The radiative cooling associated with the wedge of low humidity that extends into a larger area toward warmer SST helps to balance the subsiding motion in the more intense lower cell.

These trends continue into the phase of most rapid SST decline (Figures 2.5m-p). In this phase the diabatic heating and high cloud amount are concentrated over the warmest SST and the vertical velocity reaches a maximum over the highest SST. This phase is associated with a maximum in the export of energy from the warm region Figure 2.4b, which results in the rapid cooling of the warm SST waters by evaporative cooling and shortwave shading.

The cooling phase has sufficient momentum to return the SST distribution to a nearly uniform warm pool about 14 months after the maximum SST difference was attained (Figure 2.3a). The SST distribution is more uniform after the maximum in Tdif than before it. With a relatively weak SST difference, the circulation is weak, but the small region of subsiding motion exists and is ready to develop into another cycle of increasing SST contrast (Figure 2.5q). This low-contrast phase has a large area with high clouds and a relatively small area where low humidity extends down to the boundary layer (Figures 2.5s,t).

The circulation throughout the cycle, as described above, develops as follows:

- Towards the beginning of the cycle, just as the SST gradient and the moisture gradient across SSTs begin to increase, a strong shallow circulation develops over the coldest SSTs. This shallow circulation is associated with drying of the troposphere in the region of subsiding motion and is in turn enhanced by the radiative cooling from the bounday layer.

- As the subsiding region expands, the warm pool shrinks, and convection intensifies, both the shallow and upper circulation cells shift to warmer SSTs.

- As the circulation peaks over the warmest SSTs, the resulting increase in export of energy from this region helps bring the SST distribution back to its original, relatively uniform distribution.

2.4.3 Compositing of upward and downward regions

In this section we consider composites of averages of the energy budget quantities over the rising and subsiding regions. Figure 2.6 shows top-of-atmosphere and surface energy budget composites for averages of the upward and downward regions for case C304. These are plotted as anomalies from their time mean values. We include the -GMS term with the TOA radiative fluxes to indicate the important role of atmospheric transport in the cycle. The atmospheric transport term (-GMS) has the largest variation of all the terms in in the upward region for the top of the atmosphere energy balance (Figure 2.6a). At the surface in the upward region (Figure 2.6c) the turbulent heating term -(LE+SH) has almost exactly the shape of the atmospheric energy export, which is required by the atmospheric energy balance.

The atmospheric transport and net shortwave radiation (SWnet) both act to increase $Tdif$ when it is increasing and reduce it when it is decreasing. The longwave term (-OLR) has smaller variations during the cycle and acts to decrease the amplitude of the cycle of $Tdif$. Interestingly, SWnet in the upward region peaks early in the cycle of growth when $Tdif$ is at a minimum ($\sim$ -10 months), declines as $Tdif$ grows and then becomes negative before $Tdif$ reaches its maximum value at lag 0. This suggests that the SWCRE is playing an important role in controlling the cycle, since it is the first term to reverse direction in the upward region as the cycle progresses.

At the surface in the downward region, the turbulent cooling and cloud shading contribute to the cooling leading up to maximum $Tdif$, while the LWnet plays a weaker role. The heating anomalies do not become substantially positive until more than 10 months after the maximum $Tdif$, when the surface anomalies in the upward region have also returned to positive anomalies (Compare Figures 2.6c and d).

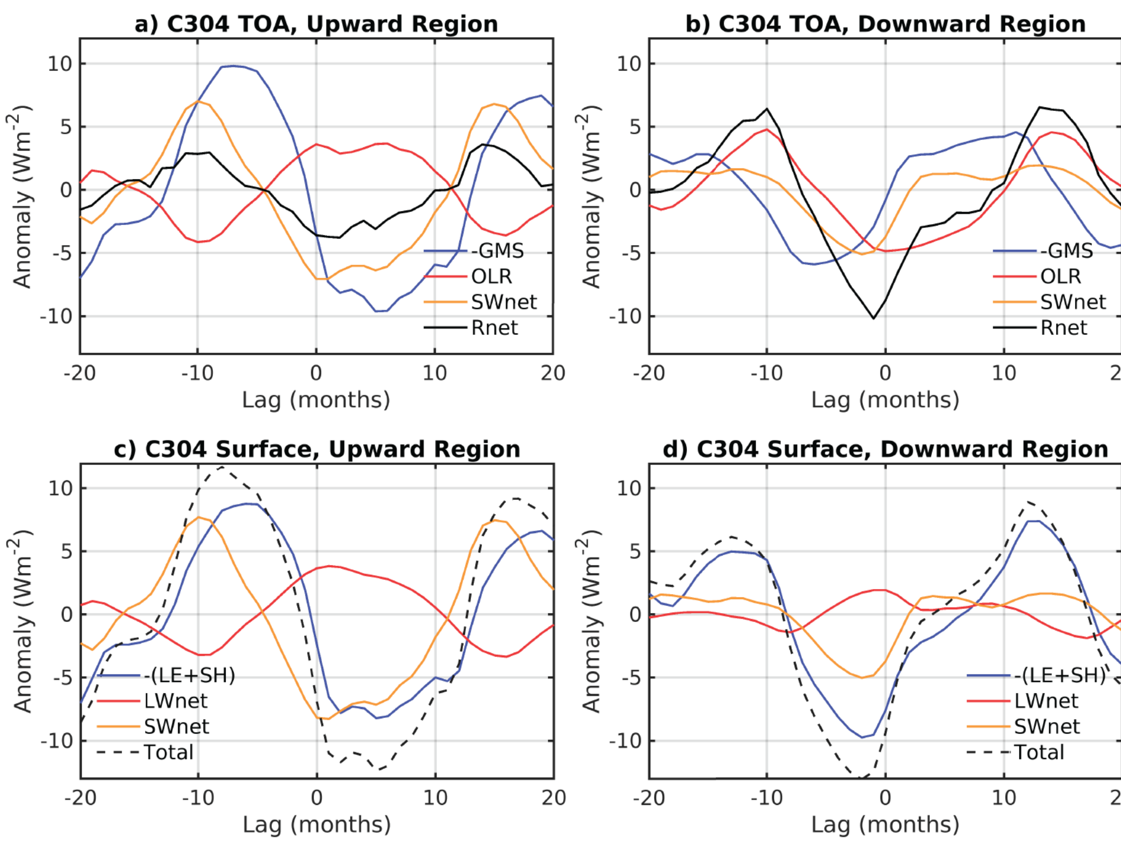

Figure 2.6: Anomalies in each term of the TOA (a,b) and surface energy (c,d) budgets for the upward and downward regions for case C304.

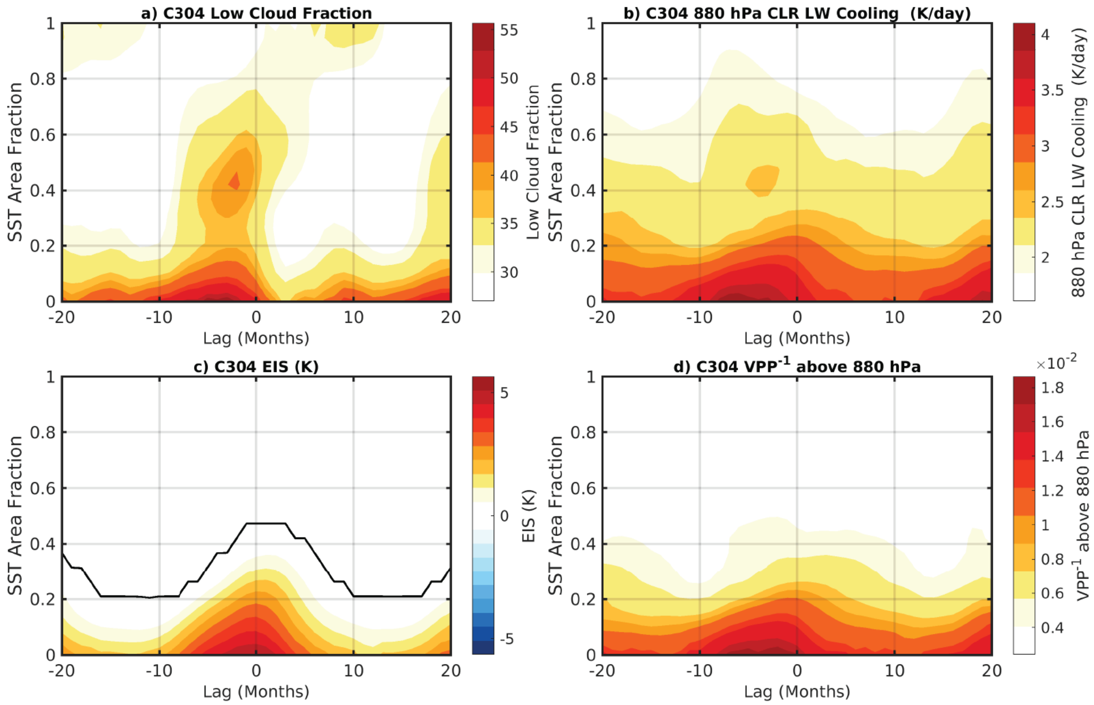

Figure 2.7: Lagged composites of variables in SST area fraction coordinates for case C304, showing a) cloud fraction, b) clear sky longwave cooling at 880 hPa (K/day) c) estimated inversion strength, EIS (K), and d) the inverse of vapor pressure path, VPP.

2.4.4 Low Clouds through the Cycle

The low clouds in the subsiding region also show significant changes throughout the cycle. As shown in Figure 2.7a, over the coldest SSTs, the low cloud fraction increases as the SST contrast grows before dropping sharply just as the SST contrast peaks. The second, smaller low cloud maximum over intermediate SSTs is associated with convection and low level convergence as the subsiding region expands, and so is explained by a different mechanism from the main low cloud peak over the coldest SSTs. From previous studies, we would expect this low cloud decline to correspond to a decline in inversion strength. However, in this model, low clouds begin to decrease while inversion strength is still increasing, as shown by 2.7c. So, another explanation is required here.

Instead of EIS, we find that clear sky long wave cooling best explains the onset of the low cloud decline. We focus on clear sky longwave cooling at 880 hPa where the cloud fraction is maximized, shown in Figure 2.7b. To understand this decrease in longwave cooling, we turn to the cooling-to-space approximation. The derivation of the form used here can be found in Hartmann, Dygert, Blossey, Fu, and Sokol (2022b).

$$\frac{dT}{dt}\Big|_{\lambda} \approx -\left\{\frac{e^{-1}\,\pi\,g}{c_p}\;RH\;\;e_s(T)\;\;B_\lambda(T)\right\}VPP^{-1}. \tag{2.5}$$

where

$$VPP = \int_0^p RHe_s(T)dp \tag{2.6}$$

From these equations, we know that the clear sky longwave cooling rate is proportional to the vapor pressure at the level of emission and inversely proportional to the vapor pressure path (VPP) above that level. The inverse of VPP above 880 hPa is shown in Figure 2.7d. Especially over the coldest water, it decreases in phase with the clear sky longwave cooling rate at 880 hPa shown in panel b. We find that the change in VPP above 880 hPa appears to be the main contributor to the change in the clear sky longwave cooling rate.

The VPP is determined by both relative humidity and temperature, the lagged composites of which are shown in pressure coordinates for the downward region in Figure 2.8, panels b and c. In Figure 2.8a, cloud fraction is shown in pressure coordinates for comparison with the relative humidity and temperature changes. Due to the large scale circulation, the air temperature in the subsiding region is set by the surface temperature in the ascending region. As the hottest SSTs warm, so does the tropospheric air temperature in the subsiding region. So, with temperature increasing, we would expect an increase in VPP as the SST contrast grows, and a decrease as it decays, if the relative humidity is fixed. This is the opposite of what we see, however. The relative humidity decrease from subsidence drying wins out over the temperature increase, and the VPP decreases as the contrast grows, reaching a minimum just before the peak SST contrast.

While the VPP is set by the relative humidity changes, the increase in relative humidity above the boundary layer clouds just before the SST contrast peaks is set by changes in the circulation. Section 4.2 describes the changing circulation throughout the cycle, and Figure 2.5 shows the peak of the shallow circulation moving to warmer SSTs as the cycle progresses. The overall effect of this migration is illustrated by Figure 2.8 which shows the

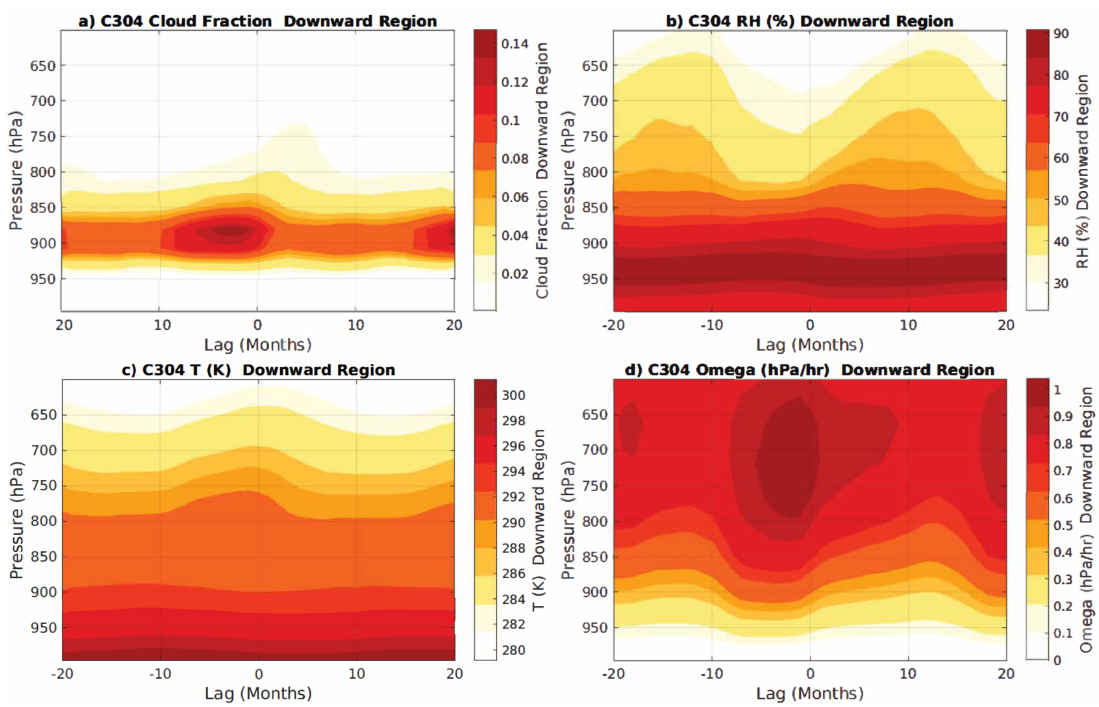

Figure 2.8: Lagged composites of variables in pressure coordinates averaged over the region of downward motion for case C302, showing a) cloud fraction, b) relative humidity (%) c) temperature (K), and d) vertical motion (hPa/hr).

time evolution of vertical profiles key to understanding changes in cloud fraction and relative humidity. As the subsiding fraction expands and the shallow circulation moves towards warmer SSTs, the subsidence over the boundary layer begins to decrease, as shown by Figure 2.8d. Working alone, we would expect this decrease in subsidence above boundary layer clouds to increase the low cloud fraction (Bretherton & Blossey, 2014). Decreased subsidence increases low cloud amount by allowing for deeper inversions, weaker entrainment, and an increased vertical extent of boundary layer clouds. However, in this model, the strong, large-scale organization of convection results in most of the water vapor in the free troposphere concentrated over areas of convection, leading to low relative humidity (around 40%) above the boundary layer in the subsiding region. So, when subsidence drying above the boundary layer weakens, this results in an increase in relative humidity, but an insufficient increase to promote cloud growth. Instead, the increased humidity above the boundary layer sharply decreases longwave cooling, cutting off radiatively driven turbulence necessary to sustain the boundary layer clouds.

The secondary peak of low clouds near SST area fraction of 0.4 in Figure 2.7a similarly depends on the shallow circulation cell moving into warmer SSTs. As the SST contrast peaks, the subsiding region expands, and the vertical velocity over intermediate SSTs flips from upward to downward motion (Figure 2.5e-m). This transition to downward motion leads to the rapid decrease in the low cloud fraction. Over these intermediate SSTs, the maximum cloud fraction in pressure coordinates occurs in the middle troposphere (Figure 2.5f-g), suggesting that this secondary maximum of low clouds is associated with the congestus mode of convection (Nuijens & Emanuel, 2018).

To summarize this section, cloud fraction over the coldest SSTs sharply decreases, starting just before the SST contrast peaks. This coincides with a decline in clear sky longwave cooling at the level where low clouds are maximum, 880 hPa. This decline in longwave cooling is primarily explained by an increase in VPP above 880 hPa, which itself comes from a decrease in subsidence. Over intermediate SSTs, low clouds associated with the congestus mode of convection similarly decline as the subsiding region expands.

2.5 Modification of the Cycle with Mean SST

We have described the mechanisms of the cycle for case C304 due to its resemblance to the current tropics as well as the robust cycle it exhibits. As shown by the power spectra in Figure 2.1, the cycle is strong for cases C302, C304 and C307. For case C309 the cycle speeds up, and for the warmest cases C313 and C318 the cycle is either weak or chaotic. Here we wish to better understand why these changes in variability of the model climate occur as it is warmed above the temperature of the current tropics. Our hypothesis will be that the strengths of the energetic and hydrologic feedbacks increase so that small variations in SST are met with a strong reaction that limits the cycle amplitude. This is consistent with the reduction in the mean SST difference with warming for the mean climate shown in Hartmann and Dygert (2022b). In addition, subsiding fraction and SST skewness both increase with SST, and these changes both enhance the effectiveness with which atmospheric transport can cool the warm region and decrease the effectiveness of strong subsidence in drying the cold region.

2.5.1 Feedback Strength and Warming

We can estimate the strength of the response of components of the energy budget to the SST contrast by using the peak-to-peak cycle amplitudes from the composites such as those shown in Figures 2.3, 2.4 and 2.6 from which the SST and energy budget components in the upward and downward regions can be computed. To estimate the peak-to-peak amplitude we first smooth the composites with a 1-2-1 filter to reduce the effects of noise. Figure 2.9a shows bar chart plots of the peak-to-peak amplitude of the SST in the upward and downward regions and of the difference between the upward and downward regions. The amplitude of the cycle in the difference between the upward and downward regions at first increases and then decreases for the three warmest cases. As the SST is warmed the amplitude of the difference is increasingly dominated by the changes in the region of upward motion. The reduction in the cycle at high temperatures may be related to the decline in the mean SST difference. In Hartmann and Dygert (2022b) it was shown that the decline in the mean SST difference between upward and downward regions at warm temperatures is related to a decline in the contrast in the greenhouse effect between moist and dry regions.

Figures 2.9b and c show the amplitude of the cycles in the surface energy budget for the upward and downward regions, respectively. These also increase and then decrease as the SST is warmed. Figures 2.9d and e show the feedback estimated by dividing the amplitude of the surface energy budget cycles by the amplitude of the cycle in the SST difference between the upward and downward regions. The goal here is to estimate how sensitive the flux cycles are to the SST difference cycle. We see that for the warmest cases the feedback gets larger, especially in the upward region. This suggests that as the SST warms the energy balance terms become much more sensitive to the SST and that this is what suppresses the magnitude and organization of the cycle. The relative importance of radiation feedbacks compared to latent cooling feedbacks increases from the cooler to the warmer climates in the upward region, but not in the downward region.

From this section, we see that the strength of the oscillation is closely tied to the strength of the hydrologic cycle. Although the SST contrast, in its mean state, peaks in case C309, we see that the cycle magnitude has already begun to decline. This decline and eventual disappearance of the cycle is shown to correspond to the strengthening of negative feedbacks with increasing global mean SST.

2.6 Summary and Conclusion

Global climate models in tropical aquaplanet mode with no rotation, uniform insolation and a slab ocean typically exhibit sustained oscillations about their climatological mean state. These oscillations can be characterized by the variations in the difference between the warmest and coolest quantiles of SST, by the difference in SST below the regions of upward and downward mean atmospheric motion or by the fraction of the global area that is rising or subsiding. For mean SST values close to the current tropics, the climatological SST distribution is negatively skewed with a large area of nearly uniform warm SST and smaller regions with much cooler SST, as in the observed tropics (Hartmann & Dygert, 2022b).

Starting from a state of near uniform SST, the SST contrast grows because the energy balance is positive over the warmer regions and negative over the cooler SST regions, most

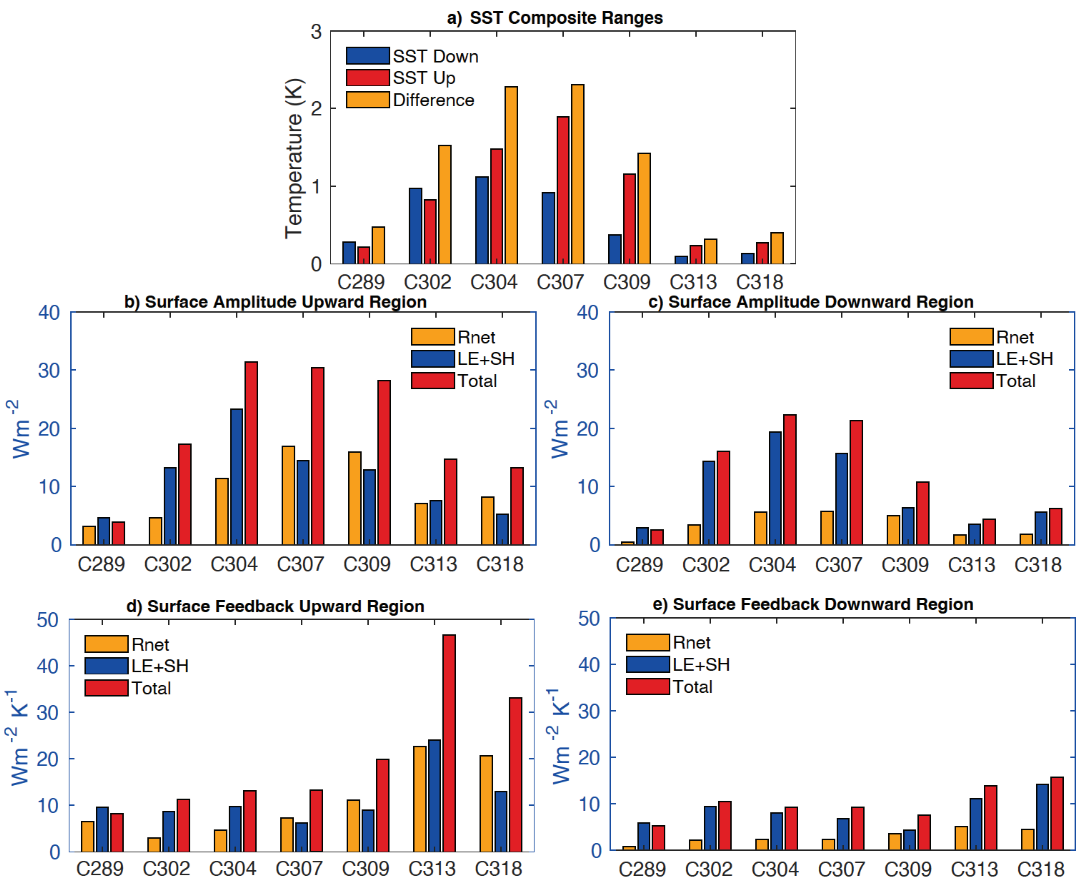

Figure 2.9: a) Peak-to-peak amplitude of the SST cycles in the upward and downward regions and of the difference between the upward and downward regions. Peak-to-peak amplitude of surface energy component composites in the b) upward and c) downward regions, and the feedback obtained by dividing the peak-to-peak amplitude of the energy budget quantities by the amplitude of the difference between the upward and downward SST for the d) upward and e) downward regions.

fundamentally because of the enhanced water vapor greenhouse effect in the convective region over the warmest SSTs. Subsidence over the cool region causes drying of the free troposphere, and the radiative cooling near the top of the boundary layer drives a shallow circulation that enhances the evaporation near the boundary between the warm and cool SST. The warmer water thus continues to warm, and a circulation develops that cools the SST outside the convective region via enhanced surface winds and reduced relative humidity. As the SST contrast grows, the export of energy from the warm area by atmospheric transport becomes more efficient so that the warm area becomes smaller, while the area of cooler SST expands.

When the SST contrast reaches its peak value, the cool area has grown and the warm area has shrunk to the point that the distribution of SST is positively skewed. This condition leads to efficient atmospheric transport of energy out of the warm region. Export of energy by atmospheric transport is associated with strong cooling of the warm region SST by cloud shading and enhanced evaporative cooling. The continued cooling of the warm region has more to do with the distribution of SST rather than the SST contrast, and is most efficient when the warm SST occupies a smaller fraction of the domain. This cooling of the warm region continues as the SST contrast declines and returns the SST distribution to a more uniform state with the pdf of SST peaked at an intermediate value.

Changes in the warm region are complemented by changes in the subsiding region, where the low cloud amount declines rapidly after the maximum SST contrast is achieved, helping the cool region to warm. The warm and cool regions are connected by atmospheric transport, which moves energy from the warm to the cool region most effectively during the period of rapid decline in SST contrast. Atmospheric energy export from the warm region is necessary to support the evaporative cooling of the surface there when the SST contrast is in decline. The cycle then repeats after the SST distribution becomes more equable and the positive feedbacks that lead to increased SST contrast begin again.

The cycle of low clouds differs slightly from Drotos et al. (2020) in that the inversion strength peaks after the low clouds have already begun to decline. Instead, we link the sharp decline in low clouds to the water vapor path above the boundary layer, which is set by the circulation. We find that the decreased magnitude of subsidence as the subsiding region expands leads to an increase in water vapor above the boundary layer. Because the convective aggregation significantly dries the free troposphere in the subsiding region, this increase in relative humidity is not sufficient to increase cloud water at smaller pressure levels. Instead, the increase in water vapor above the boundary layer decreases clear-sky longwave cooling across the cloud top. The decrease in radiatively driven turbulence results in a sharp decline in cloud fraction.

Evaporation and SW shading remain the dominant mechanisms for driving the cycle as the climate is warmed, but their relative contributions and oscillation amplitudes change with warming and also between regions of upward and downward motion within the same experiment. In the subsiding region, evaporation consistently plays a larger role than SW shading by as much as a factor of two for the colder cases. In the ascending region, however, evaporation and SW shading contribute approximately equally. SW shading becomes relatively more important in the rising region in warmer climates.

The coherence and amplitude of the oscillation vary with mean SST. For climates colder than the current tropics the oscillation is very weak and constrained to the regions of warmest SST. For climates substantially warmer than the current tropics the oscillation first speeds up and weakens and eventually disappears for very warm climates. The reasons for this have to do with the distribution of SST and the strength of the hydrologic and energetic feedbacks. For warmer cases the mean skewness of the SST distribution becomes positive, a situation in which the large-scale circulation acts to quickly suppress growth of the warm SST regions. Also, the negative feedbacks become much stronger in a warmer climate. We measure the strength of the feedbacks by comparing the amplitude of the surface energy budget variations with the amplitude of the SST contrast between the upward and downward regions. For warmer cases, a small increase in the SST contrast results in a much larger change in the energetic responses, which suppress SST contrast and its variations. These feedbacks are especially strong in the region of upward motion and warm SST, so that small increases in warm pool SST are met with large increases in shortwave cloud shading and evaporative cooling.

To summarize the main conclusions,

1. Atmospheric transport of energy between the rising and subsiding regions is critical for the development of warm SSTs. As the SST contrast builds and the circulation increases, the cooling of the warm pool is marked by a large export of energy into the subsiding region.

2. The sudden decay of low clouds over the coldest SSTs is driven by a sharp decline in clear sky longwave cooling due to increased vapor above the boundary layer clouds. This increased water vapor is associated with a decrease in subsidence drying as the subsiding region expands.

3. The oscillation speeds up as global mean SST increases, until the signal disappears for cases warmer than 309K. This increase in cycle speed is associated with increased efficiency of damping hydrologic feedbacks at warmer temperatures.

Some of the model behavior discussed here may be sensitive to the particular parameterizations employed in the model and so should be tested in different GCMs. The basic behavior of this model is very similar to the behavior discussed by Coppin and Bony (2017), however, and the key role of radiative contrasts between the upward-wet and downward-dry regions is robust and fundamental. The special role of the shallow circulation driven by radiative cooling in the subsiding region in driving the cycle of SST contrast appears to be a novel and likely robust result of this analysis.

The relative importance of feedbacks in the rising and subsiding regions are particularly sensitive to the parameterizations of ice clouds and low clouds, respectively. Simulations with models with sufficient resolution to not require a cumulus parameterization would be particularly interesting, but those simulations would also be sensitive to the ice cloud microphysics parameterization and the boundary layer cloud parameterizations. Moreover, the simulation of tropical anvil clouds is critical, since they contribute most of the radiative effect of tropical convective clouds, and even higher resolution may be necessary to simulate the dynamical, radiative and cloud-physical interactions within the anvils (Hartmann, Gasparini, Berry, & Blossey, 2018; Gasparini, Blossey, Hartmann, Lin, & Fan, 2019).

The SST contrast in the real tropics certainly depends on the effect of rotation and ocean heat transport. The way that these interact with the physical processes described here can be studied in future work.

Chapter 3

EFFECTS OF OCEAN HEAT TRANSPORT

The following chapter is currently in review as Effects of Ocean Heat Transport in Tropical Radiative Convective Equilibrium.

3.1 Introduction

The spatial pattern of Sea Surface Temperature (SST) in the tropics plays an important role in the mean climate and its sensitivity to change. For example, the circulation of the atmosphere responds strongly to changes in the tropical SST distribution (Bjerknes, 1966; Horel & Wallace, 1981). The separation of the circulation into regions of rising and sinking motion affects the outgoing longwave radiation (OLR). Regions of subsidence have lower water vapor content and form regions where the outgoing longwave radiation (OLR) is greater for a given SST than regions with higher humidity. This separation into regions of efficient longwave radiation to space and less efficient longwave radiation to space decreases the sensitivity of climate (Pierrehumbert, 1995).

The SST gradient also affects the abundance and optical properties of low clouds that form in regions of lowered SST and increased lower tropospheric stability (Klein & Hartmann, 1993). Increases in tropical SST gradient can increase the low cloud fraction in the cold SST region through both thermodynamic and dynamic effects, which may lead to a negative climate feedback (Miller, 1997; Larson, Hartmann, & Klein, 1999; Bretherton & Blossey, 2014).

Recent work has shown that an increase in the tropical SST contrast in the past 40 years has led to a negative "pattern effect" on climate sensitivity, primarily by increasing the reflectivity of low clouds over the cooler SST (Dong et al., 2020; Andrews et al., 2018b; Stevens, Sherwood, Bony, & Webb, 2016; Armour, 2017; C. Zhou et al., 2016). The La Niña-like SST changes in the tropical Pacific (warming in the West Pacific and cooling in the East Pacific) has global radiative effects that can lead to a lower apparent climate sensitivity (Dong et al., 2019; Armour et al., 2024a).

To better understand the mechanisms connecting the sea surface temperature pattern and radiation and how these might change with warming, it is helpful to study these interactions in a simplified framework. One method of studying the interactions between clouds, large-scale circulation and climate in a simplified framework is global radiative convective equilibrium (RCE) calculations in which the atmospheric structure is determined by a balance between radiative cooling and convective heating. Simulations over a fixed and uniform SST show that at high enough temperatures the circulation organizes into regions of moist air and convection and regions of dry air and subsidence, a process often called self-aggregation (Held, Hemler, & Ramaswamy, 1993; Tompkins, 2001; Bretherton et al., 2005; Held, Zhao, & Wyman, 2007; Coppin & Bony, 2015; Cronin & Wing, 2017; Retsch, Mauritsen, & Hohenegger, 2019). The initialization of self-aggregation in these uniform and fixed SST experiments is highly dependent on both the surface fluxes and the radiative cooling rates, and the dominant mechanism responsible can vary with the SST value (Bretherton et al., 2005; Coppin & Bony, 2015).

Aggregation of convection causes organization of the surface energy fluxes, with more column and surface energy loss over the dry, subsiding region than over the warm, rising region. One is then motivated to consider a model in which the SST can respond to these changed energy fluxes and allow the SST gradients to obtain their natural balance. A simple way to do this is to introduce a prediction equation for the SST, which assumes the surface is wet and has a heat capacity corresponding to a fixed depth of seawater, often called a slab ocean model. In this case a significant time-mean SST contrast develops, whose magnitude may also oscillate in time accompanied by an oscillation in the degree of aggregation (Coppin & Bony, 2018; Popke et al., 2013; Reed & Chavas, 2015; Dygert & Hartmann, 2023). Hartmann and Dygert (2022a) found that when forced by changing global mean insolation, such an RCE calculation with a slab ocean model in a global domain showed a change in apparent climate sensitivity from higher sensitivity for low global mean SST, low sensitivity for intermediate SST comparable to the current climate, and higher sensitivities for temperatures greater than about 310 K. The transition to larger sensitivity around 310 K has been reported in prior studies (Meraner, Mauritsen, & Voigt, 2013; Russell, Lacis, Rind, Colose, & Opstbaum, 2013).

In the present study we wish to know how the above considerations concerning radiative convective equilibrium above a slab ocean would be changed by ocean heat transport. For example, does the addition of ocean heat transport change the mean climate or its variations? Does the introduction of ocean heat transport change the sensitivity of climate? If either of these changes occur, by what mechanisms are these changes produced?

To make these considerations a little less abstract, let us consider the cases of El Niño Southern Oscillation (ENSO) variations in the tropical Pacific, where the mean state and its variations are affected by oceanic energy transport. Figure 3.1 shows the anomalous net energy flux from the atmosphere into the ocean and the total energy flux divergence in the atmosphere as functions of longitude and Niño 3.4 index. Data were obtained from ERA5 reanalysis (Hersbach et al., 2020a). The Niño 3.4 index was computed from the ERA5 SST averaged over the region 5°N–5°S, 190°E–240°E.

Figure 3.1a shows that during a strong El Niño event (Niño 3.4 $\approx +2$) there is an anomalous flux of nearly 40 Wm^{-2} from the ocean to the atmosphere in the Eastern Pacific equatorial ocean. These anomalies in surface heat flux are formed of about equal parts increased surface evaporation and decreased absorbed solar radiation anomalies (not shown). Figure 3.1b shows that a nearly equal flux of energy is carried away from the region by the atmosphere during strong El Niño events. This export of energy results in a convergence of atmospheric energy transport in other equatorial regions, though some is transported to the extratropics. Although the evolution of tropical SST during El Niño events is a transient process, and storage in the ocean is important (Cheng et al., 2019), the time scale is long enough that surface fluxes are in balance with atmospheric transport. In the calculations to be described below we will assume that the ocean heat transport is constant in time and compute the equilibrium response of SST and the associated atmospheric circulation to that constant ocean heat transport.

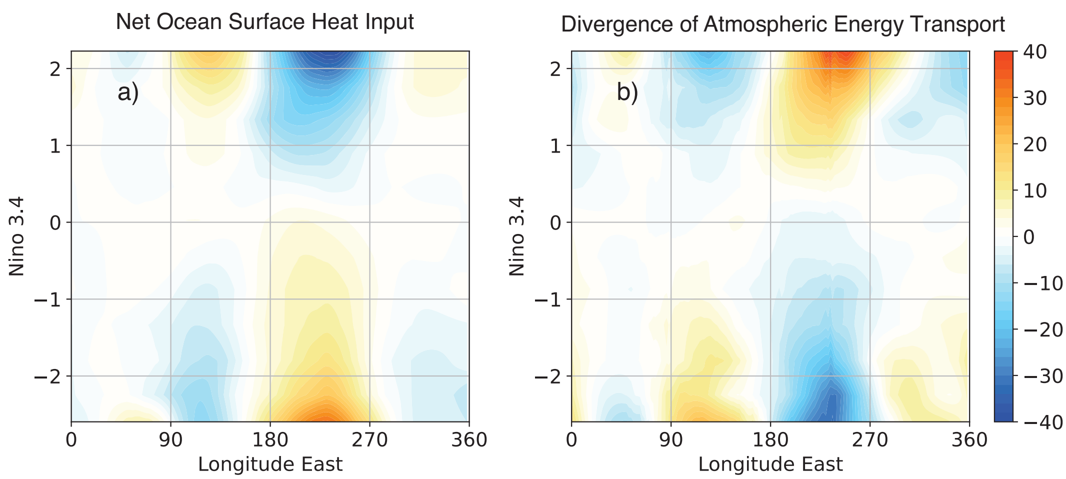

Figure 3.1: Contour plot of a) anomalous net flux of heat into the the ocean and b) divergence of total energy transport by the atmosphere averaged for the region from 10S to 10N as functions longitude and Niño 3.4 anomaly. Data are from ERA5. Units are Wm^{-2}.

To represent the effect of ocean heat transport in the context of our global RCE model with a slab ocean, we introduce constant, but spatially varying sources and sinks of energy in the slab ocean. We then compare these simulations with control simulations in which no ocean heat transport is included.

The model and experiment descriptions can be found in Section 3.2. We then describe the change in the SST distribution between the control and the ocean heat transport experiments in Section 3.3. Section 3.3.6 discusses the effect of ocean heat flux on the sensitivity to insolation changes. Finally, in section 3.4, we see that the changes in energy budget when adding ocean heat transport to our idealized experiments are similar to the changes we see in observations of the transition from El Niño to La Niña over the tropical Pacific Ocean, although our model experiments are only a very rough analogy to the tropical Pacific and ENSO.

3.2 Model and Experiments

Experiments are conducted using GFDL's AM2.1 with no rotation, uniform insolation, 50-meter slab ocean, no land, 2 by 2.5 degree horizontal resolution, and 32 vertical levels.

Stated differently, this is an aqua-planet simulation with no rotation and uniform insolation, simulating a tropical world. Control experiments are conducted with no ocean heat transport. By increasing the insolation, we create a series of control experiments at a range of global mean SSTs from about 288 K to 318 K. Simulations are run long enough to produce a sample of 40 years of equilibrated climate after a spin-up period of 20 or more years. The control experiments with no ocean heat transport are taken from Hartmann and Dygert (2022a) and more details about these experiments can be found there.

In this paper we use the same model configurations as Hartmann and Dygert (2022a), except that we apply sources and sinks of energy to the slab ocean layer. In climate modeling that employs slab ocean models, sources and sinks of energy added to mimic the effect of ocean heat transport are often called "Q-fluxes". So in comparing these cases to the control cases described above, we will use the letter C to denote the control cases without ocean heat transport and we will use the letter Q to denote the new simulations with specified ocean heat transport.

The shape and magnitude of the Q-fluxes were chosen to loosely replicate the natural structure of SST anomalies emerging from the control experiments, which tend to take on a global wavenumber one pattern with one maximum and one minimum (Hartmann & Dygert, 2022a). As shown in Figure 3.2a, we use a Gaussian shaped dipole of Q-flux with a maximum magnitude of 50 Wm^{-2}. The global-mean Q-flux is zero. A value of 50 Wm^{-2} was found to be large enough to lock the convection over the warmest SST. Because convection preferentially occurs over warmer SSTs, positive Q-flux serves as an attractor for the atmosphere to organize around–with convection and warmer SSTs above the positive Q-flux and colder SSTs and subsidence above the negative Q-flux. The magnitude of ocean heat transport chosen here is not too dissimilar from the observed anomalies associated with El Niño shown in Figure 3.1. Also, the climatological flux of energy into the ocean in the equatorial eastern Pacific is on the order of 100 Wm^{-2} (Hartmann, 2016), which is similar to the contrast in ocean heat transport that we apply here. This magnitude of Q-flux fixes the locations of warm and cold SSTs over the regions of positive and negative Q-flux, respectively. With significantly weaker Q-flux, the internal feedbacks between the atmosphere and the ocean are sufficiently strong to move the SST around in space as in

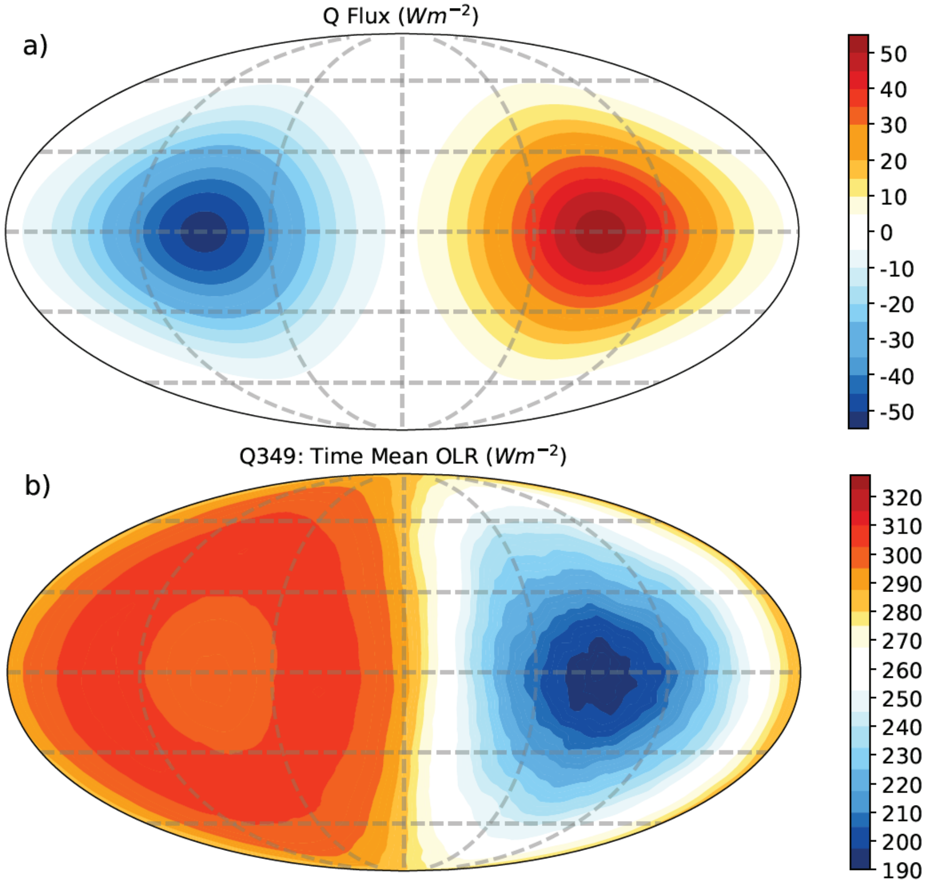

Figure 3.2: Global structure of a) time invariant Q Flux and b) outgoing longwave radiation (OLR) averaged over the final decade of simulation in Hammer equal-area projection.

experiments with zero Q-flux. This simplified Q-flux is included to test the reaction of the atmosphere to forcing from the ocean, resembling an idealized version of the gradient in ocean heat uptake from the East Pacific to the West Pacific and Indian Oceans.

As an example of how the atmosphere responds to the imposed Q-flux, Figure 3.2b shows the time mean outgoing longwave radiation (OLR). The Q-flux fixes the regions of subsiding and ascending motion over the regions of cooling and warming respectively, and the OLR reflects the location of convection. The OLR is enhanced over the dry, subsiding region over the region of negative Q-flux, and is suppressed over the region of positive Q-flux where the atmosphere is ascending, moist and cloudy.

3.3 Mean State Changes

In this section, we will discuss the changes to the SST distribution and energy budget between cases with and without the Q-flux. Figure 3.3a shows the SST averaged over the coldest 20% by area, warmest 20% by area and the global mean SST as functions of the insolation for both the control cases and the Q-flux cases. In all cases the coldest 20% of SST values decreases much more than the warmest 20% of SST values in response to Q-flux, and in every case the global mean temperature is cooled by the addition of Q-flux. The Q-flux has a dramatic effect on SST, except for the SST over the warmest 20% of SST for cases with global mean SST similar to the current tropical climate (≈300 - 309 K). In these cases the warmest SST values only decrease by a small amount in response to Q-flux.

The addition of Q-flux has a much larger effect at colder temperatures corresponding to low insolation values, and introduces an apparent abrupt regime transition from a colder to warmer climate when crossing insolation values of about 335 Wm^{-2} (Fig. 3.3a). The reasons for this transition will be discussed later, but it is similar to a much weaker transition in sensitivity and temperature that occurs between a cold regime and an intermediate regime in the control cases (Hartmann & Dygert, 2022a). Also apparent is a change to increased sensitivity to insolation increases that occurs around global mean temperature of 310 K. As mentioned previously, many climate models show an increase in climate sensitivity at temperatures around 310 K, which is associated with the increased efficiency of water vapor absorption, particularly in the continuum region (Meraner et al., 2013; Hartmann & Dygert, 2022a). This warm transition occurs both in the control and Q-flux cases. Between the cold and warm transitions is a region of relatively stable climate, as measured by the increase of temperature with increasing insolation. Hartmann and Dygert (2022a) showed that this stable region is associated with the strong stabilizing effect of the radiator fin mechanism of Pierrehumbert (1995) in this temperature range.

3.3.1 SST Distribution and Organization

In simulations with uniform SST the organization in RCE experiments can be characterized by the subsiding fraction (SF), the area of the domain with downward motion (Wing et al.,

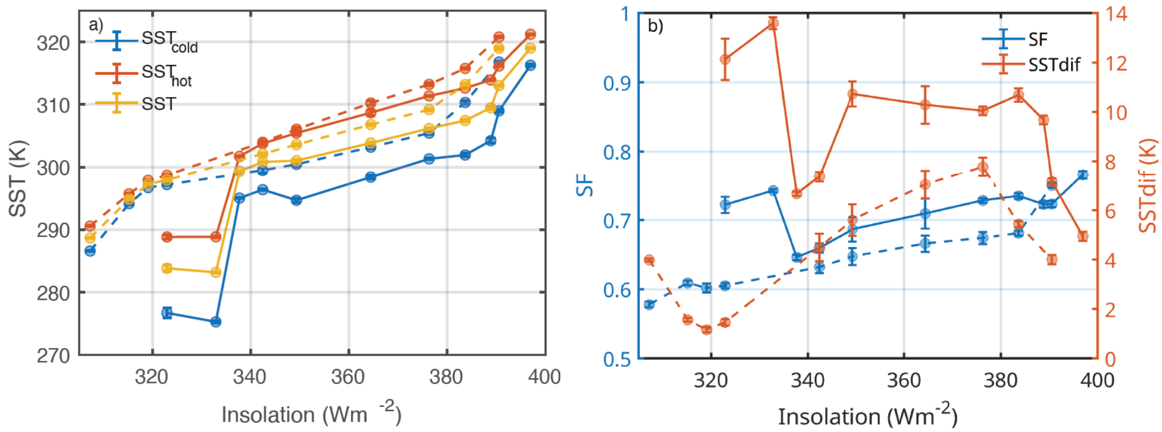

Figure 3.3: Line plots versus insolation of a) the coldest 20% SSTs (blue), warmest 20% SSTs (red) and global mean SST (yellow) for the Q-flux (solid) and control (dashed) cases, and b) the SST contrast between the top and bottom 20% SSTs (SSTdif) in orange and the subsiding fraction (SF) in blue for the control (dashed) and OHT (solid cases).

2017). Here we compute the subsiding fraction using the mass-averaged pressure velocity. With predicted SST, however, the SST contrast between the cold and warm regions can also be used as a metric for the strength of self-aggregation. We define this SST contrast, $SSTdif$, as the difference between the warmest and coldest 20% of SSTs. Because there is no rotation and insolation is uniform, in cases with no Q-flux the warm and cold pools do not have any spatial preference and tend to move around with time and oscillate in amplitude (Coppin & Bony, 2017; Dygert & Hartmann, 2023). In the cases with strong Q-flux discussed here, the upward motion tends to remain over the geographically fixed region of positive Q-flux, where the warmest SST values also remain. The water vapor follows the Q-flux and SST distribution. Because the Q-flux tends to fix regions of subsiding and ascending motion in place, the moisture gradient between the two regions is enhanced. The effect of this on the OLR distribution is shown in Figure 3.2b. The OLR is enhanced in the dry, subsiding region over the coldest SSTs and suppressed in the humid, convecting region over the warmest SSTs.

As shown in Figure 3.3b, in the control experiments (dashed lines) SST contrast at first declines with increasing SST, up to an SST value of about 300 K, after which it increases up until 310 K at which point it rapidly declines as the climate is warmed further. In the case with Q-flux the SST contrast is very large for the two lowest values of insolation and temperature, then abruptly drops as the insolation is increased further. By comparing Figures 3.3b and 3.3a one can see that the rapid transition in the Q-flux case occurs at about the same global mean temperature of 300 K as the change from decreasing to increasing SST contrast in the control case. For the Q-flux experiments there is also a rapid reduction in the subsiding fraction as the temperature warms across the rapid transition around 300 K. We force the SST to change with insolation variations, but we believe that the regime transitions would occur at similar temperatures if we forced climate change in a different way, such as increasing carbon dioxide. This is because the regime transitions are related to the amount of water vapor in the atmosphere, which is mostly a function of mean SST.

The subsiding fraction is shown in Figure 3.3b. It is greater than 60% in almost all cases and increases in response to Q-flux. Greater SST contrast generally tends to concentrate the convection in a smaller portion of the domain (Dygert & Hartmann, 2023). Subsiding fraction is greater than 70% for the two cold cases and drops significantly as the climate abruptly warms around insolation of 335 Wm^{-2}, where the mean SST increases from about 285 K to 300 K in the Q-flux experiments.

To summarize, Q-flux cools the mean climate compared to the control case. Most of this cooling occurs in the subsiding cold region. The climate has three regimes similar to the control case, with an intermediate insensitive climate and cooler and warmer edge climates that are more sensitive. These regimes are shifted to higher insolation values in the Q-flux experiments because of the mean cooling that Q-flux produces. In the Q-flux case the cold regime is very cold with high SST contrast and shifts abruptly to a warmer climate with much reduced SST contrast as the insolation is increased by a small amount. The mean SST increases from $\approx$285 K to $\approx$300 K across this cold transition. The transition to a more sensitive very warm climate occurs at about 310 K for both the Q-flux and control cases, as has been observed in other GCM studies.

3.3.2 Energy Budget Changes

As in the case of the observed El Niño cycle shown in Figure 3.1, the atmosphere energy transport will play an important role in the simulations described here. We define the divergence of vertically integrated total energy transport (DAT) as the mass-integrated flux divergence of moist static energy (MSE), where V is the horizontal wind field and P is pressure.

$$DAT = \frac{1}{g}\int_0^{P_s} \nabla \cdot (MSE\,\mathbf{V})\,dP \tag{3.1}$$

Assuming atmospheric energy storage is small, however, DAT can alternatively be calculated as a residual in the atmospheric energy budget equation, which becomes the difference in top of the atmosphere radiation and the flux of energy across the surface.

$$DAT = R_{net,TOA} - SEF \tag{3.2}$$

Here, we define the surface energy flux from the atmosphere to the ocean (SEF) as the total of all energy budget terms crossing the surface. The surface flux terms are the net LW at the surface (LW_{net}), the net SW at the surface (SW_{net}), and the surface fluxes associated with evaporation (LE) and sensible heat flux (SH).

$$SEF = LW_{net} + SW_{net} - (LE + SH) \tag{3.3}$$

Figure 3.4 shows key regional top-of-atmosphere energy budget terms for the regions with mass-averaged upward and downward motion, which correspond to warm and cold regions. Panels 3.4a and 3.4b show top-of-atmosphere energy budget terms for the subsiding and rising regions, respectively, for both the control (dashed) and Q-flux (solid) cases. Note that the divergence of atmospheric energy transport, DAT, is plotted with opposite sign, so that it is actually the convergence of atmospheric energy transport. This is done so that DAT and Q-flux do not obscure each other in the plot. Looking first at Figure 3.4a we see that in the downward region a close balance exists between net shortwave absorption and OLR, with the small difference balanced by atmospheric transport and Q-Flux. For the two cold Q-flux cases we see a large reduction in both OLR and net shortwave radiation. The OLR decreases because it is colder in the Q-flux case than in the control case, and it is colder because the absorbed solar radiation is less, which we will see is associated with increased low cloud reflectivity.

Turning to the region of rising motion in Figure 3.4b, we see that the OLR is again substantially reduced for the two coldest cases, again because it is colder, but the net solar radiation is not correspondingly decreased, since in the rising region high clouds are always present. The albedo of the high clouds in the upward region does not respond much to the addition of Q-flux. In the rising region the increase in the TOA radiation balance that would be implied by the reduction in OLR is balanced by an increase in the divergence of atmospheric energy transport, DAT.

Figures 3.4c and 3.4d show the changes in energy budget components between the Q-flux and control experiments for each insolation value. DAT and OLR are shown with negative signs to indicate their effect on the TOA energy budget. Let's begin by discussing the coldest cases, with insolation equal to 323 and 333 Wm^{-2}, respectively. In the descending region decreased absorbed solar energy is balanced primarily by decreased loss of OLR, while the cooling due to Q-flux and the heating due to increased atmospheric energy convergence are smaller contributors. For the other, warmer cases in the subsiding region the energy budget responses to Q-flux are much smaller and the Q-flux is balanced in a variety of ways. Figure 3.4d shows that in the rising region the addition of heat by the Q-flux is offset predominantly by increased divergence of atmospheric transport (DAT). The bar charts for the warmest cases with 391 Wm^{-2} of insolation do not balance well. This is likely because the control case has a small SST contrast that oscillates chaotically so that the energy balances are less meaningful.

Comparing the temperature changes in Figure 3.3a with the energy budget changes in Figure 3.4a, we see that for the warmer cases with mean SST greater than about 300 K, the change in cold region temperature in response to Q-flux is significant, while the OLR changes in the cold region are rather small. This is possible because at tropical temperatures most of the OLR comes from the atmosphere, rather than the surface. Because there is no rotation, the atmosphere temperature profile above the boundary layer in the subsiding region is similar to the atmosphere temperature profile in the rising region. Because the

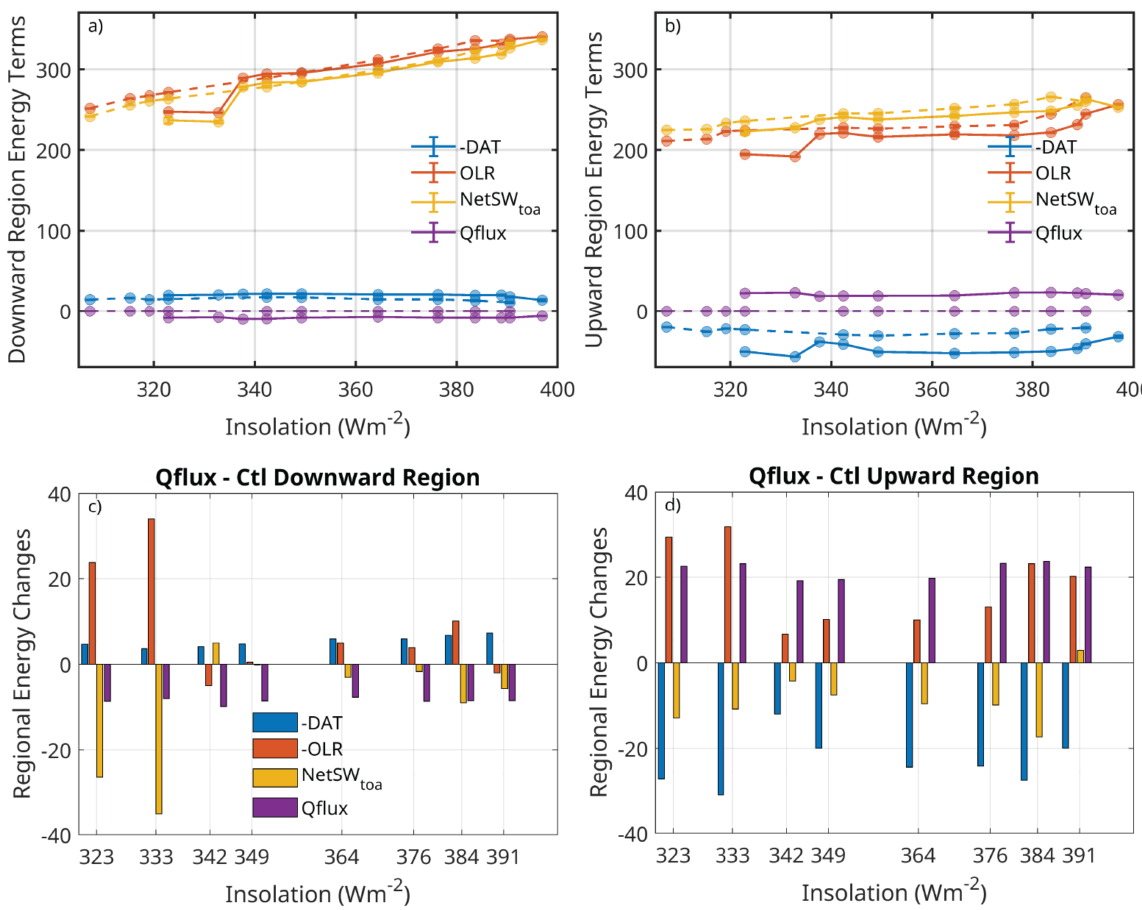

Figure 3.4: The top panels show regional energy terms, divergence of atmospheric energy flux (blue), outgoing longwave radiation (red), net shortwave at the top of the atmosphere (yellow), surface heat flux (purple) averaged over the region of ascending motion in panel a) and the region of descending motion in panel b). Dashed lines represent the control cases, solid the Q-flux cases. The bottom row shows bar charts of the same regional energy variables, but instead show the change when adding Q-flux in experiments sharing the same insolation.

warm region SST does not change much in response to Q-flux, the atmospheric temperature does not change much above the boundary layer, and the OLR therefore does not change much in response to Q-flux. In the downward region then, the surface temperature can decline without much reduction in OLR to suppress the cooling. In the region of rising motion, heat that is added by Q-flux is exported to the subsiding region, where it balances the OLR loss, which stays about the same despite the cooler surface with Q-flux. These mechanisms are similar to the ones that cause the intermediate climates to have a low sensitivity, as discussed in Hartmann and Dygert (2022a).

To summarize, for the coldest climates with resulting global mean temperatures around 285 K, Q-flux produces a transition to a cold, high-SST-contrast state. An abrupt transition occurs across which the global mean SST increases and the SST contrast decreases. In this warmer regime (300-309 K) Q-flux produces a global cooling, mostly associated with cooling in the subsiding region. This surface cooling in the subsiding region has only a small impact on the OLR in the subsiding region for the warmer cases, because the atmospheric temperature is controlled by the warmest SST values, which don't change much in response to Q-flux.

3.3.3 Dynamic and Thermodynamic responses to Q-flux

To better understand how Q-flux affects the SST it is helpful to visualize how the circulation and thermodynamic properties respond to the addition of Q-flux. We will compare cases C349 and Q349 that have insolation of 349 Wm^{-2}, but with the latter having an added oceanic heat transport represented by a Q-flux. To show the structure compactly we plot circulation, relative humidity and air temperature as functions of pressure and SST area fraction. We divide the SST into 0.25 K intervals and then compute the area-averaged atmospheric structure for those SST bins. Each monthly grid cell from 40 years of simulation is identified by its SST, and variables of interest are averaged for each SST bin. Each SST bin also has a value that determines what fraction of the total area of the globe falls within the SST bin, $f_A(SST)$. The cumulative area fraction is computed by integrating this pdf of area fraction across SST, thus defining the cumulative "SST area fraction", which varies

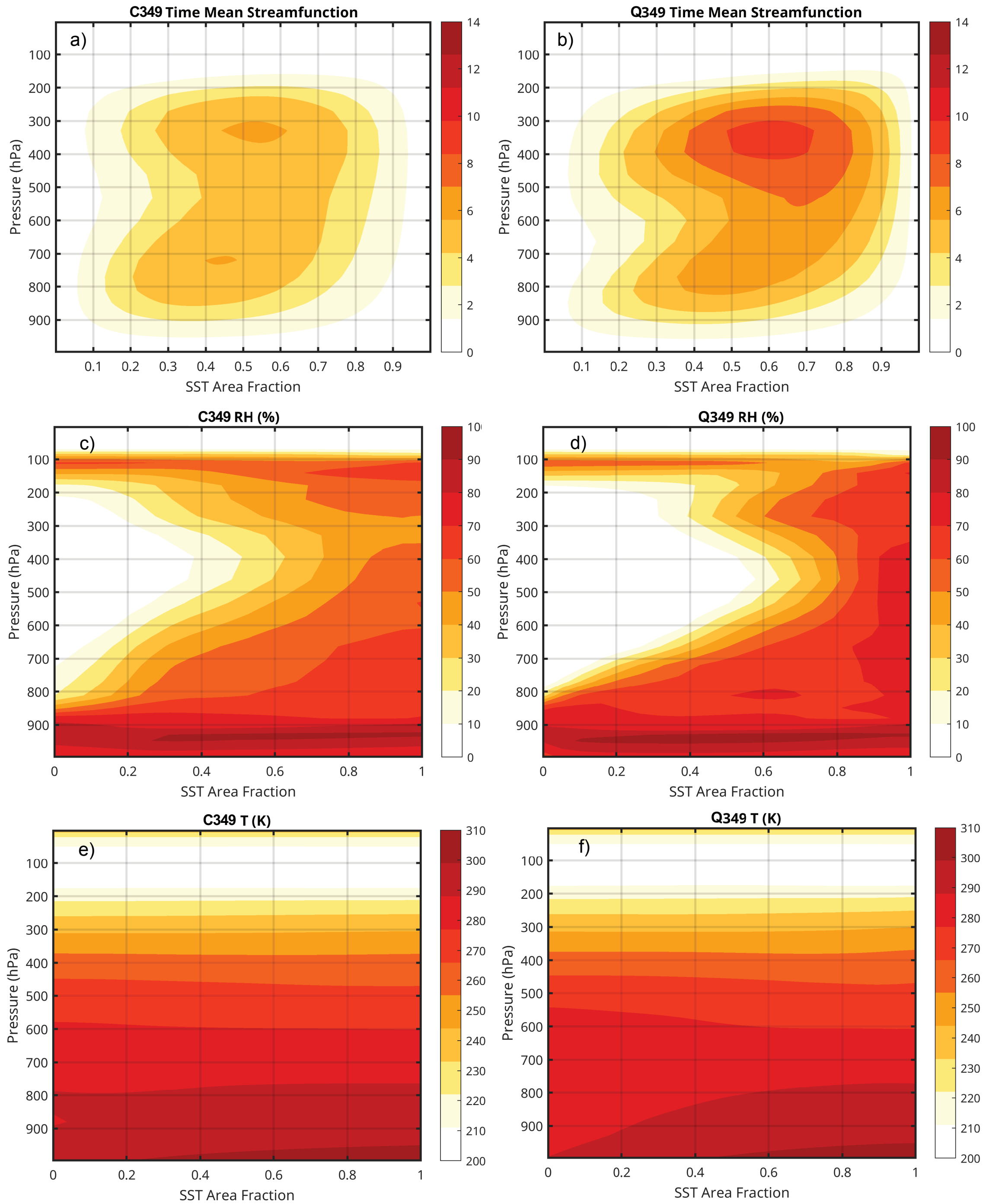

Figure 3.5: Comparisons of the vertical profiles in pressure coordinates, binned by SST area fraction between control case C349 and its Q-flux counterpart with the same insolation Q349. The top row shows the streamfunction ($1.0 \times 10^{11} kgs^{-1}$) strengthening, the second row shows the relative humidity (%) drying over the colder SSTs, and the third row shows the small temperature (K) changes in the mid troposphere where most of the OLR originates.

between zero and one.

$$\Phi_A(SST) = \int_0^{SST} f_A(SST)\, dSST \tag{3.4}$$

A streamfunction can be computed by integrating the omega vertical velocity in Pa/s through area,

$$\Psi(\Phi_A, p) = \frac{A_E}{g} \int_0^{\Phi_A} \omega(p)\, d\Phi'_A \tag{3.5}$$

Here A_E is the surface area of Earth, g is the acceleration of gravity and $\Psi(\Phi_A, p)$ has units of $kg\ s^{-1}$. The horizontal area velocity in $m^2 s^{-1}$ flowing toward the region of warm SST is then computed from,

$$V = -g\, \frac{d\Psi}{dp} \tag{3.6}$$

and the pressure velocity can be obtained from

$$\omega = \frac{g}{A_E} \frac{d\Psi}{d\Phi_A} \tag{3.7}$$

Figure 3.5 shows cross-sections in pressure versus SST area fraction coordinates for case C349 and its corresponding Q-flux case Q349 with the same insolation, 349 Wm^{-2}. Changes in the circulation with added Q-flux are illustrated through the streamfunction in panels a and b. With added Q-flux, the circulation strengthens and leads to more distinct shallow and deep cells. This helps to dry the troposphere over the coldest SSTs, as shown through relative humidity (RH) in Figures 3.5c,d. The Q-flux case has a sharper vertical gradient of RH and a much larger area of very dry air above the boundary layer, consistent with the increase in subsidence drying. Figures 3.5e,f show the cross-sections of temperature. Although the coldest SSTs cool in response to Q-flux, air temperatures above the boundary layer are set by the warm pool and cool much less than the surface. So, while the surface temperature decreases in the subsiding region, the levels above the boundary layer where most of the OLR originates remain at about the same temperature after Q-flux is added. In addition, decreased emission from the surface through the atmospheric window region can be offset by the drier atmosphere above causing the atmospheric emission to move to slightly lower and warmer regions of the atmosphere.

In summary, we see the increase in circulation drying out the troposphere while the tropospheric air temperatures change only slightly above the boundary layer. This explains why, for the intermediate climates (300-309 K) the OLR in the subsiding region does not decrease much as the surface temperature is reduced by the addition of Q-flux.

3.3.4 The Greenhouse Effect and OLR Efficiency

To quantify the effect of atmospheric temperature and humidity structure on OLR, it is helpful to consider the greenhouse effect, GHE.

$$GHE = \sigma T_s^4 - OLR = \sigma T_s^4 (1 - E) \tag{3.8}$$

where E is the OLR efficiency defined by

$$E = OLR/\sigma T_s^4 \tag{3.9}$$

We introduce E here so we can use the term "OLR efficiency" with a specific meaning. It is also a useful metric for the longwave effect of SST contrast on climate. We will see that Q-flux increases the OLR efficiency and that this is a primary mechanism whereby Q-flux cools the climate.

Figure 3.6 shows key variables for understanding the change in regional energy balance in response to Q-flux and insolation increases. Figure 3.6a shows the greenhouse effect as a function of insolation for the control and Q-flux cases. For the coldest cases Q-flux causes a large decreases in the GHE, because of the cooler surface and drier atmosphere. For the intermediate (300-309 K) cases the addition of Q-flux reduces the greenhouse effect in the subsiding region by about 20 Wm^{-2}. Except for the two coldest cases, Q-flux has very little effect on the greenhouse effect in the upward region. Figure 3.6b shows that most of this changed GHE is present in the clear-sky fluxes and so does not depend on cloud changes. At the warmest temperatures greater than 310 K, the GHE over the subsiding region begins to increase, which is related to the rapid increase in water vapor path (WVP) in the subsiding region that is shown in Figure 3.6d. Figure 3.6c shows a large change in albedo between the coldest cases and the warmer cases, but in the intermediate regime where the mean

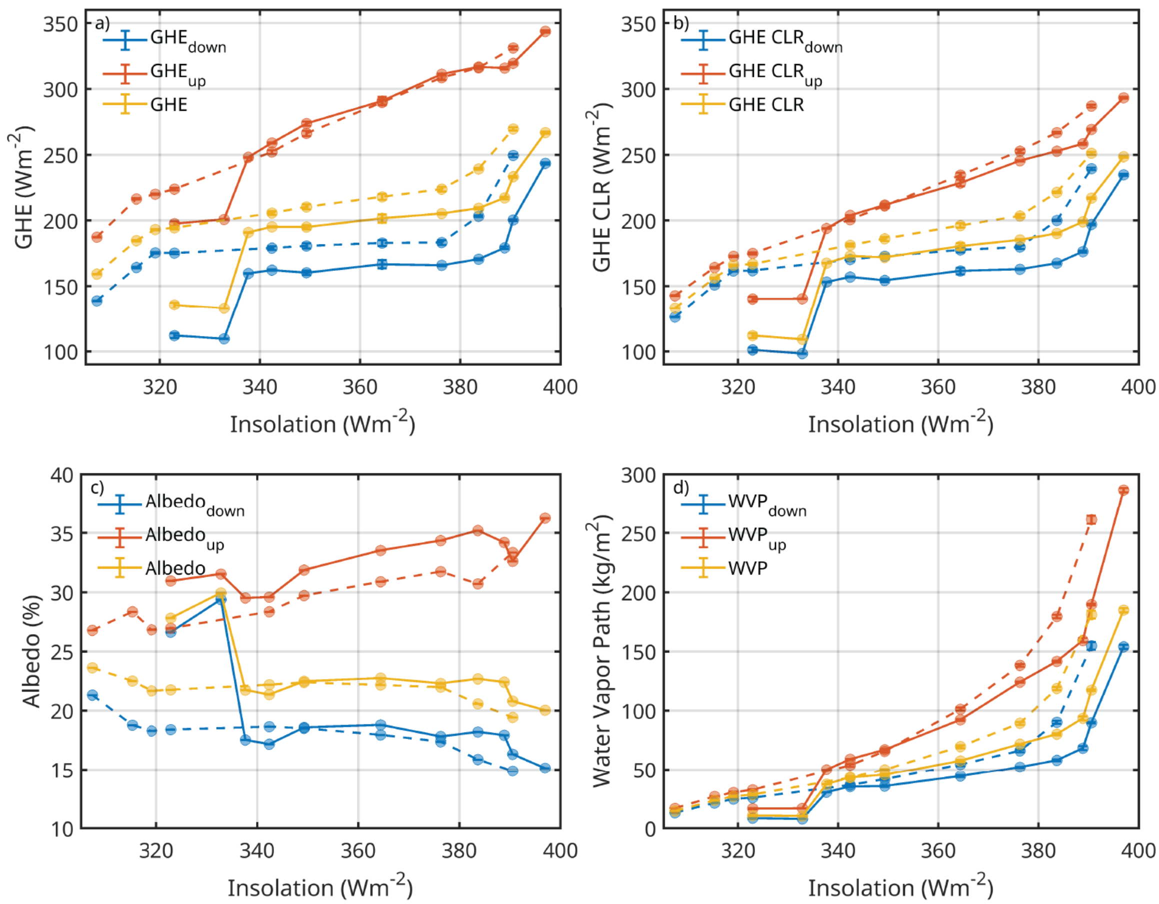

Figure 3.6: The top panels show the total a) and clear-sky b) greenhouse effect (GHE) in Wm^{-2} averaged over the region of ascending motion (orange), descending motion (blue) and globally (yellow). Panel c) shows the albedo (%), and panel d) shows the water vapor path (WVP) in kgm^{-2}. The dashed lines represent the control cases and the solid lines represent the Q-flux cases.

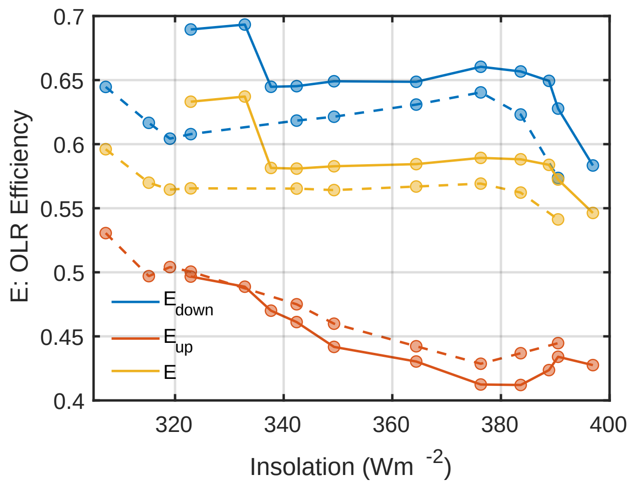

Figure 3.7: OLR efficiency E as in (3.9), plotted versus insolation for the upward, downward and global domains for both the control (dashed line) and the Q-flux (solid line) experiments.

SST is about 300-309 K the albedo in the downward region is insensitive to Q-flux and also does not change much as the mean SST warms from 300 K to 309 K. The albedo in the upward region does increase somewhat in response to Q-flux, possibly because the increased SST gradient associated with Q-flux confines the deep convection and upward motion to a smaller part of the domain.

Figure 3.7 shows the OLR efficiency as defined in (3.9) averaged over the upward, downward and global domains for both the control and Q-flux experiments. For the global mean and downward regions the OLR efficiency is greater in the Q-flux cases. This is because Q-flux lowers the SST in the subsiding region and also creates larger and drier subsiding zone. In the upward region, Q-flux actually reduces the OLR efficiency by concentrating the convection in a smaller area. For the two coldest cases in the Q-flux experiment, the OLR efficiency is very high and contributes significantly to the cooling in those cases. At the warmest temperatures the OLR efficiency declines as the SST contrast declines and explains much of the greater sensitivity of the warmest climates. Most of this reduced OLR efficiency at high temperatures is produced in the subsiding region, where the water vapor path is increasing (Figure 3.6d).

To summarize, focusing on the intermediate climates with SST between 300 and 309 K, we see that the primary mechanism whereby Q-flux cools the mean climate is by increasing the OLR efficiency, the amount of OLR generated for a given mean SST value. OLR efficiency can be increased three ways: (1) by increasing the SST contrast between dry subsiding regions and warm convective regions. (2) by increased drying of the troposphere in the subsiding region, further decreasing the greenhouse effect, and (3) by increasing the subsiding fraction, as regions of downward motion have drier tropospheres, and the smaller greenhouse effect leads to more efficient OLR. Since the free troposphere temperature is similar everywhere in the tropics, the air temperature is determined by convection occurring over the warmest water. Since at tropical temperatures most of the OLR comes from the atmosphere, by increasing the SST contrast the mean surface temperature can be decreased while the OLR changes relatively little. The longwave emission from the atmosphere is largely determined by the temperature at the emission level and the water vapor above that (Hartmann et al., 2022b; Jeevanjee & Fueglistaler, 2020). The OLR efficiency in the cold subsiding region is affected by the relative humidity and temperature of the free atmosphere above, but also by the coldness of the surface and boundary layer temperatures. For fixed boundary layer relative humidity, cooling the surface increases the longwave efficiency because the cooler boundary layer contains less water vapor.

3.3.5 Cloud Response

In Figure 3.4 we saw that the changes of OLR and absorbed shortwave in response to the addition of Q-flux are much larger for the cold regime (<300 K), but much smaller for the intermediate and warm (>309 K) regimes. The large changes in the cold regime are driven by low cloud changes. In this section, we look at the cloud contribution to the changes in reflected short-wave radiation.

Figure 3.8 shows several variables, averaged over the coldest 20% of SSTs, a useful focus for understanding the change in clouds in the cold regime. Figure 3.8a shows the albedo and low cloud fraction. In the cold regime, Q-flux causes a drastic increase in both albedo and low cloud fraction. As shown in Figure 3.8b, this translates to a large increase in shortwave cloud radiative effect (SWCRE), and a small changes in longwave cloud radiative effect (LWCRE). The increase in low clouds corresponds to a large increase in inversion strength compared to the case without Q-flux, as shown in panel 3.8c. Panel 3.8c shows both the estimated inversion strength (EIS) (Wood & Bretherton, 2006), and the lower troposphere stabilty (LTS) (Klein & Hartmann, 1993). Panel 3.8d shows the water vapor path (WVP) scaled by 1000 and liquid water path (LWP). The WVP is particularly low for the cold regime, while the LWP is enhanced there. As the insolation is increased and the climate warms, the WVP above the boundary layer increases, which increases downwelling longwave radiation that could suppress the low clouds (Schneider, Kaul, & Pressel, 2019; Bretherton & Khairoutdinov, 2015; Eastman & Wood, 2018).

To summarize, in the cold regime Q-flux induces a large increase in low clouds that correlates with an increase in inversion strength and a large decrease in temperature. Low temperature and high inversion strength both favor low cloud abundance through thermodynamic and dynamic mechanisms (Bretherton & Blossey, 2014; Bretherton & Khairoutdinov, 2015). The transition from the cold regime to the intermediate regime is marked by a large decrease in low clouds corresponding to decreasing estimated inversion strength (EIS), warmer SST and an increase in WVP above the boundary layer. These responses are all in accord with our general understanding of low clouds in the atmosphere.

In the intermediate regime, the change in low clouds from the control experiments to the Q-flux experiments is small due to three main competing effects: (1) for the same insolation, the subsiding region is colder in the case with Q-flux, and this favors more low clouds, (2) the Q-flux increases the SST contrast, which leads to a stronger inversion above the boundary layer, which if acting alone would lead to an increase in low clouds, and (3) the Q-flux leads to a drier troposphere, which increases entrainment drying, which would decrease the low clouds if acting alone (Bretherton & Blossey, 2014). For warmer temperatures (> 300 K) entrainment drying plays a larger role than in the cold regime, and the low clouds respond only weakly to Q-flux.

Finally, for the very warm temperatures (> 309 K), the low cloud fractions and albedo decrease dramatically as the SST contrast also declines. Associated with this breakdown of the SST contrast is a rapid increase in the water vapor path over the colder water (Figure

3.8d), which decreases the longwave cooling of the boundary layer clouds in the subsiding region. This rapid increase in water vapor path occurs at a higher insolation for the case with Q-flux, because the Q-flux cases are colder than the control cases. Thus at the 310 K transition, although the inversion strength remains, both the increased temperature and the reduced longwave cooling of the boundary layer act to reduce the low cloud abundance in the cold region.

The transition from the cold regime to the intermediate regime is dominated by the reduction in low clouds over the subsiding region and is therefore likely to be sensitive to the low cloud parameterization in the model. The transition, however, appears physically reasonable and consistent with previous studies. Specifically, Schneider et al. (2019) found a similar, drastic decline in stratiform clouds with warming using large eddy simulations (LES). There are several potential factors contributing to the decline in low clouds (Bretherton & Blossey, 2014). Schneider et al. (2019) highlight the importance of cloud top radiative cooling for generating the turbulence responsible for maintaining stratiform clouds. Eastman and Wood (2018) use observational data to address the competing influences of increasing inversion strength with changes in specific humidity: including, (1) stability, (2) the specific humidity just above the boundary layer, and (3) the column humidity in the free troposphere. The specific humidity immediately above the boundary layer impacts the efficiency of entrainment drying while the total column humidity impacts the downwelling longwave radiation at the boundary layer top. While increasing the inversion strength would lead to an increase in low clouds, increasing the specific humidity gradient leads to enhanced entrainment drying and a decrease in low clouds (Wood & Bretherton, 2006; Bretherton & Blossey, 2014). Cloud top radiative cooling and entrainment drying impact albedo through stratocumulus thinning and cloud lifetime respectively (Eastman & Wood, 2018).

Although the clouds do contribute to the overall cooling with Q-flux, apart from the cold regime ($<$ 300 K) the cloud change is small in comparison to other energy budget variables such as energy transport out of the warm region and increased efficiency of OLR in the cold region. If the clouds were responsible for the cooling, we would expect to see a large decrease in net shortwave radiation and a decrease in OLR of the same magnitude as

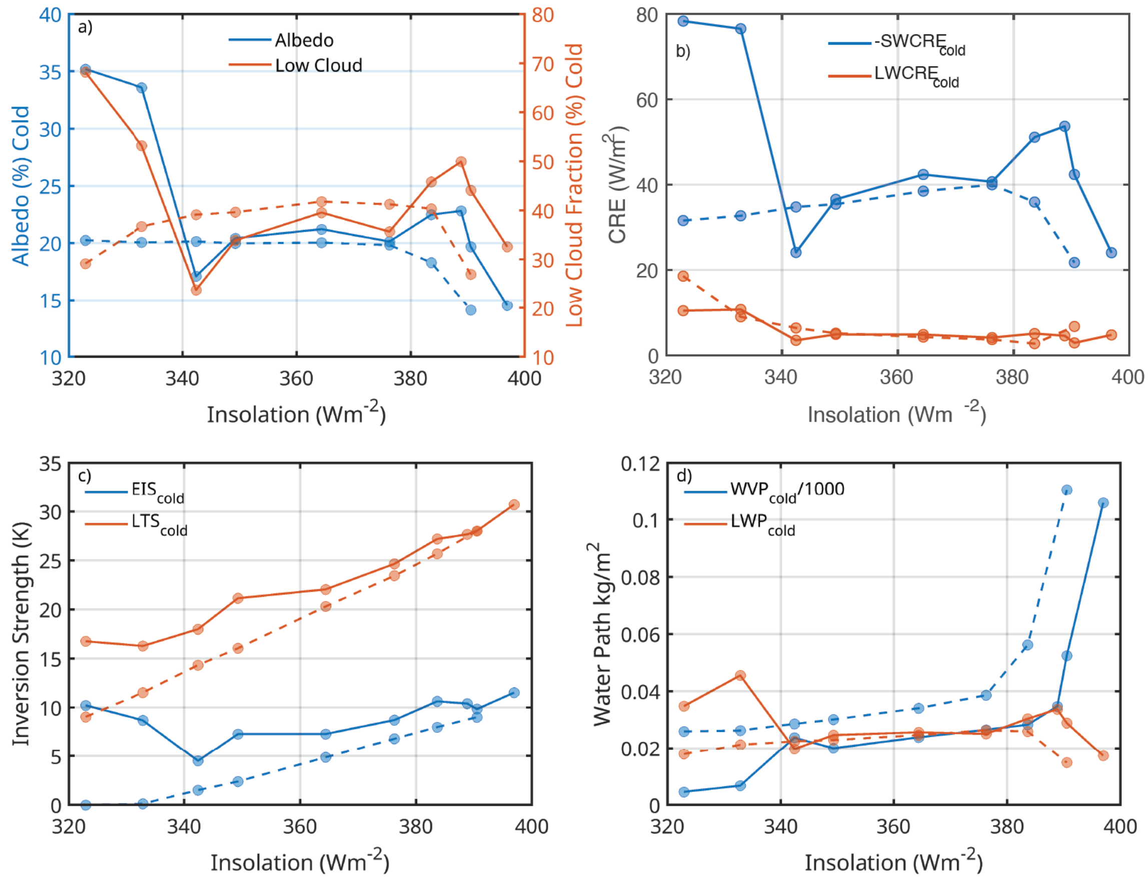

Figure 3.8: Key cloud variables averaged over coldest 20% SSTs: a) albedo and low cloud fraction (%), b) negative shortwave (-SWCRE) and longwave (LWCRE) cloud radiative effect, c) EIS and LTS, and d) water vapor path (WVP/1000) divided by 1000 for scaling and liquid water path (LWP) in kgm^{-2}. Note that SWCRE is plotted with reversed sign for clarity. Dashed line indicate the control case and solid lines indicate the Q-flux case.

the sea surface temperature decreases. Instead, we see only a small decrease in OLR and net shortwave radiation. So, although the clouds do cool more in Q-flux cases, with the most change occurring in the hottest cases, they are not the main mechanism responsible for the decrease in global mean SST in response to Q-flux, except in cold cases before the transition from the cold regime to the intermediate regime.

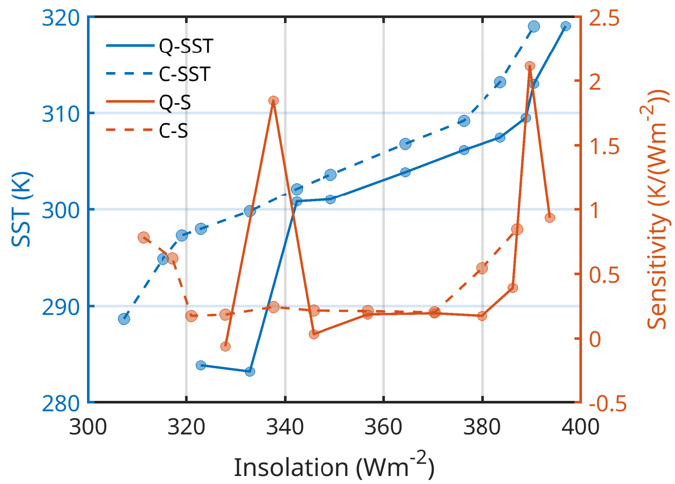

Figure 3.9: The blue lines show the global mean SST (K) versus insolation (Wm^{-2}), with the dashed lines representing the control cases and the solid lines representing cases with the Q-flux added. The orange lines represent the slope of the blue lines, or the change in SST per change in insolation (K/Wm^{-2}).

3.3.6 Sensitivity to Forcing

Adding the Q-flux results in a decrease in global mean SST when compared to the control simulation with the same forcing. One might ask if this cooling has any effect on the sensitivity of the climate to forcing. We are changing insolation rather than carbon dioxide levels to vary the climate. Here, we will define our sensitivity to forcing as

$$S = \frac{\Delta SST}{\Delta I} \tag{3.10}$$

where ΔSST is the change in global mean sea surface temperature and ΔI is the change in insolation. This definition is not consistent with the way global sensitivity is calculated, since the insolation change is not the forcing change. Some fraction of the insolation is reflected, so that the forcing is smaller than the change in insolation. We seek here not to provide a precise estimate of sensitivity, but merely to show that significant changes in sensitivity occur at the regime transitions in our experiments.

Figure 3.9 shows the sensitivity defined by (3.10) for the cases with and without the Q-flux. For the cases with intermediate global mean SSTs (300-309 K), the implied sensitivities of the control and the Q-flux cases are similar. While Q-flux cools the climate in comparison to the control case, it does not result in substantially different sensitivity to insolation increases for most values of insolation. Exceptions to this occur at the transition from the cool to the intermediate regime, and when moving to the warmest cases. For the warm transition near 310 K the Q-flux cases make a much more rapid transition and at higher insolation values, although similar temperatures. Both the control cases and the Q-flux cases see a sudden change in sensitivity after reaching 310 K. This shift is attributed to the increase in water vapor that causes the subsiding region to become less efficient at cooling to space (Figure 3.8d).

While the different regimes affect the global mean SST, they do not affect the overall change in sensitivity within regimes when comparing the Q-flux cases to those without. Instead, at each regime transition, there is a large spike in sensitivity as an SST cooling mechanism is lost. Moving from the cold regime where the clouds dominate to a climate where greenhouse effect dominates, there is a sudden decrease in cloud fraction that results in a large global mean SST increase associated with a decrease in the SST contrast. The cooling response to Q-flux in the intermediate regime comes from the increased OLR efficiency from the reduced greenhouse effect associated with the SST contrast. When the SST becomes warm enough that the greenhouse effect begins to grow in the subsiding region, the cooling associated with the SST contrast is lost and another spike in sensitivity occurs in the transition to warm climates where the radiator-fin cooling mechanism becomes less efficient.

To summarize, although adding Q-flux results in cooler global mean SSTs compared to the corresponding control case, Q-flux does not result in large changes to the implied climate sensitivity, except at the transitions between the cold and intermediate, and the intermediate and warm regimes. Adding Q-flux delays the onset of the high sensitivity associated with very warm climates until higher values of insolation, but the temperature threshold remains unchanged at about 310 K.

3.4 Comparison to ENSO Observations

In this section we will use ERA5 reanalysis data to compare behaviors of the model with nature. The most likely real-world analog for these experiments is the El Niño Southern

Oscillation (ENSO) in which the east-west gradient of ocean heat transport varies from a small gradient in El Niño years, similar to our control experiments, and a large gradient in La Niña years (Figure 3.1), similar to our Q-flux experiments. We use monthly average, one degree horizontal resolution data from ERA5 (Hersbach et al., 2020a) from 1990 to 2020. The variables used are the surface energy budget terms, top of the atmosphere energy, and sea surface temperature. We use the vertically integrated divergence of energy transport (DAT) from a mass-consistent data set (Mayer, Mayer, & Haimberger, 2021).

We again use the Niño 3.4 index to represent the phase of ENSO, with positive values indicating an El Niño phase and negative values indicating a La Niña phase. We use reanalysis data averaged from 10S to 10N over tropical oceans to get a sense for how key variables vary zonally and how that changes between ENSO phases. Figure 3.10 shows top of the atmosphere energy variables and the SST binned by standard deviations of the Niño 3.4 index and longitude. Note that for the energy budget terms, the color scale is arranged so that the changes can be directly compared. This shows in particular the larger changes in atmospheric energy divergence compared to the longwave and shortwave terms. In the Q-flux experiments, we saw that the hottest SSTs did not increase as much as the coldest SSTs cooled. We see a similar phenomenon in the reanalysis data, as shown in Figure 3.10a. Increased upwelling cools the coldest SSTs, but there is a much smaller decrease in the hottest SSTs. To better understand what is affecting the change in SSTs, we look at the top of the atmosphere energy budget terms.

The energy budget terms also show similar variations as our idealized experiments. Figure 3.10b, shows that OLR decreases only modestly in the La Niña phase, compared to the DAT changes. In Figure 3.10d, the net shortwave at the top of the atmosphere shows only small changes over the coldest SSTs, again compared to DAT changes. Over intermediate and warm SSTs, OLR and SWnet show individual changes on the order of 20 Wm^{-2} in which the longwave and shortwave effects offset each other. Among the energy budget terms, DAT, shown in Figure 3.10c, sees the largest change between La Niña and El Niño phases in the Eastern Pacific. There is an increase in convergence of atmospheric energy flux over the coldest SSTs in the La Niña phase and an increase in export from the warmer SSTs. This is consistent with the increased SST gradient leading to a stronger circulation and increased atmospheric transport.

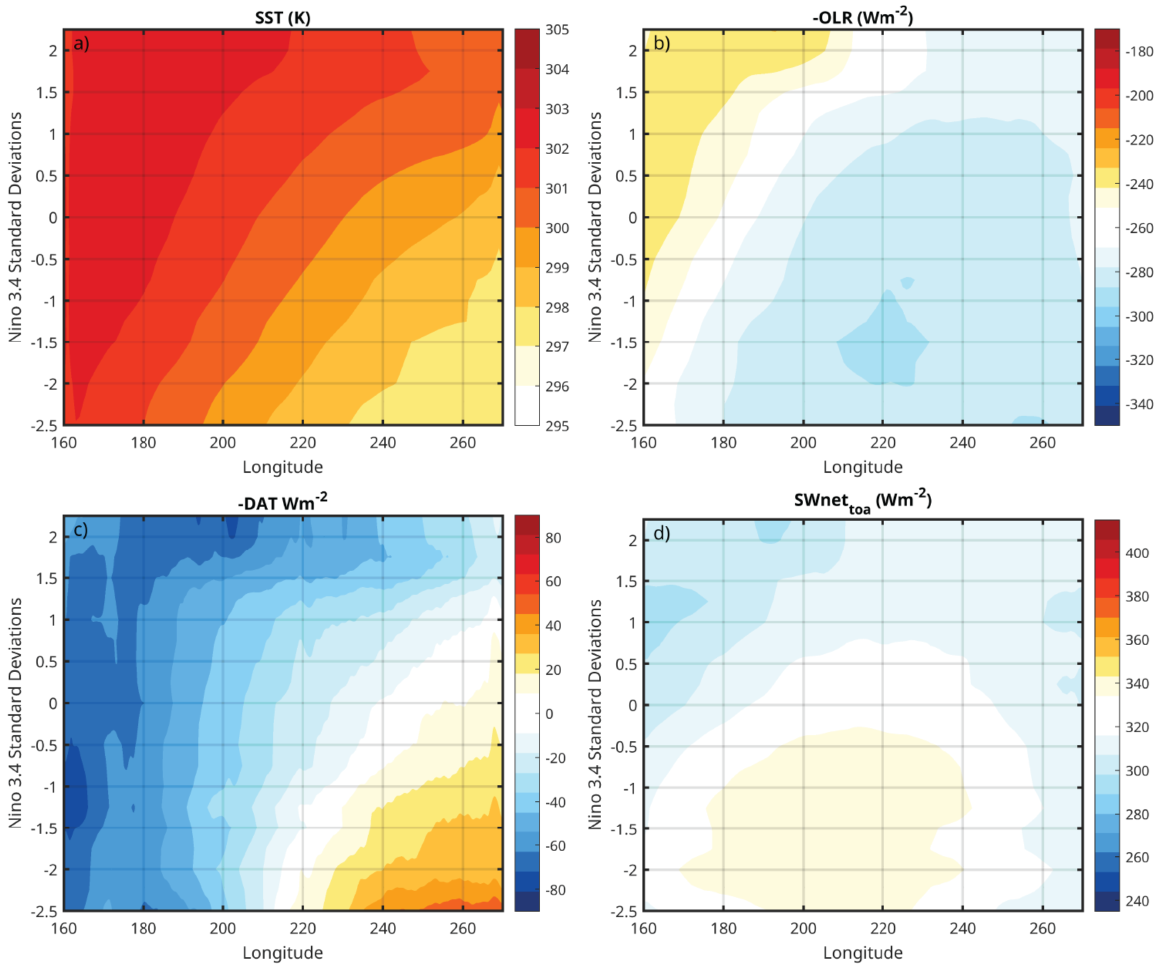

Figure 3.10: Panel a) shows the SST (K) binned by Niño 3.4 standard deviations and longitude, with 0.25 K contour intervals. Panels b-c show top of the atmosphere energy budget terms (b) OLR, (c) DAT, and (d) NetSW with 10 Wm^{-2} contour intervals. Data over land is removed so that we use the meridional mean over tropical waters from -10 degrees S to 10 degrees N.

Despite the larger changes in SST in the cold region, the OLR and SWnet in this region change modestly compared to the changes in DAT. The warmest SSTs appear to be constrained by an increase in energy export out of the region in both cases.

Significant differences exist between our idealized modeling results and the ENSO cycle represented in the reanalysis data. In our modeling experiments, insolation is uniform and there is no systematic energy transport from the tropics toward the poles. In nature, there is a systematic atmospheric energy transport out of the tropics to the mid latitudes. In nature, much of the subsidence occurs in the subtropics under the Hadley Cells and in the presence of rotation.

3.5 Summary

Ocean heat transport in the form of Q-flux has been added to a global radiative equilibrium model of an atmosphere above a slab ocean. The global mean temperature is reduced by the addition of Q-flux. Adding Q-flux leads to stronger SST contrast by cooling the coldest SSTs, which leads to stronger circulation and stronger winds. Stronger winds also help the warmest SSTs stay approximately unchanged despite the added heat in the warm region. The warm region is prevented from warming in response to Q-flux by increased export of energy from the region of upward motion over the warmest SSTs. While the atmosphere exports more heat from the warm pool, the large-scale circulation warms and dries the upper troposphere in the subsiding region. This contrast produced by Q-flux increases the OLR achieved for a particular mean SST, which produces a cooler planet for the same insolation value, even in the absence of cloud effects.

The response of the model to adding Q-flux depends on the regime of global mean SST. For relatively cold mean SST, Q-flux causes a transition to a very cold, high-SST-contrast state. Increased low clouds in the cold region are the main factor in cooling the global mean SST and increasing its contrast in these cold states. As the insolation is increased from these cold cases, an abrupt transition occurs where the low cloud reflectivity decreases, the SST contrast decreases and the mean SST increases. Above this cold transition mean SST values are near those of the current tropics, and cloud changes play a small role as the insolation is further increased.

A second transition occurs near mean SST values of 310 K. At this point the SST contrast declines and the climate becomes much more sensitive to further increases in insolation. Because it cools the mean climate, Q-flux delays this transition to a warm and sensitive climate to higher values of insolation, but again the transition is more abrupt than in the case without Q-flux. Oceanic heat transport results in stronger convective organization, promoting both the increase in low clouds seen in the coldest case and the reduction in the greenhouse effect over the subsiding region for the intermediate cases most like the current tropics.

Despite the large changes in circulation from the control to the Q-flux experiments, for cases with mean SST similar to the current tropics (300-309 K) there are only small changes in cloud fraction and albedo as the climate is warmed. The role of clouds is probably strongly model dependent, and cloud feedbacks could play a more significant role in a different model. Our main conclusions, however, can be shown through clear-sky values alone, which are more robust across different models.

Major caveats regarding these results are that the parameterizations affecting the low cloud amount in the simulations are uncertain and likely important to the regime behavior of the model. Also, the fixed position of the convective region and the lack of meteorology driven by rotation likely result in a subsiding region that is drier than found in nature. It is nonetheless true that the SST contrast is as important to the radiator fin mechanism as the relative humidity contrast, because of the strong dependence of boundary layer humidity on temperature.

To summarize, we have shown that

- Adding a Q-flux that mimics ocean heat transport cools the global mean SST by cooling the coldest SSTs.

- Although ocean heat transport provides heating under the warmest SSTs, the warmest SSTs do not increase much compared to the control case without Q-flux.

- Although the warm, ascending region sees changes in both longwave and shortwave radiative effects, the net radiation change is small; instead, the atmospheric energy transport out of the ascending region increases to balance the convergence of Q-flux.

- For cases most like the current tropics, the OLR over the coldest SSTs only decreases a small amount despite the large decrease in SST, because the air temperature is tied to the warmest SSTs, and increased circulation leads to a drier mid troposphere in the subsiding region, which decreases the greenhouse effect and allows for more efficient longwave cooling to space.

- Although the Q-flux cools the global mean SST, it does not affect the climate sensitivity of the model. It does, however, delay the transition between SST regimes, particularly the onset of the higher sensitivity warm climates.

- Observations of ENSO events show a similar breakdown of the most important terms as in our Q-flux experiments.

Chapter 4

SEA SURFACE TEMPERATURE AND SHALLOW ATMOSPHERIC CIRCULATIONS

4.1 Introduction

Understanding the atmospheric circulation in the tropics and its interaction with convection and radiation is critical to the global radiation budget and climate sensitivity (Bony et al., 2015; Dong et al., 2019; Armour et al., 2024b). While the predominant view of the tropical circulation envisions a single deep cell, shallow circulations are known to occur in the tropics in both observations and reanalysis datasets, particularly the shallow meridional circulation (SMC) on the flanks of the intertropical convergence zone (ITCZ) in the East Pacific (Zhang et al., 2004; Zhang, Nolan, Thorncroft, & Nguyen, 2008b; Schulz & Stevens, n.d.; Huaman, Schumacher, & Sobel, 2022). These shallow circulations are characterized by strong return flow above the boundary layer and are often identified in regions with strong sea surface temperature gradients (Zhang et al., 2004). Fläschner, Mauritsen, Stevens, and Bony (2018) have shown that shallow circulations can have a strong effect on the distribution of precipitation and its response to warming in climate models.

Several studies have investigated the mechanisms underlying these shallow circulations. One potential driver of this shallow circulation is boundary layer pressure gradients created by SST gradients, as in a sea-breeze (Nishant, Sherwood, & Geoffroy, 2016; Lindzen & Nigam, 1987). Other studies find boundary layer radiative cooling to be the best indicator of shallow circulation strength (Nolan, Zhang, & Chen, 2007; Naumann, Stevens, Hohenegger, & Mellado, 2017). Nolan et al. (2007) specifically address the direct impact of sea surface temperature gradients and longwave cooling, and find that longwave cooling is the primary driver. While they found that SST gradients were not strong enough to explain the shallow circulation strength through their direct impact on boundary layer pressure gradients, they acknowledge that the longwave cooling increases in experiments with stronger SST gradients due to the effect of SST gradients on the relative humidity distribution. Janssens, George, Schulz, Couvreux, and Bouniol (2024) find, instead, that shallow convection is the primary driver of tropical shallow circulations. In their study the SST gradients are relatively weak, and they do not speculate on the potential effects of SST on shallow convection.

Several prior studies using a simplified mock-Walker simulation setup designed to emulate the overturning circulation along the equator have found that a double-cell structure develops in these simulations (Grabowski, Jun, & Moncrieff, 2000; Larson & Hartmann, 2003; Yano, Grabowski, & Moncrieff, 2002; Lutsko & Cronin, 2018). These studies focus on explaining the development of the shallow circulation as primarily being driven by radiative cooling in the subsiding region or shallow convective heating in the rising portion of the shallow cell. Diagnostically, it is difficult to say which of these factors is the primary control on the development of shallow circulations, as both are required to sustain a shallow circulation cell energetically. This problem has recently been addressed in the context of mock-Walker circulations in a convection permitting model by Lutsko and Cronin (2024b). They find that a double-cell circulation always develops in this model when surface temperatures are higher than about 300K, and that the development of the double-cell structure is encouraged by SST gradients. Adding moisture to the subsiding region or fixing the radiative cooling reduces the radiative cooling mechanism and moves the development of the double-cell structure to a higher mean temperature closer to 305K. This suggests that a mechanism other than radiative cooling also encourages a double-cell structure with a strong shallow circulation when the surface temperature is warm.

Many previous studies have investigated the relationship between SST gradients and circulation. These studies vary from more general interactions between sea surface temperature and circulation strength to specific effects on the top and bottom heaviness of the distribution (Lindzen & Nigam, 1987; Sobel & Neelin, 2006). Back and Bretherton (2009) use a linear mixed layer model to find that sea surface temperature gradients lead to shallow convergence and convection.

Our goal here is better understand the comparative roles of mean SST and SST gradients in generating shallow circulations in a tropical context. To do this we use a simplified framework of a global climate model with uniform insolation and no rotation, emulating a global tropical world. We use fixed SST simulations and vary the mean SST and the SST gradient in the domain and compare the shallow versus deep circulations in a suite of experiments in which the mean SST and SST gradient are varied independently. We diagnose the relative roles of radiative cooling and convective heating in driving shallow circulations. We find that SST gradients are important in driving shallow circulations and that the primary energetic support for these shallow circulations is radiative cooling. As the mean SST is increased, however, we see an increasing role for shallow convection in driving shallow circulations. We diagnose the reasons for the increased shallow convection with a convective plume model.

The model and experimental design are described in Section 4.2. The circulation response to mean SST and SST gradient are described in Section 4.3. The effects of longwave cooling on the circulations are described in Section 4.4. Diagnosis and interpretation of the effect of shallow convection on shallow circulation strength are given in Section 4.5. A summary is provided in Section 4.6.

4.2 Model and Experiments

These experiments use Geophysical Fluid Dynamics Laboratory's (GFDL) AM2.1 (Anderson et al., 2004). We use a grid with 2 by 2.5 degree horizontal resolution and 32 vertical levels. We simplify the model by using uniform insolation, no rotation, and prescribed SST. The experiments are spun up until equilibrium, and extended for two decades after equilibrium.

The intention of these experiments is to evaluate the effect of changes in both mean SST and SST range. We prescribe SST with a spatial distribution of wavenumber 1 and mean of 299, 302, 303.5, and 305 K. Experiments using these mean SSTs are run with SST ranges of 2.5, 5, 7.5, 10 and 15 K. Each case is named by its global mean SST and SST range. For example, the SST for the case F302-5, is shown in Figure 4.1, has a global mean SST of 302 K and a SST range of 5 K.

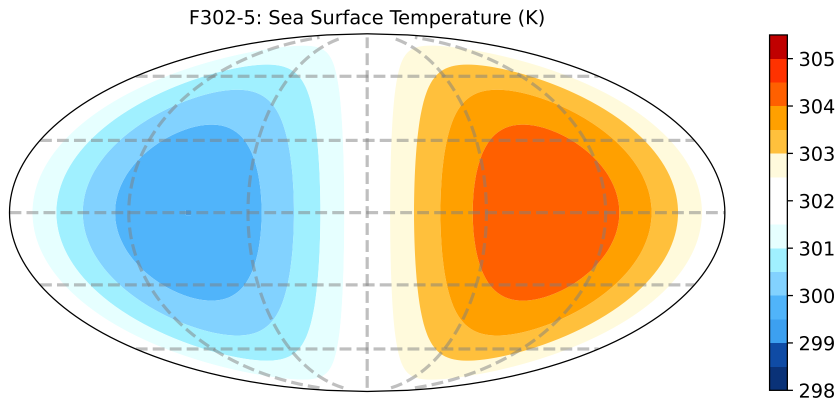

Figure 4.1: Example of prescribed sea surface temperature (K) in latitude and longitude for F302-5, or the case with a global mean SST of 302 K and a range of 5 K.

4.3 Circulation and Streamfunction

The circulation can be visualized through a mass streamfunction calculated for each case, as shown in Figure 4.2. Here, we organize the circulation in column relative humidity (CRH) area space, such that the stream function is integrated flowing from dry to moist regions. The CRH area fraction is then given by

$$\Phi_A(CRH) = \int_0^{CRH} f_A dCRH \tag{4.1}$$

and thus the streamfunction is given by

$$\Psi(\Phi_A, p) = \frac{A_E}{g} \int_0^{\Phi_A} \omega(p) d\Phi'_A \tag{4.2}$$

This is the same expression used in Hartmann and Dygert (2022b) with CRH area fraction in place of SST area fraction. CRH was chosen here because in the cases with small SST gradients the circulation is not well organized by SST, and CRH better captures the contrast between regions of rising and sinking motion. In those cases with larger SST contrast, using CRH area fraction or SST area fraction yield similar results.

In Figure 4.2 the mean SST increases from left to right and the SST contrast increases from bottom to top. In all cases, as the global mean SST increases the upper cell weakens and the shallow cell strengthens. The weakening of the upper cell is consistent with studies finding that the tropical overturning atmospheric circulation will weaken under warming, primarily because of the increasing dry static stability (Knutson & Manabe, 1995; Vecchi & Soden, 2007). Figure 4.2 also shows that as the range of SST increases from bottom to top, the shallow circulation strengthens and the circulation takes on a more distinct double cell structure. As the SST range increases, the upper cell tends to shrink toward higher CRH such that the upper cell is strong only over the highest CRH area fractions. So increasing the global mean SST and the SST range both increase the strength of the shallow cell and the double-cell structure of the circulation.

As shown in the bottom row of Figure 4.2, the circulation in the cases with an SST range of 2.5 K is particularly top heavy and does not have a strong shallow cell. The weak SST gradient is not sufficient to produce strong large-scale organization, given the internal variability of the simulations, and these cases are the least consistent with the others. Even so, the upper cell still rises and weakens with warming, and the circulation starts to show a distinct double cell structure by the warmest experiment, F305-2.5.

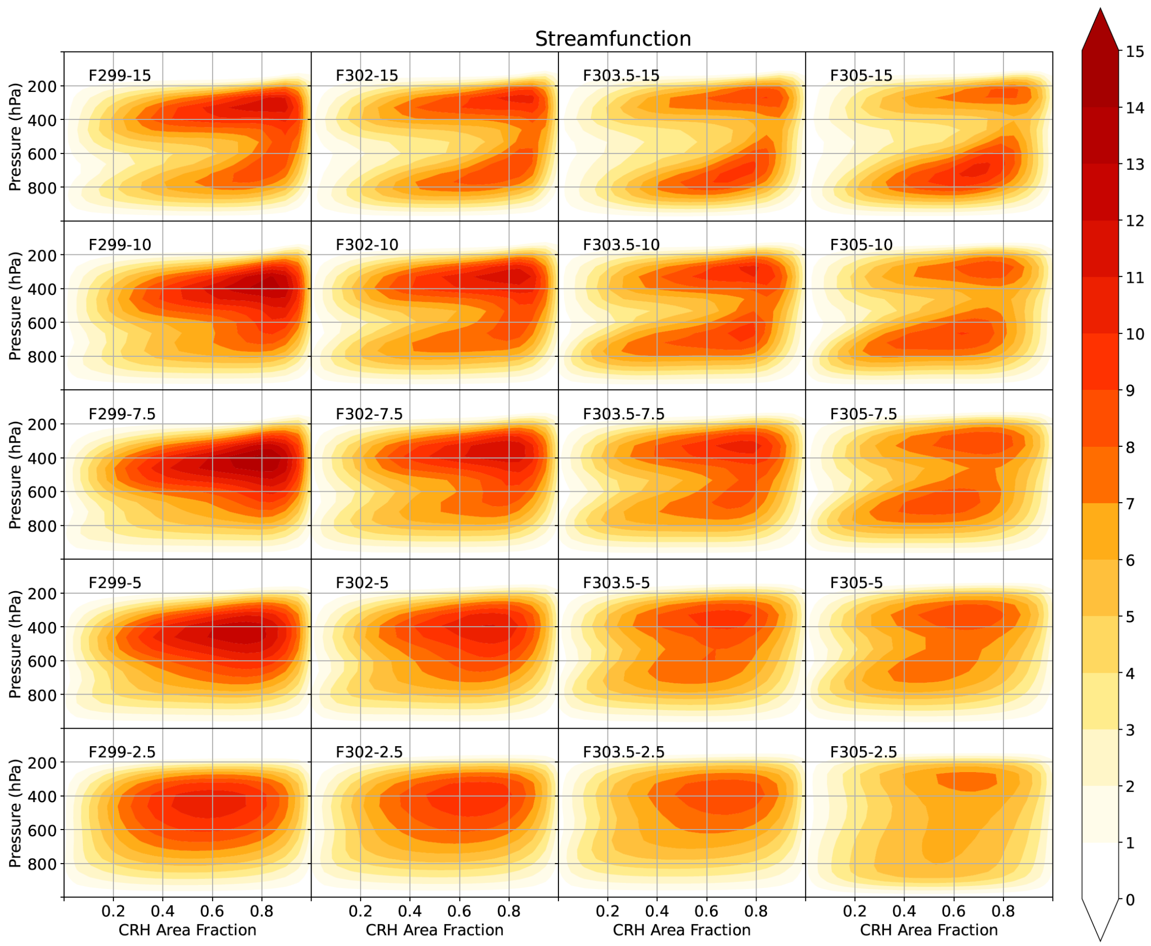

Figure 4.2: Streamfunction for each case shown in pressure (hPa) and column relative humidity (CRH) area space (%). The global mean SST of each case increases from left to right, and the SST range increases from bottom to top.

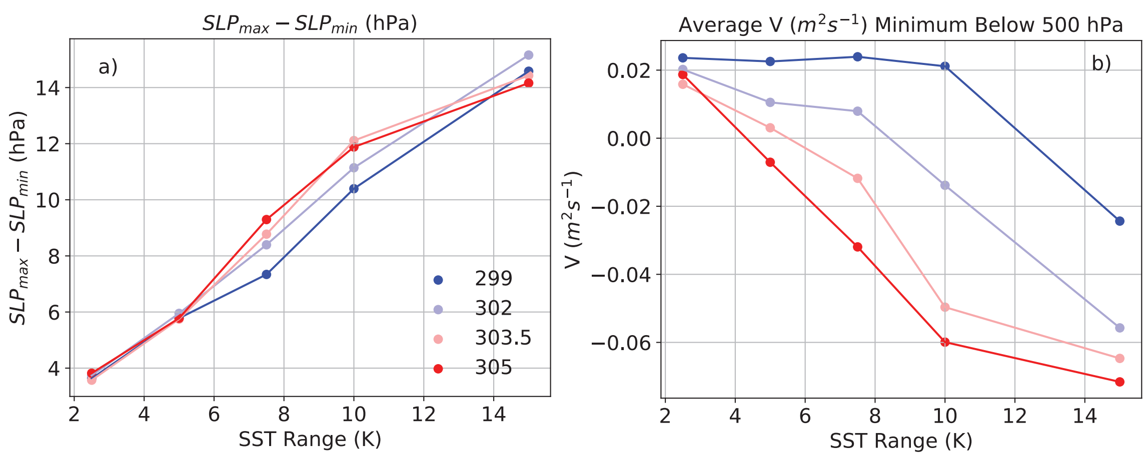

Figure 4.3: a) Surface pressure difference from minimum to maximum CRH as a function of SST contrast for each mean temperature. b) minimum horizontal area velocity (V) averaged over all CRH values for each mean temperature.

Further detail on the response of the circulation to SST is shown in Figure 4.3. Panel a shows that as the SST contrast is increased, the pressure contrast between driest (coldest) and wettest (warmest) portions of the domain increases linearly, with relatively modest sensitivity to mean temperature. This might be expected from the relation of SST to surface pressure predicted by hydrostatic considerations (Lindzen & Nigam, 1987). One would expect these increasing surface pressure gradients to drive a stronger near-surface flow toward warmer SST.

A more direct measure of the relative strength of the shallow circulation is shown in Figure 4.3b. Here, we show an effective "horizontal area velocity" derived from our expression for streamfunction shown in Equation 4.2:

$$V = -g \, \frac{d\Psi}{dp} \tag{4.3}$$

V represents the flow from low to high CRH area fractions, where negative values represent a return flow from high CRH values to low CRH values. Because the shallow circulation is characterized by a strong return flow, we use the strength of this return flow to represent the strength of the shallow circulation. Strong negative values represent a strong return flow and strong shallow circulation. We calculate this index by finding the minimum of V below 500 hPa for each CRH value and taking the average across the full CRH range. This quantity is shown in Figure 4.3b for each case plotted against SST range. As in Figure 4.3a, each line represents a different global mean SST. The strength of the return flow increases with both mean SST and SST range. This figure specifically highlights that warming the SST, without increasing the SST gradient, increases the return flow and shallow circulation strength. For the coldest case, the return flow strength only increases at the highest SST range, 15 K. In experiments with already strong shallow circulation strength, such as F303.5-7.5, increasing either the mean SST or SST range appears to have diminishing returns. Increasing either the SST range or warming the mean SST strengthens the shallow circulation, and the strongest shallow circulations occur in experiments with both warm mean SSTs and large SST ranges.

Although we are characterizing these experiments by their mean SST and their SST

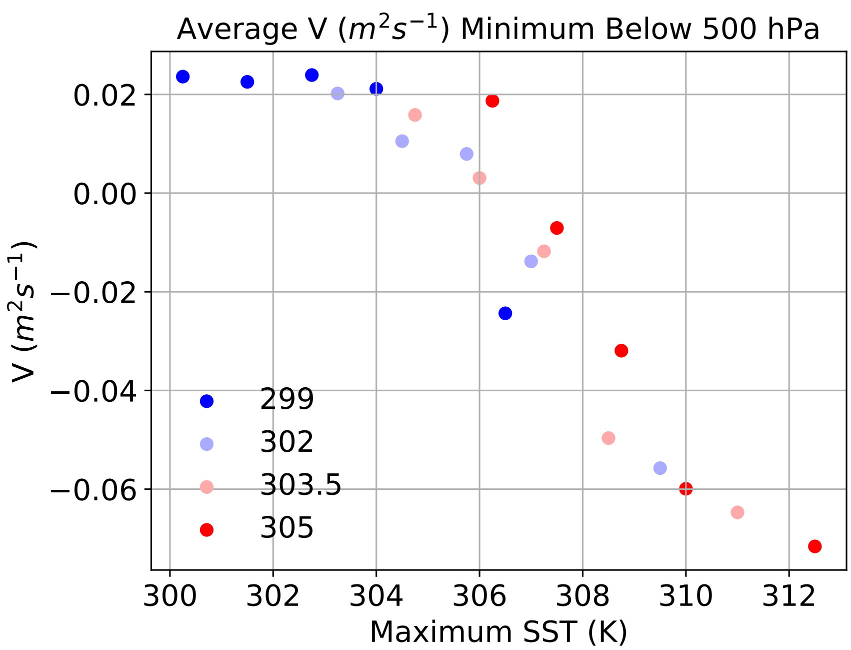

Figure 4.4: Minimum horizontal area velocity (V) averaged over all CRH values for each mean temperature, plotted against maximum SST. Global mean SST is represented by color.

range, it is important to note that changing either the mean SST or the SST range will also change the maximum SST. The maximum SST is particularly important in the tropics, as the tropospheric air temperature is primarily set by the warmest SSTs (Sobel, Nilsson, & Polvani, 2001). Figure 4.4 shows the same index for shallow circulation strength used in 4.3 plotted against the maximum SST for each experiment. The return flow strengthens with maximum SST. This is consistent with the strongest shallow circulations occurring in experiments with both warm mean SSTs and large SST ranges.

4.3.1 Relative Humidity

The relative humidity is closely tied to both the circulation and the potential mechanisms that drive it. Figure 4.5 shows contours of relative humidity (%) in pressure versus CRH area, similar to Figure 4.2. An interesting feature of the relative humidity distribution is a deep secondary moist layer above the near-surface boundary layer. This layer is capped by a sharp transition to much drier air on a surface that slopes downward from the moist to the driest part of the domain. This layer becomes thinner and more moist as the SST gradient is increased. Although these models are highly idealized, this middle tropospheric moist layer can be found in observations and reanalysis data.

Zhang et al. (2008b) determined that well developed shallow circulation cells occur in the northern spring season over the East Pacific and west of Africa. We plot the relative humidity from ERA5 reanalysis (Hersbach et al., 2020b) for meridional cross sections in these regions and seasons in Figure 4.6. In each case a moist layer extends upward to about 600 hPa in the vicinity of the equator, above which is much drier air. This humidity profile is consistent with relatively abundant shallow convection but relatively sparse deep convection in these regions. Note that relative humidity as low as 10% appear in these climatological averages. The lack of deep convection is consistent with the fact that the SST in these regions is slightly less than the maximum SST in the Tropics, which determines the temperature profile above the boundary layer. This relatively shallow heating drives the strong shallow circulations that are observed in this season.

Figure 4.6d shows a cross-section of relative humidity averaged over 15N to 15S and plotted versus longitude. The tendency for moist layers to extend up to 600 hPa is seen, but the extremely low relative humidity seen in the meridional cross sections in 4.6a-c is washed out in this representation. The attainment of low humidity is helpful for the lower-tropospheric radiative cooling that balances shallow circulations.

In the summer season the SST north of the equator in the East Pacific warms up to temperatures comparable to the warmest temperatures in the Western Pacific. In this season much more deep convection occurs, as is consistent with the much deeper moist layer for September in the East Pacific shown in Figure 4.6c.

Later we will show enhanced shallow convection at temperatures just less than the maximum SST in our simulations. This shallow convection increases in strength with the mean SST, driving stronger shallow circulations in a warmed climate. We will then propose an analogy between the shallow convection that drives the shallow circulations in our experiments and the shallow convection that occurs in nature in regions of the tropics whose SST is slightly less than the tropical maximum.

Increasing the mean SST and increasing the SST gradient have different effects on the distribution of relative humidity. When increasing the SST range (bottom to top in Figure 4.5), the subsiding region dries and expands into higher CRH regions. This drying effect is particularly noticeable for the range of CRH area fraction from 0.6-0.8. For any given global mean SST, increasing the SST range consistently dries out the mid troposphere (around 600 to 400 hPa) in this CRH window. However, warming the global mean SST while maintaining the same SST contrast has the opposite effect. Warming moistens the layer between 800 to 400 hPa in the window from 0.6 to 0.8 CRH area fraction.

The moistening or drying of the 0.6-0.8 CRH window has important effects for radiative cooling and convection. If the air above the boundary layer moistens (dries), longwave cooling of the layer below can be suppressed (enhanced) (Hartmann et al., 2022a; Jeevanjee & Fueglistaler, 2020). Conversely, if the air above the boundary layer dries (moistens), convection is suppressed (enhanced). So, the change in relative humidity in this window indicates which mechanism is playing a more active role in strengthening the shallow circulation. When increasing the SST range and drying the window, the conditions are more favorable for longwave cooling. When warming the mean SST and moistening the window,

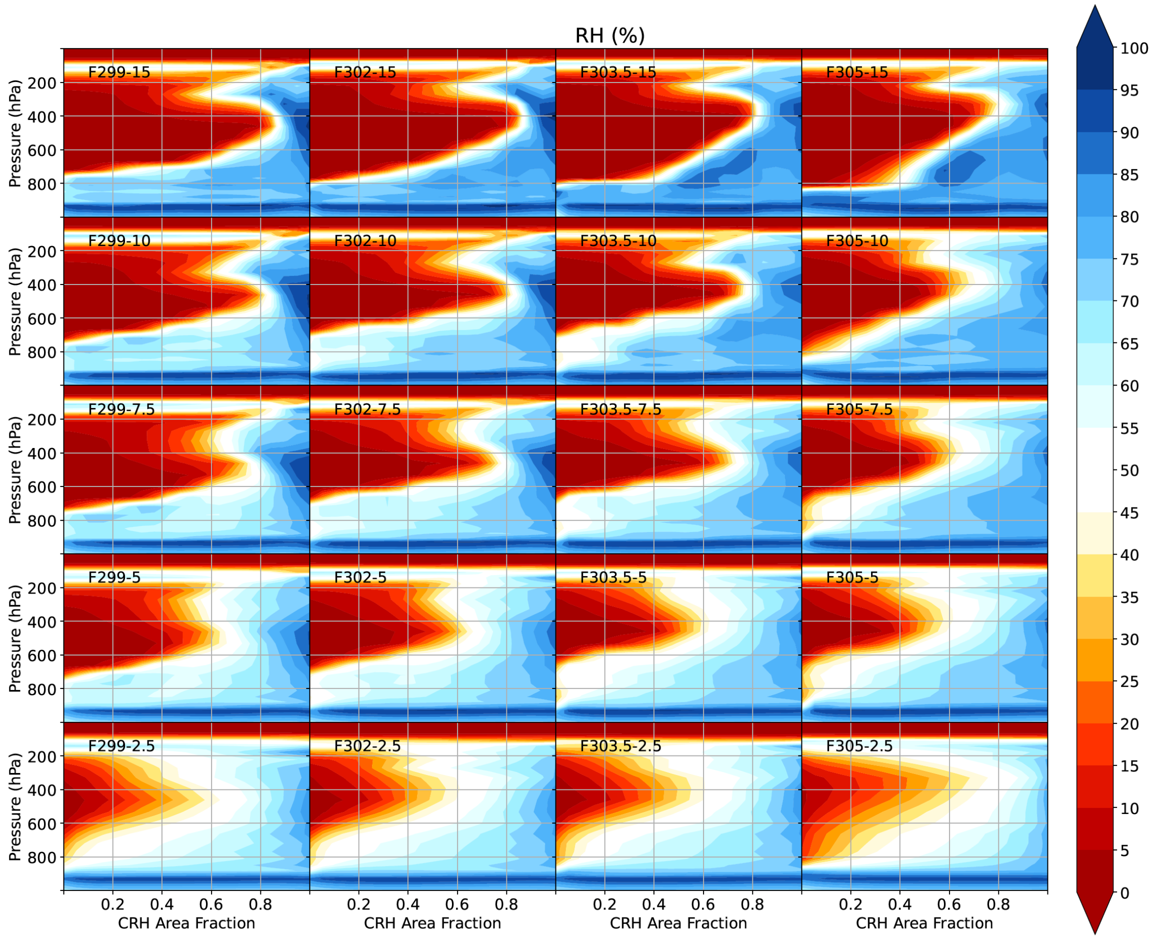

Figure 4.5: Relative humidity (%) for each case shown in pressure (hPa) and column relative humidity (CRH) area space (%). The global mean SST of each case increases from left to right, and the SST range increases from bottom to top.

the conditions are more favorable for shallow convection. It is relevant to note here that the relative humidity and these mechanisms feed back on each other, so it is difficult to parse which initially triggers the feedback loop. We will discuss in more detail the effect relative humidity on longwave cooling in Section 4.4 and on shallow convection in Section 4.5.

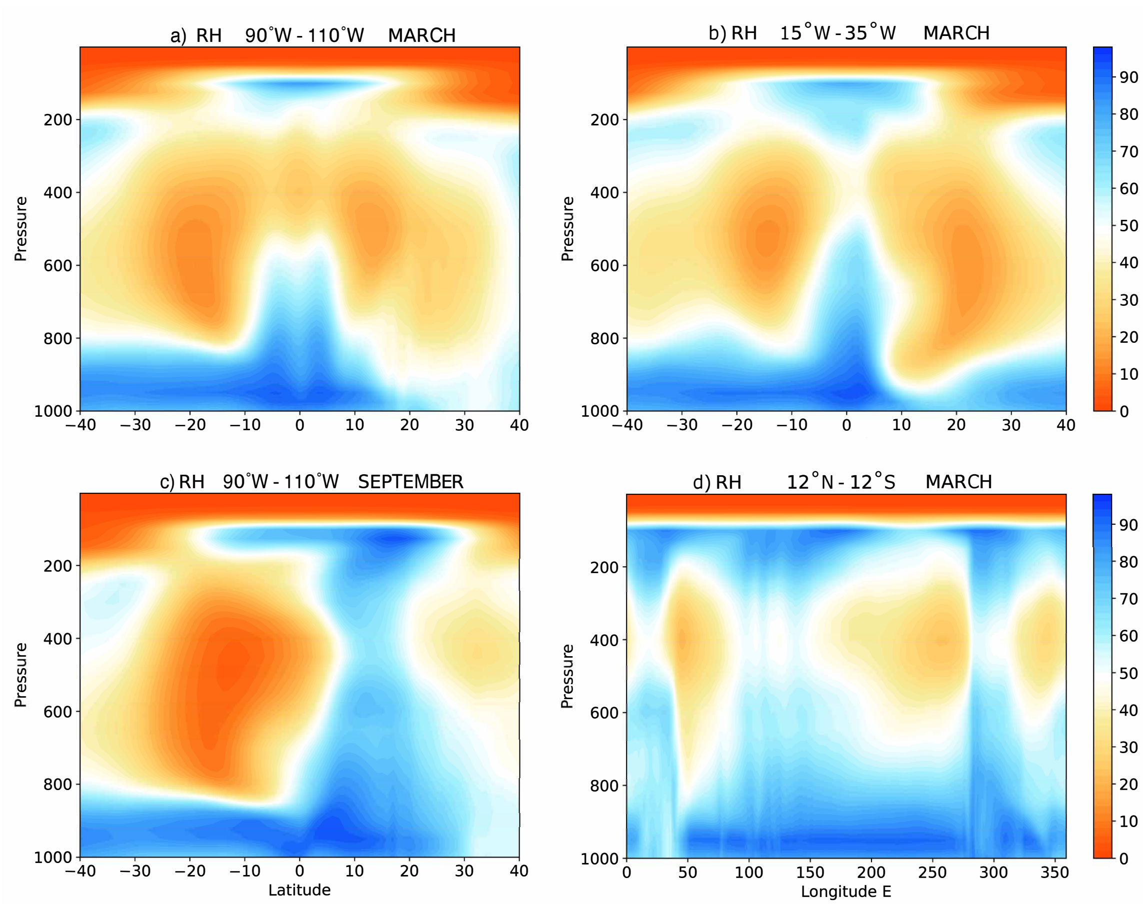

Figure 4.6: Climatological relative humidity from ERA5 reanalysis for a) Meridional cross section for longitudes from 90W to 110W for the month of March, b) as in a) except for 15W to 35W, c) as in a) except for September, and d) cross section of the averaged from 15N to 15S for March.

4.4 Boundary Layer Longwave Cooling

The longwave cooling above the boundary layer in the subsiding region is known to be strongly connected to the shallow circulation strength (Nolan et al., 2007). This relationship is characterized by a feedback between the longwave cooling and the shallow circulation strength through effects on the column relative humidity. As the shallow circulation strengthens, the troposphere of the subsiding region dries and the water vapor above the boundary layer decreases. Decreasing the water vapor path above the emission level leads to an increase in longwave cooling (Hartmann et al., 2022a; Jeevanjee & Fueglistaler, 2020). This increase in boundary layer longwave cooling in turn strengthens the shallow circulation (Nolan et al., 2007). Fildier, Muller, Pincus, and Fueglistaler (2023) similarly find the vertical moisture distribution to have a significant role in the long-wave cooling of the boundary layer, and specifically highlight the importance of moist intrusions from remote convection in setting the humidity above the boundary layer.

Figure 4.7 shows the longwave cooling for each case in pressure vs CRH fraction coordinates, similar to Figure 4.2. For a given global mean SST, as the SST range increases, the magnitude of the longwave cooling also increases. The band of enhanced longwave cooling above the moist layer also expands into the intermediate region between subsidence and deep convection with higher CRH. This enhancement in longwave cooling corresponds to increasing shallow circulation strength, as expected. In summary, we find that the longwave cooling above the boundary layer tends to respond more strongly to an increase in SST range rather than mean SST. This can largely be explained by the relative humidity distribution.

The strength of longwave cooling is directly proportional to the amount of water vapor above the emission level (Hartmann et al., 2022a; Jeevanjee & Fueglistaler, 2020; Fildier et al., 2023). Following Hartmann et al. (2022a), the cooling-to-space approximation for the longwave cooling rate at a specified emission level and wavelength, λ is a function of its temperature and humidity at that level as well as the vapor pressure path above that level

$$\frac{dT}{dt}|_{\bar{\lambda}} \approx -[\frac{\pi g}{C_p e} RH e_s(T) B_{\bar{\lambda}}] VPP^{-1} \tag{4.4}$$

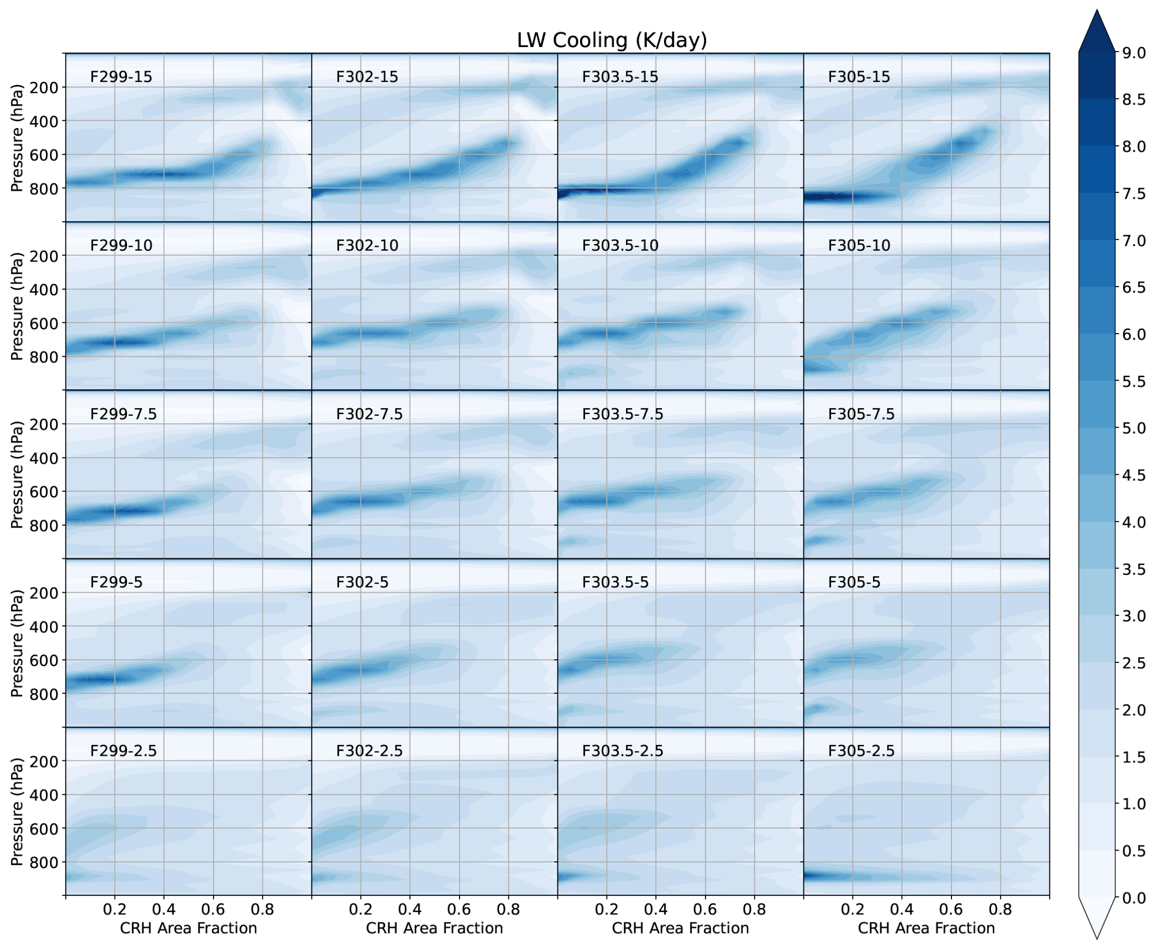

Figure 4.7: Longwave cooling (K/day) for each case shown in pressure (hPa) and column relative humidity (CRH) area space (%). The global mean SST of each case increases from left to right, and the SST range increases from bottom to top.

where

$$VPP = \int_0^p RHe_s(T)dp \tag{4.5}$$

From this expression, we see that the longwave cooling is stronger when the vapor pressure at the emission level is high and the vapor pressure path above the level of emission is small. Figure 4.8 shows (a) the longwave cooling, (b) the humidity component of the cooling to space approximation shown above by (4.5), (c) the temperature profile, and (d) the relative humidity profile for cases with a mean SST of 303.5K and the full range of SST gradients. Line plots versus pressure are shown for the CRH range of 0.6 to 0.8. As described in Section 4.3, the strength of the shallow circulation corresponds to an expansion of the shallow cell to higher CRH area fraction values. Specifically, we identified the CRH area fraction from 0.6-0.8 as showing particularly distinct differences between warming and increasing the SST range. So, to analyze the mechanism responsible for this strengthening, we show averages over 0.6-0.8 CRH area fractions. We show experiments with an SST of 303.5 K as a representative example of the changes with increasing SST range.

Panel 4.8a shows the longwave cooling rates averaged from 0.6 to 0.8 CRH area fraction in pressure coordinates. For this SST and CRH window, the longwave cooling peaks at 532 hPa. Panel 4.8b shows a peak in $RHe_s(T)VPP^{-1}$ at the same pressure level, indicating strong control of the vapor column on the longwave cooling. The VPP profile peak is a combined effect of both moistening below the emission level and drying above. In addition, because of the large-scale circulation and the weak temperature gradient in the tropics, the temperature of the free troposphere of the entire tropics is set by the warmest region. Figure 4.8c shows the temperature profiles for each SST range. As the SST range increases, the air temperature increases, and there is a corresponding increase in emission temperature, and thus an increase to the longwave cooling. Because the temperature and consequently the saturation vapor pressure increase with SST range, the reduction in VPP must be dominated by the decrease in relative humidity, shown in panel 4.8d.

The VPP above the boundary layer in the subsiding region decreases with increasing SST range. Because the longwave cooling is inversely proportional to the VPP, the longwave cooling is then enhanced with increasing SST gradient. Because the longwave cooling impacts the shallow circulation strength, which in turn impacts the drying above the boundary layer, it is difficult to say which is causing the other. However, there is a clear trend in the changes in longwave cooing and VPP across changing SST distributions.

In these experiments, increasing the SST range strengthens the large-scale circulation, dries the mid troposphere in the subsiding region, and increases longwave cooling. So, following the initial drying from the increase in SST range, we see a feedback between the longwave cooling, shallow circulation strength, and humidity of the subsiding region:

1. Drying the subsiding region strengthens the longwave cooling above the boundary layer.

2. Longwave cooling strengthens the shallow circulation.

3. Moisture transport away from the subsiding region is enhanced, and the vapor pressure above the boundary layer decreases.

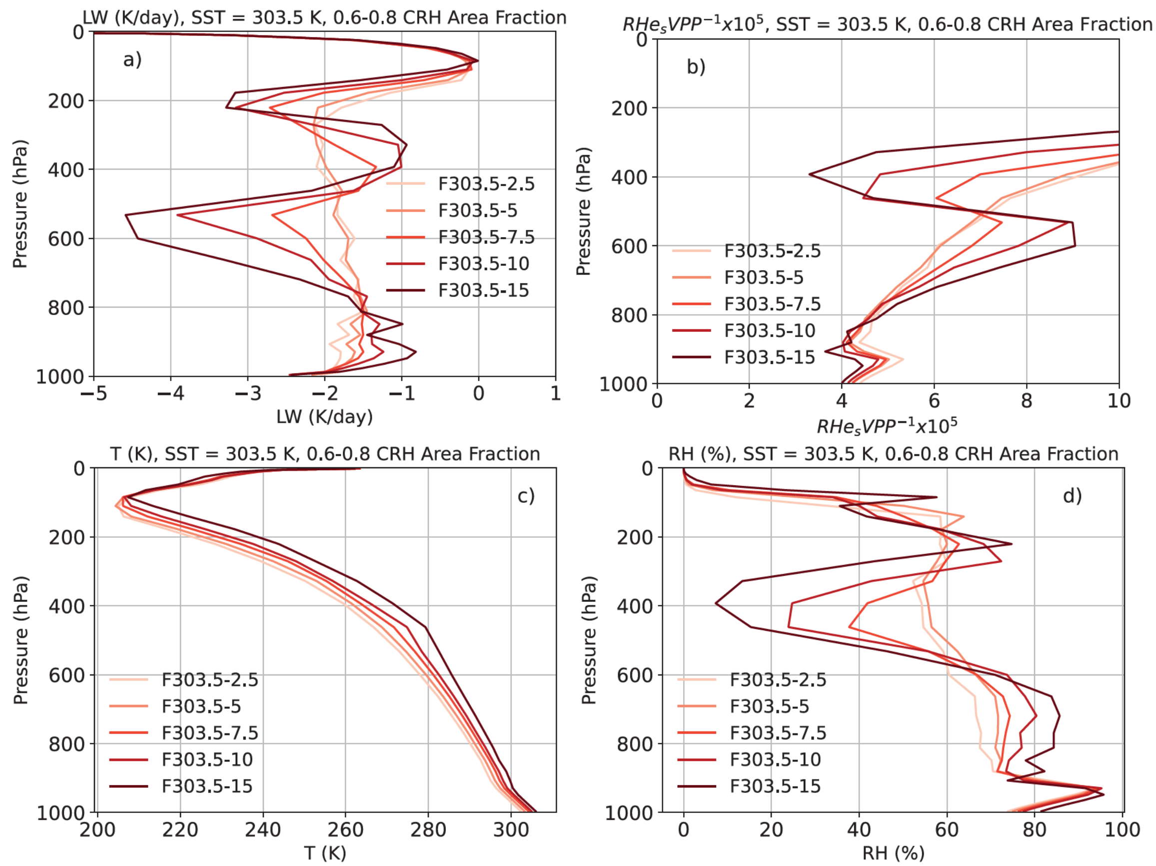

Figure 4.8: These panels show vertical profiles of quantities corresponding to experiments of each SST range with an SST of 303.5, averaged over 0.6-0.8 CRH area fraction. Panel (a) shows the temperature tendency from longwave cooling (K/day), (b) shows the humidity component of the longwave cooling approximation, $RHe_s(T)VPP^{-1}$, (c) temperature (K), and (d) relative humidity (%).

4.5 Shallow Convection

The longwave cooling of the moist layer provides a good consistency argument for the increasing shallow circulation with increasing SST gradient, but this longwave cooling does not work as well in understanding the increase in shallow circulation strength with increasing global mean SST. For a given SST range in Figure 4.7, as the global mean SST increases, the longwave cooling does not correspond as strongly with the increase in shallow circulation strength with mean SST. We also do not see the same expansion of peak longwave cooling into the intermediate region with increasing mean SST. We know from the streamfunctions shown in Figure 4.2 that the shallow cell strengthens and expands with increasing global mean SST. Because the longwave cooling does not strengthen and expand in this region with warming, an alternative explanation is required to explain the strengthening of the shallow cell with warming.

In this section we explore the role of shallow convection in driving stronger shallow circulations as the mean SST is increased. Figure 4.9 shows the total heating from parameterized convection in each case. For a given global mean SST, increasing the SST range does increase the strength of both deep and shallow convection, but the convection occupies a narrow region, and does not expand into intermediate regions. When increasing the global mean SST, the shallow convection both intensifies and expands, moistening the mid troposphere over intermediate regions of CRH and SST.

The increase in shallow convection over intermediate SSTs also corresponds to an increase in relative humidity in the layer. To better understand how the increase in shallow convection relates to humidity and sea surface temperature, we use a simplified model. W. Zhou and Xie (2019) use a spectral plume model (SPM) to illustrate the effect of entrainment on lapse rate. In this SPM, the strength of the entrainment is controlled by a parameter, ϵ, which we set to .3 km^{-1}, which both generates temperature profiles that best fit our model data and is also the value chosen by W. Zhou and Xie (2019) to best fit the observed tropical temperature profile. We use this model to generate parcel profiles for varying relative humidity profiles and sea surface temperatures. We then use these parcel profiles to calculate the convective available potential energy (CAPE), which we expect will

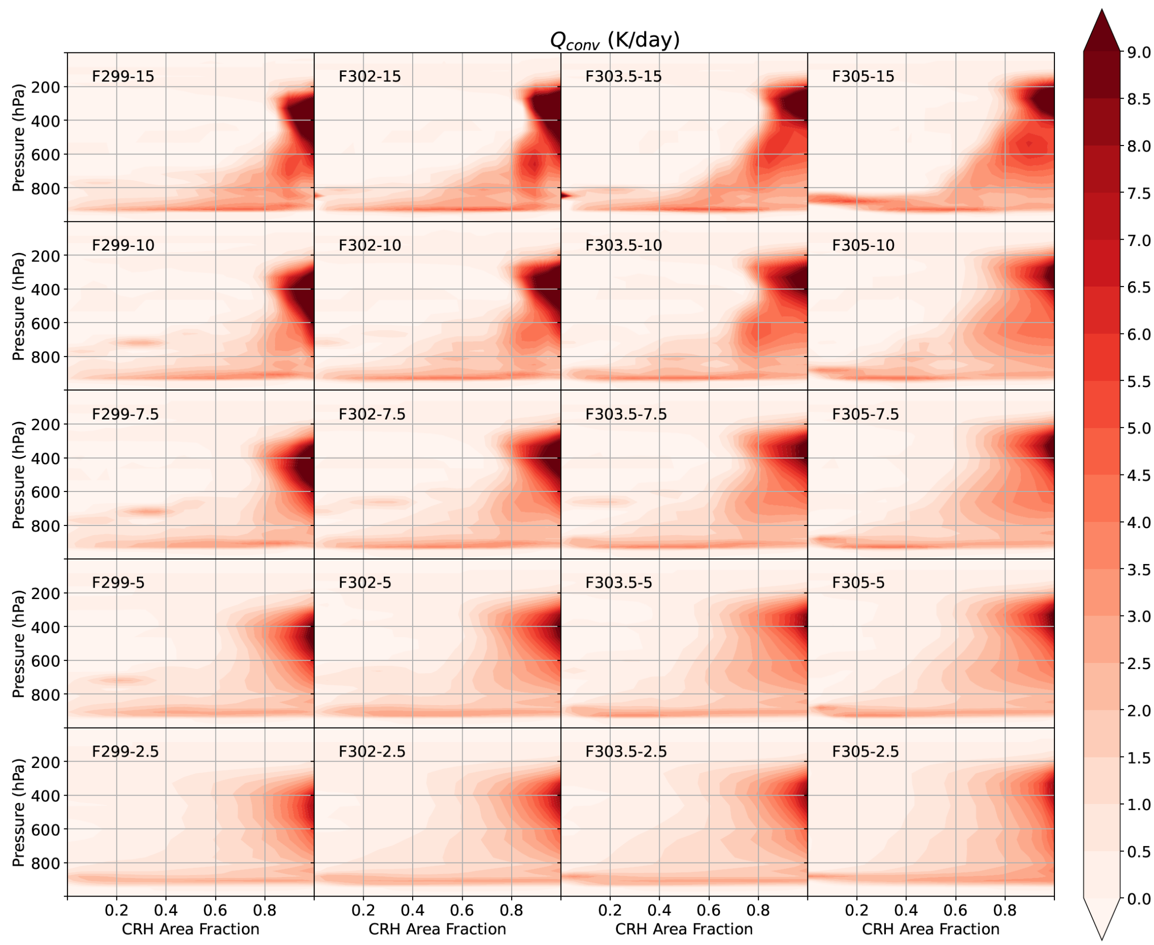

Figure 4.9: Heating from convection (K/day) for each case shown in pressure (hPa) and column relative humidity (CRH) area space (%). The global mean SST of each case increases from left to right, and the SST range increases from bottom to top.

explain the location of the shallow convection. Using this simplified model allows us to look at the impact of entrainment drying on convection height, and how this height is influenced by relative humidity.

The total CAPE is defined as

$$CAPE = \int \frac{T_{v,p} - T_{v,env}}{T_{v,env}} dz \tag{4.6}$$

where $T_{v,p}$ is the parcel virtual temperature (generated by the SPM) and $T_{v,env}$ is the background virtual temperature (from the GCM data). In model coordinates, this can be written as

$$CAPE = \sum_i \frac{T_{v,p,i} - T_{v,env,i}}{T_{v,env,i}} \Delta z_i = \sum_i B_i \Delta z_i \tag{4.7}$$

We call the $B_i \Delta z_i$ at each model level the contribution to CAPE by that layer, and look at how the vertical distribution of this quantity changes from case to case and is affected by the relative humidity distribution.

The top row of Figure 4.10 shows some test cases to illustrate the role of relative humidity on the vertical profile of CAPE contributions $B_i \Delta z_i$. Shown in green in Figure 4.10a is the relative humidity in the 0.6-0.8 CRH band for the case F303.5-7.5. In addition, we show test profiles that have a maximum RH of 20, 40 and 80% above the 849 hPa level. The CAPE contributions calculated with the SPM model for these examples are shown in Figure 4.10b. Decreasing the relative humidity above 849 hPa relative to the model profile produces a sharp increase of CAPE just above 849 hPa, but this increase is very shallow. This shallow CAPE increase is due to the effect of humidity on virtual temperature. The plume is assumed to be saturated, but the environment is assumed to have the prescribed RH profile. The dry RH profile decreases the virtual temperature of the environment, and so buoyancy of the saturated parcel increases. This spike in buoyancy is very shallow and above about 750 hPa the CAPE contribution for these dry cases is less than the control case represented by the model. Lifted parcels experience a larger lapse rate when lifted in the drier environment, quickly leading to a colder parcel temperature, and thus reducing the buoyancy of the parcel.

On the other hand, the SPM predicts a deeper layer of positive CAPE contribution for the moister 80% minimum RH case shown in Figure 4.10b. Parcels lifted into a moister environment maintain their buoyancy better and lead to increase CAPE contributions.

Figure 4.10 shows how the CAPE responds to warming in cases with a fixed SST contrast of 7.5 K. Panel c shows that the heating from convection in the 800 to 600 hPa layer increases as the temperature is increased from 299 K to 305 K, consistent with stronger driving of a shallow circulation by shallow convection as the temperature increases. Panel d shows that the plume model CAPE predicts this increase in shallow convection, since the layer of positive CAPE increases and deepens with increasing SST.

Although the magnitude of this effect is sensitive to the entrainment parameter used, the overall effect is consistent: drying limits the height convection reaches, and conversely, moistening can increase the height convection reaches. There is, however, a limit to how much increasing the relative humidity can increase the height of convection. As the temperature decreases at higher altitudes, the saturation specific humidity decreases, and its effect on the buoyancy and virtual temperature is reduced. Similarly, the effect of drying on the convection height is stronger at lower altitudes where the atmosphere is warmer and specific humidity has a larger impact on the buoyancy.

Janssens et al. (2024) find shallow convection to be the primary driver of shallow circulations, and also note that the SST range in the circulations considered is small. We similarly find shallow convection to play a significant role when warming the global mean SST, and that increasing the SST range can actually limit the impact of shallow convection through the drying of the mid troposphere above the moist layer. Dry mid tropospheres strengthen longwave cooling, while moister mid tropospheres favor shallow convection. Shallow convection also brings moisture up from the surface and increases the humidity, making the environment more favorable for future shallow convection.

In these experiments, increasing the global mean SST increases shallow CAPE in the intermediate region between subsidence and deep convection, and this leads to an increase in shallow convection. The moistening and extension of the lower tropospheric moist layer with a warming climate can be clearly seen in the relative humidity sections in Figure 4.5. A feedback process between shallow convection and relative humidity works as follows:

1. Shallow convection strengthens and enhances the secondary moist layer.

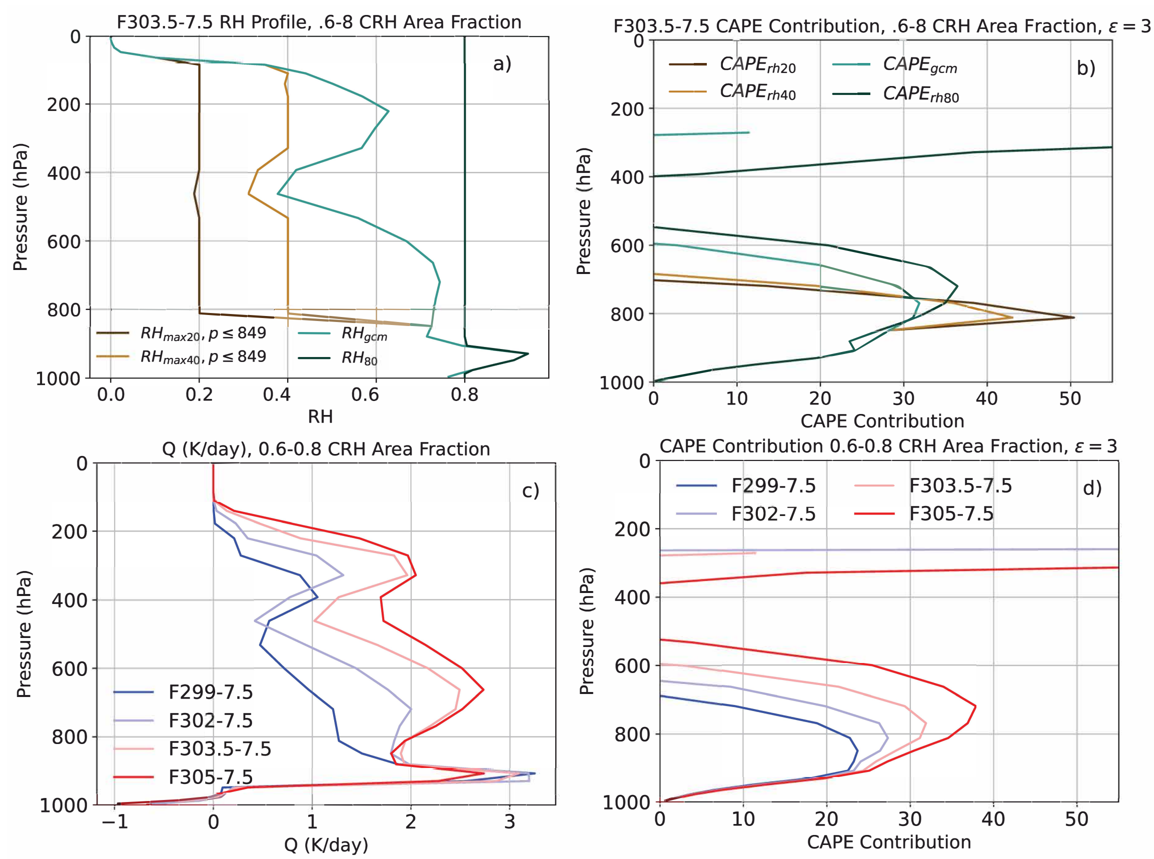

Figure 4.10: The top row shows the CAPE dependence on relative humidity. Panel a shows the relative humidity profiles used to generate parcel profiles in the SPM, (b) the CAPE contribution for each relative humidity profile. The bottom row shows the CAPE dependence on mean SST. Panel c shows the heating from convection (K/day), panel d shows the CAPE contribution for cases with a range of 7.5 K.

2. A moist lower free troposphere favors shallow convection.

This process becomes stronger with warming as shallow CAPE increases with a warming climate.

4.6 Summary

Tropical shallow circulations play an important role both in observations and in idealized modeling experiments. Potential drivers for shallow circulation strength include boundary layer pressure gradients driven by sea surface temperature distributions, boundary layer longwave cooling, and shallow convection. Here, we use an idealized model to look at the relationship between the sea surface temperature gradient, mean sea surface temperature magnitude, and the shallow circulation strength.

We find that different drivers dominate depending on whether we increase the SST range or increase the global mean SST. In both cases, this strengthening of the shallow cell corresponds to anomalous heating rates above the boundary layer. When increasing the SST range, the longwave cooling above the boundary layer in the dry, subsiding region increases as the shallow circulation strengthens. When increasing the global mean SST, the shallow convection over intermediate CRH/SSTs increases, but there is not a strong increase in the longwave cooling above the boundary layer. In summary, increasing the SST range strengthens the shallow circulation by increasing the longwave cooling rate, while increasing the global mean SST strengthens the shallow circulation by increasing the shallow convection over intermediate SSTs.

- When increasing the SST range, the boundary layer longwave cooling increases as both the deep and shallow circulations strengthen and the subsiding region dries.

- When increasing the global mean SST, heating from shallow convection dominates. An increase in CAPE over the intermediate region between deep convection and subsidence leads to an increase in shallow convection, moistening the mid troposphere and making the environment more favorable for further convection.

- The conditions favorable for each mechanism work in opposition to each other. Drying above the boundary layer leads to an increase in longwave cooling, but is less favorable for shallow convection due to effects from entrainment drying. Conversely, moistening above the boundary layer is more favorable for shallow convection, but limits the longwave cooling.

These idealized experiments present a simplified, qualitative relationship between these mechanisms and are thus limited in their application to a more realistic setting. For example, the relative humidity in the subsiding region is often much drier than would be expected from observations. This may over-emphasize the significance of entrainment drying on convection. In scenarios with moister subsiding regions, convergence forced shallow convection could play a larger role when increasing the SST gradient, as in Back and Bretherton (2009). Similarly, we use the quantity CAPE in an attempt to connect our results to a quantity applicable to observations, but in our model convection is parameterized. Despite these limitations, these results provide a useful framework for the indirect effect of SST on shallow circulation.

Chapter 5

SUMMARY

In the preceding chapters, we explored the interaction between sea surface temperature and convection in radiative convective equilibrium with incrementally increasing complexity. We start from an aqua-planet with no rotation, uniform insolation, and a slab ocean with interactive sea surface temperature; in subsequent chapters, we modify elements of this base framework to better address ocean heat transport effects and shallow circulation drivers. The atmospheric circulation response to sea surface temperature consistently plays a major role, particularly through the consequent atmospheric energy transport.

In the first chapter, we use the inter-annual oscillations of the climate to identify mechanisms constraining the sea surface temperature distribution. We found that the atmospheric energy transport responds to the skewness of the SST distribution, and this transport cools the warmest SSTs and reduces the SST contrast. At the surface level, this corresponds to an increase in evaporative cooling. The circulation similarly influences low clouds, particularly through its impact on the humidity above the boundary layer.

The circulation response plays a similar role when considering the role of ocean heat transport. When we add a Gaussian shaped, net-zero surface heating (Q-flux), the warmest SSTs align over the positive Q-flux and the coldest SSTs over the negative Q-flux. Despite the Q-flux heating under the warmest SSTs, the maximum SST does not increase between cases with and without Q-flux. This is because the increased atmospheric energy transport out of the ascending region over the warmest SSTs increases and offsets the Q-flux heating. The role of clouds in these experiments varies with the mean sea surface temperature of the experiment: when warming from the coldest experiments, there is a drastic decrease in low clouds and an increase in the greenhouse effect gradient between subsiding and ascending regions.

Because atmospheric energy transport plays a large role in both preceding chapters, in the fourth chapter, we investigate the influence of sea surface temperature on the vertical structure and strength of the atmospheric circulation. Instead of looking at the direct effect of sea surface temperature and gradients on the boundary layer pressure gradients, we look at the indirect effects on shallow convection and longwave cooling. In this chapter, we find that the shallow circulation strength increases with both mean SST and SST range, but the primary mechanism strengthening the shallow circulation differs when warming the mean sea surface temperature versus increasing the sea surface temperature gradient. When warming the global mean SST, the shallow circulation is strengthened by shallow convection over intermediate SSTs. This is associated with an increase in CAPE as the surface MSE gradient increases. When increasing the SST range, the shallow circulation is strengthened by boundary layer longwave cooling in the subsiding region. This is associated with a strong drying of the mid troposphere as the deep circulation strength increases due to large SST gradient-driven surface pressure gradients.

In each chapter, atmospheric circulation and energy transport are fundamental to the relationship between sea surface temperature and convection,

- Atmospheric energy transport responds to the skewness of SST and works to reduce the SST gradient

- Increasing the SST gradient in OHT experiments leads to an increase in atmospheric energy transport that keeps the warmest SSTs cool

- The double cell structure of the atmospheric circulation responds to both warming the global mean SST and to increasing the SST range

In these chapters, we use idealized modeling experiments to characterize the mechanisms governing the relationship between sea surface temperature and convection. We use reanalysis data to verify that our model results are within reasonable comparison to reality. Future work is required to determine the impact of these described mechanisms in the observed tropics with its entire complexity. Outside of moving to observational work to better understand the real world impact of these interactions, more could be learned within an idealized modeling framework. Regarding the effect of ocean heat transport, one limitation is that the Q-flux does not respond, in turn, to the atmosphere. An interactive Q-flux, as opposed to the constant Q-flux used in our experiments, could be used to represent the atmosphere's influence on ocean heat transport without moving to a fully coupled ocean. For better understanding the impact of sea surface temperature on shallow circulations, mechanism denial experiments could be conducted to evaluate the contribution of shallow convection and longwave cooling. Additionally, because relative humidity plays a critical role in both mechanisms, experiments in which relative humidity is specified when computing longwave cooling and convection within the model could quantify the impact of relative humidity changes.

References

Anderson, J. L., Balaji, V., Broccoli, A. J., Cooke, W. F., Delworth, T. L., Dixon, K. W., ... Dev, G. G. A. M. (2004). The new gfdl global atmosphere and land model am2-lm2: Evaluation with prescribed sst simulations [Journal Article]. *J. Climate*, *17*(24), 4641-4673.

Andrews, T., Gregory, J. M., Paynter, D., Silvers, L. G., Zhou, C., Mauritsen, T., ... Titchner, H. (2018a). Accounting for changing temperature patterns increases historical estimates of climate sensitivity [Journal Article]. *Geophys. Res. Lett.*, *45*(16), 8490-8499. Retrieved from `https://agupubs.onlinelibrary.wiley.com/doi/abs/10.1029/2018GL078887` doi: 10.1029/2018gl078887

Andrews, T., Gregory, J. M., Paynter, D., Silvers, L. G., Zhou, C., Mauritsen, T., ... Titchner, H. (2018b). Accounting for Changing Temperature Patterns Increases Historical Estimates of Climate Sensitivity. *Geophysical Research Letters*, *45*(16), 8490–8499. Retrieved 2023-10-09, from `https://onlinelibrary.wiley.com/doi/abs/10.1029/2018GL078887` doi: 10.1029/2018GL078887

Armour, K. C. (2017, May). Energy budget constraints on climate sensitivity in light of inconstant climate feedbacks. *Nature Climate Change*, *7*(5), 331–335. Retrieved 2023-

10-09, from https://www.nature.com/articles/nclimate3278 doi: 10.1038/nclimate3278

Armour, K. C., Proistosescu, C., Dong, Y., Hahn, L. C., Blanchard-Wrigglesworth, E., Pauling, A. G., ... Gregory, J. M. (2024a). Sea-surface temperature pattern effects have slowed global warming and biased warming-based constraints on climate sensitivity [Journal Article]. *Proceedings of the National Academy of Sciences*, *121*(12), e2312093121. Retrieved from https://www.pnas.org/doi/abs/10.1073/pnas.2312093121 doi: doi:10.1073/pnas.2312093121

Armour, K. C., Proistosescu, C., Dong, Y., Hahn, L. C., Blanchard-Wrigglesworth, E., Pauling, A. G., ... Gregory, J. M. (2024b). Sea-surface temperature pattern effects have slowed global warming and biased warming-based constraints on climate sensitivity [Journal Article]. *Proceedings of the National Academy of Sciences*, *121*(12), e2312093121. doi: doi:10.1073/pnas.2312093121

Back, L. E., & Bretherton, C. S. (2009, August). On the Relationship between SST Gradients, Boundary Layer Winds, and Convergence over the Tropical Oceans. *Journal of Climate*, *22*(15), 4182–4196. Retrieved 2024-04-30, from https://journals.ametsoc.org/view/journals/clim/22/15/2009jcli2392.1.xml doi: 10.1175/2009JCLI2392.1

Bjerknes, J. (1966). A possible response of the atmospheric hadley circulation to equatorial anomalies of ocean temperature [Journal Article]. *Tellus*, *18A*, 820-829.

Bony, S., Stevens, B., Coppin, D., Becker, T., Reed, K. A., Voigt, A., & Medeiros, B. (2016, August). Thermodynamic control of anvil cloud amount. *Proceedings of the National Academy of Sciences*, *113*(32), 8927–8932. Retrieved 2020-04-02, from http://www.pnas.org/lookup/doi/10.1073/pnas.1601472113 doi: 10.1073/pnas.1601472113

Bony, S., Stevens, B., Frierson, D. M. W., Jakob, C., Kageyama, M., Pincus, R., ... Webb, M. J. (2015). Clouds, circulation and climate sensitivity [Journal Article]. *Nature Geoscience*, *8*(4), 261-268. doi: 10.1038/ngeo2398

Bretherton, C. S., & Blossey, P. N. (2014). Low cloud reduction in a greenhouse-warmed climate: Results from Lagrangian LES of a subtropical marine cloudiness transition. *Journal of Advances in Modeling Earth Systems*, *6*(1), 91–114. Retrieved 2020-04-02, from https://agupubs.onlinelibrary.wiley.com/doi/abs/10.1002/2013MS000250 doi: 10.1002/2013MS000250

Bretherton, C. S., Blossey, P. N., & Khairoutdinov, M. (2005, December). An Energy-Balance Analysis of Deep Convective Self-Aggregation above Uniform SST. *Journal of the Atmospheric Sciences*, *62*(12), 4273–4292. Retrieved 2020-02-19, from https://journals.ametsoc.org/doi/10.1175/JAS3614.1 doi: 10.1175/JAS3614.1

Bretherton, C. S., & Khairoutdinov, M. F. (2015). Convective self-aggregation feedbacks in near-global cloud-resolving simulations of an aquaplanet. *Journal of Advances in Modeling Earth Systems*, *7*(4), 1765–1787. Retrieved 2021-03-08, from https://agupubs.onlinelibrary.wiley.com/doi/abs/10.1002/2015MS000499 doi: https://doi.org/10.1002/2015MS000499

Cheng, L., Trenberth, K. E., Fasullo, J. T., Mayer, M., Balmaseda, M., & Zhu, J. (2019). Evolution of ocean heat content related to enso [Journal Article]. *Journal of Climate*, *32*(12), 3529-3556. Retrieved from https://journals.ametsoc.org/view/journals/clim/32/12/jcli-d-18-0607.1.xml doi: https://doi.org/10.1175/JCLI-D-18-0607.1

Coppin, D., & Bony, S. (2015). Physical mechanisms controlling the initiation of convective self-aggregation in a General Circulation Model. *Journal of Advances in Modeling Earth Systems*, *7*(4), 2060–2078. Retrieved 2020-01-30, from https://agupubs.onlinelibrary.wiley.com/doi/abs/10.1002/2015MS000571 doi: 10.1002/2015MS000571

Coppin, D., & Bony, S. (2017). Internal variability in a coupled general circulation model in radiative-convective equilibrium. *Geophysical Research Letters*, *44*(10), 5142–5149. Retrieved 2020-02-21, from https://agupubs.onlinelibrary.wiley.com/doi/abs/10.1002/2017GL073658 doi: 10.1002/2017GL073658

Coppin, D., & Bony, S. (2018). On the Interplay Between Convective Aggregation, Surface Temperature Gradients, and Climate Sensitivity. *Journal of Advances in Modeling Earth Systems*, *10*(12), 3123–3138. Retrieved 2020-01-30, from `https://agupubs.onlinelibrary.wiley.com/doi/abs/10.1029/2018MS001406` doi: 10.1029/2018MS001406

Cronin, T. W., & Wing, A. A. (2017). Clouds, Circulation, and Climate Sensitivity in a Radiative-Convective Equilibrium Channel Model. *Journal of Advances in Modeling Earth Systems*, *9*(8), 2883–2905. Retrieved 2020-04-02, from `https://agupubs.onlinelibrary.wiley.com/doi/abs/10.1002/2017MS001111` doi: 10.1002/2017MS001111

Delworth, T. L., Broccoli, A. J., Rosati, A., Stouffer, R. J., Balaji, V., Beesley, J. A., ... Zhang, R. (2006). Gfdl's cm2 global coupled climate models. part i: Formulation and simulation characteristics [Journal Article]. *J. Climate*, *19*(5), 643-674. Retrieved from `<Go to ISI>://WOS:000236668000002` doi: 10.1175/jcli3629.1

Dong, Y., Armour, K. C., Zelinka, M. D., Proistosescu, C., Battisti, D. S., Zhou, C., & Andrews, T. (2020, September). Intermodel Spread in the Pattern Effect and Its Contribution to Climate Sensitivity in CMIP5 and CMIP6 Models. *Journal of Climate*, *33*(18), 7755–7775. Retrieved 2023-10-09, from `https://journals.ametsoc.org/view/journals/clim/33/18/jcliD191011.xml` doi: 10.1175/JCLI-D-19-1011.1

Dong, Y., Proistosescu, C., Armour, K. C., & Battisti, D. S. (2019, June). Attributing Historical and Future Evolution of Radiative Feedbacks to Regional Warming Patterns using a Green's Function Approach: The Preeminence of the Western Pacific. *Journal of Climate*, *32*(17), 5471–5491. Retrieved 2020-02-21, from `https://journals.ametsoc.org/doi/full/10.1175/JCLI-D-18-0843.1` doi: 10.1175/JCLI-D-18-0843.1

Drotos, G., Becker, T., Mauritsen, T., & Stevens, B. (2020). Global variability in radiative-convective equilibrium with a slab ocean under a wide range of co2 concentrations [Journal Article]. *Tellus A*, *72*(1), 1-19. doi: 10.1080/16000870.2019.1699387

Dygert, B. D., & Hartmann, D. L. (2023). The Cycle of Large-Scale Aggregation in Tropical Radiative-Convective Equilibrium. *Journal of Geophysical Research: Atmospheres*, *128*(7), e2022JD037302. Retrieved 2023-06-27, from https://onlinelibrary.wiley.com/doi/abs/10.1029/2022JD037302 doi: 10.1029/2022JD037302

Eastman, R., & Wood, R. (2018, August). The Competing Effects of Stability and Humidity on Subtropical Stratocumulus Entrainment and Cloud Evolution from a Lagrangian Perspective. *Journal of the Atmospheric Sciences*, *75*(8), 2563–2578. Retrieved 2024-03-07, from https://journals.ametsoc.org/view/journals/atsc/75/8/jas-d-18-0030.1.xml (Publisher: American Meteorological Society Section: Journal of the Atmospheric Sciences) doi: 10.1175/JAS-D-18-0030.1

Emanuel, K., Wing, A. A., & Vincent, E. M. (2014). Radiative-convective instability [Journal Article]. *J. Adv. Mod. Earth Sys.*, *6*(1), 75-90. doi: 10.1002/2013ms000270

Fildier, B., Muller, C., Pincus, R., & Fueglistaler, S. (2023). How Moisture Shapes Low-Level Radiative Cooling in Subsidence Regimes. *AGU Advances*, *4*(3), e2023AV000880. Retrieved 2024-11-03, from https://onlinelibrary.wiley.com/doi/abs/10.1029/2023AV000880 doi: 10.1029/2023AV000880

Fläschner, D., Mauritsen, T., Stevens, B., & Bony, S. (2018). The signature of shallow circulations, not cloud radiative effects, in the spatial distribution of tropical precipitation [Journal Article]. *Journal of Climate*, *31*(23), 9489-9505. doi: https://doi.org/10.1175/JCLI-D-18-0230.1

Gasparini, B., Blossey, P. N., Hartmann, D. L., Lin, G. X., & Fan, J. W. (2019). What drives the life cycle of tropical anvil clouds? [Journal Article]. *Journal of Advances in Modeling Earth Systems*, *11*(8), 2586-2605. doi: 10.1029/2019ms001736

Grabowski, W. W., Jun, I. Y., & Moncrieff, M. W. (2000). Cloud resolving modeling of tropical circulations driven by large-scale sst gradients [Journal Article]. *J. Atmos. Sci.*, *57*(13), 2022-39. (Using Smart Source Parsing 1 July p)

Harrison, E. F., Minnis, P., Barkstrom, B. R., Ramanathan, V., Cess, R. D., & Gibson, G. G. (1990). Seasonal variation of cloud radiative forcing derived from the earth radiation budget experiment [Journal Article]. *J. Geophys. Res.*, *95*, 18,687-18,703.

Hartmann, D. L. (2016). Global physical climatology. In (2nd ed., p. 40). Elsevier.

Hartmann, D. L., & Dygert, B. D. (2022a). Global Radiative Convective Equilibrium With a Slab Ocean: SST Contrast, Sensitivity and Circulation. *Journal of Geophysical Research: Atmospheres*, *127*(12), e2021JD036400. Retrieved 2023-10-10, from `https://onlinelibrary.wiley.com/doi/abs/10.1029/2021JD036400` (_eprint: https://onlinelibrary.wiley.com/doi/pdf/10.1029/2021JD036400) doi: 10.1029/2021JD036400

Hartmann, D. L., & Dygert, B. D. (2022b). Global radiative convective equilibrium with a slab ocean: Sst contrast, sensitivity and circulation. *Journal of Geophysical Research: Atmospheres*. doi: 10.1029/2021JD036400

Hartmann, D. L., Dygert, B. D., Blossey, P. N., Fu, Q., & Sokol, A. B. (2022a, September). The Vertical Profile of Radiative Cooling and Lapse Rate in a Warming Climate. *Journal of Climate*, *35*(19), 6253–6265. Retrieved 2023-10-24, from `https://journals.ametsoc.org/view/journals/clim/35/19/JCLI-D-21-0861.1.xml` (Publisher: American Meteorological Society Section: Journal of Climate) doi: 10.1175/JCLI-D-21-0861.1

Hartmann, D. L., Dygert, B. D., Blossey, P. N., Fu, Q., & Sokol, A. B. (2022b). The vertical profile of radiative cooling in radiative-convective equilibrium: Moist adiabat versus entrainment-modified plume model. *J. Climate*. doi: 10.1175/JCLI-D-21-0861.1

Hartmann, D. L., Gasparini, B., Berry, S. E., & Blossey, P. N. (2018). The life cycle and net radiative effect of tropical anvil clouds [Journal Article]. *Journal of Advances in Modeling Earth Systems*, *10*(12), 3012-3029. doi: 10.1029/2018ms001484

Held, I. M., Hemler, R. S., & Ramaswamy, V. (1993). Radiative-convective equilibrium with explicit two-dimensional moist convection [Journal Article]. *J. Atmos. Sci.*, *50*(23), 3909-3927. (Geophys. Fluid Dynamics Lab., NOAA, Princeton Univ., NJ, USA.)

Held, I. M., Zhao, M., & Wyman, B. (2007, January). Dynamic Radiative–Convective Equilibria Using GCM Column Physics. *Journal of the Atmospheric Sciences*, *64*(1), 228–238. Retrieved 2020-02-05, from `https://journals.ametsoc.org/doi/full/10.1175/JAS3825.11` doi:

10.1175/JAS3825.11

Hersbach, H., Bell, B., Berrisford, P., Hirahara, S., Horányi, A., Muñoz-Sabater, J., ... Thépaut, J.-N. (2020a). The era5 global reanalysis [Journal Article]. *Quarterly Journal of the Royal Meteorological Society*, *146*(730), 1999-2049. doi: https://doi.org/10.1002/qj.3803

Hersbach, H., Bell, B., Berrisford, P., Hirahara, S., Horányi, A., Muñoz-Sabater, J., ... Thépaut, J.-N. (2020b). The era5 global reanalysis [Journal Article]. *Quarterly Journal of the Royal Meteorological Society*, *146*(730), 1999-2049. doi: https://doi.org/10.1002/qj.3803

Horel, J. D., & Wallace, J. M. (1981). Planetary-scale atmospheric phenomena associated with the southern oscillation [Journal Article]. *Mon. Wea. Rev.*, *109*, 813-829. doi: https://doi.org/10.1175/1520-0493(1981)109¡0813:PSAPAW¿2.0.CO;2

Huaman, L., Schumacher, C., & Sobel, A. H. (2022). Assessing the Vertical Velocity of the East Pacific ITCZ. *Geophysical Research Letters*, *49*(1), e2021GL096192. Retrieved 2024-02-06, from `https://onlinelibrary.wiley.com/doi/abs/10.1029/2021GL096192` doi: 10.1029/2021GL096192

Huang, J.-D., & Wu, C.-M. (2022). A Framework to Evaluate Convective Aggregation: Examples With Different Microphysics Schemes. *Journal of Geophysical Research: Atmospheres*, *127*(5), e2021JD035886. Retrieved 2022-09-13, from `https://onlinelibrary.wiley.com/doi/abs/10.1029/2021JD035886` doi: 10.1029/2021JD035886

Janssens, M., George, G., Schulz, H., Couvreux, F., & Bouniol, D. (2024). Shallow Convective Heating in Weak Temperature Gradient Balance Explains Mesoscale Vertical Motions in the Trades. *Journal of Geophysical Research: Atmospheres*, *129*(18), e2024JD041417. Retrieved 2024-12-12, from `https://onlinelibrary.wiley.com/doi/abs/10.1029/2024JD041417` doi: 10.1029/2024JD041417

Jeevanjee, N., & Fueglistaler, S. (2020, February). On the Cooling-to-Space Approximation. *Journal of the Atmospheric Sciences*, *77*(2), 465–478. Retrieved 2020-

04-02, from `http://journals.ametsoc.org/doi/10.1175/JAS-D-18-0352.1` doi: 10.1175/JAS-D-18-0352.1

Klein, S., & Hartmann, D. (1993). The seasonal cycle of low stratiform clouds [Journal Article]. *J. Climate*, *6*(8), 1587-1606.

Knutson, T. R., & Manabe, S. (1995). Time-mean response over the tropical pacific to increased co2 in a coupled ocean-atmosphere model [Journal Article]. *J. Climate*, *8*(9), 2181-2199. Retrieved from `<Go to ISI>://A1995RT01100004`

Larson, K., & Hartmann, D. L. (2003). Interactions among cloud, water vapor, radiation, and large-scale circulation in the tropical climate. part ii: Sensitivity to spatial gradients of sea surface temperature [Journal Article]. *J. Climate*, *16*(10), 1441-1455. (Using Smart Source Parsing 15 0894-8755 Physical-Chemical-and-Earth-Sciences)

Larson, K., Hartmann, D. L., & Klein, S. A. (1999). The role of clouds, water vapor, circulation, and boundary layer structure in the sensitivity of the tropical climate [Journal Article]. *J. Climate*, *12*(8), 2359-2374. (Using Smart Source Parsing pt.1; Aug. p)

Lindzen, R. S., & Nigam, S. (1987, September). On the Role of Sea Surface Temperature Gradients in Forcing Low-Level Winds and Convergence in the Tropics. Retrieved 2025-03-11, from `https://journals.ametsoc.org/view/journals/atsc/44/17/1520-0469`$_1987_044_2418_otross_{20c}o_2.$

Lutsko, N. J., & Cronin, T. W. (2018). Increase in precipitation efficiency with surface warming in radiative-convective equilibrium [Journal Article]. *Journal of Advances in Modeling Earth Systems*, *10*(11), 2992-3010. doi: 10.1029/2018ms001482

Lutsko, N. J., & Cronin, T. W. (2024a). The Transition to Double-Celled Circulations in Mock-Walker Simulations. *Geophysical Research Letters*, *51*(14), e2024GL108945. Retrieved 2025-04-22, from `https://onlinelibrary.wiley.com/doi/abs/10.1029/2024GL108945` doi: 10.1029/2024GL108945

Lutsko, N. J., & Cronin, T. W. (2024b). The transition to double-celled circulations in mock-walker simulations [Journal Article]. *Geophysical Research Letters*, *51*(14), e2024GL108945. doi: https://doi.org/10.1029/2024GL108945

Manabe, S., & Wetherald, R. T. (1967, May). Thermal Equilibrium of the Atmosphere with a Given Distribution of Relative Humidity. *Journal of the Atmospheric Sciences*, *24*(3), 241–259. Retrieved 2020-04-02, from

Mayer, J., Mayer, M., & Haimberger, L. (2021). *Mass-consistent atmospheric energy and moisture budget monthly data from 1979 to present derived from era5 reanalysis* [dataset]. doi: 10.24381/cds.c2451f6b

Meraner, K., Mauritsen, T., & Voigt, A. (2013). Robust increase in equilibrium climate sensitivity under global warming. *Geophysical Research Letters*, *40*(22), 5944–5948. Retrieved 2024-04-10, from `https://onlinelibrary.wiley.com/doi/abs/10.1002/2013GL058118` doi: 10.1002/2013GL058118

Miller, R. (1997). Tropical thermostats and low cloud cover [Journal Article]. *J. Climate*, *10*(3), 409-440.

Naumann, A. K., Stevens, B., Hohenegger, C., & Mellado, J. P. (2017, October). A Conceptual Model of a Shallow Circulation Induced by Prescribed Low-Level Radiative Cooling. *Journal of the Atmospheric Sciences*, *74*(10), 3129–3144. Retrieved 2024-02-20, from `https://journals.ametsoc.org/view/journals/atsc/74/10/jas-d-17-0030.1.xml` doi: 10.1175/JAS-D-17-0030.1

Neelin, J. D., & Held, I. M. (1987). Modeling tropical convergence based on the moist static energy budget [Journal Article]. *Mon. Wea. Rev.*, *115*(1), 3-12. Retrieved from `https://doi.org/10.1175/1520-0493(1987)115<0003:MTCBOT>2.0.CO;2` doi: 10.1175/1520-0493(1987)115¡0003:Mtcbot¿2.0.Co;2

Nishant, N., Sherwood, S. C., & Geoffroy, O. (2016). Radiative driving of shallow return flows from the ITCZ. *Journal of Advances in Modeling Earth Systems*, *8*(2), 831–842. Retrieved 2022-10-25, from `https://onlinelibrary.wiley.com/doi/abs/10.1002/2015MS000606` (_eprint: https://onlinelibrary.wiley.com/doi/pdf/10.1002/2015MS000606) doi: 10.1002/2015MS000606

Nolan, D. S., Zhang, C., & Chen, S.-h. (2007, July). Dynamics of the Shallow Meridional Circulation around Intertropical Convergence Zones. *Journal of the Atmospheric Sciences*, *64*(7), 2262–2285. Retrieved 2022-10-28, from `https://journals.ametsoc.org/view/journals/atsc/64/7/jas3964.1.xml` (Publisher: American Meteorological Society Section: Journal of the Atmospheric Sciences) doi: 10.1175/JAS3964.1

Nuijens, L., & Emanuel, K. (2018). Congestus modes in circulating equilibria of the tropical atmosphere in a two-column model. *Quarterly Journal of the Royal Meteorological Society*, *144*(717), 2676–2692. Retrieved 2022-05-25, from `https://onlinelibrary.wiley.com/doi/abs/10.1002/qj.3385` doi: 10.1002/qj.3385

Pierrehumbert, R. T. (1995, May). Thermostats, Radiator Fins, and the Local Runaway Greenhouse. *Journal of the Atmospheric Sciences*, *52*(10), 1784–1806. Retrieved 2020-02-05, from

Popke, D., Stevens, B., & Voigt, A. (2013, March). Climate and climate change in a radiative-convective equilibrium version of ECHAM6. *Journal of Advances in Modeling Earth Systems*, *5*(1), 1–14. Retrieved 2020-02-21, from `https://agupubs.onlinelibrary.wiley.com/doi/full/10.1029/2012MS000191` doi: 10.1029/2012MS000191

Raymond, D. J., Sessions, S. L., Sobel, A. H., & Fuchs, Z. (2009). The mechanics of gross moist stability [Journal Article]. *J. Adv. Model. Earth Sys.*, *1*. Retrieved from `<Go to ISI>://WOS:000208299400009` doi: 10.3894/james.2009.1.9

Reed, K. A., & Chavas, D. R. (2015). Uniformly rotating global radiative-convective equilibrium in the Community Atmosphere Model, version 5. *Journal of Advances in Modeling Earth Systems*, *7*(4), 1938–1955. Retrieved 2020-05-15, from `https://agupubs.onlinelibrary.wiley.com/doi/abs/10.1002/2015MS000519` doi: 10.1002/2015MS000519

Reed, K. A., Medeiros, B., Bacmeister, J. T., & Lauritzen, P. H. (2015). Global radiative-convective equilibrium in the community atmosphere model, version 5 [Journal Article]. *J. Atmos. Sci.*, *72*(5), 2183-2197. doi: 10.1175/jas-d-14-0268.1

Retsch, M. H., Mauritsen, T., & Hohenegger, C. (2019). Climate Change Feedbacks in Aquaplanet Experiments With Explicit and Parametrized Convection for Horizontal Resolutions of 2,525 Up to 5 km. *Journal of Advances in Modeling Earth Systems*, *11*(7), 2070–2088. Retrieved 2020-01-24, from `https://agupubs.onlinelibrary.wiley.com/doi/abs/10.1029/2019MS001677` doi: 10.1029/2019MS001677

Russell, G. L., Lacis, A. A., Rind, D. H., Colose, C., & Opstbaum, R. F. (2013). Fast atmosphere-ocean model runs with large changes in CO2. *Geophysical Research Letters*, *40*(21), 5787–5792. Retrieved 2024-04-10, from `https://onlinelibrary.wiley.com/doi/abs/10.1002/2013GL056755` doi: 10.1002/2013GL056755

Schneider, T., Kaul, C. M., & Pressel, K. G. (2019, March). Possible climate transitions from breakup of stratocumulus decks under greenhouse warming. *Nature Geoscience*, *12*(3), 163–167. Retrieved 2024-03-07, from `https://www.nature.com/articles/s41561-019-0310-1` doi: 10.1038/s41561-019-0310-1

Schulz, H., & Stevens, B. (n.d.). *Observing the Tropical Atmosphere in Moisture Space in: Journal of the Atmospheric Sciences Volume 75 Issue 10 (2018).* Retrieved 2022-10-26, from `https://journals.ametsoc.org/view/journals/atsc/75/10/jas-d-17-0375.1.xml`

Sobel, A. H., & Neelin, J. D. (2006, November). The boundary layer contribution to intertropical convergence zones in the quasi-equilibrium tropical circulation model framework. *Theoretical and Computational Fluid Dynamics*, *20*(5), 323–350. Retrieved 2025-03-11, from `https://doi.org/10.1007/s00162-006-0033-y` doi: 10.1007/s00162-006-0033-y

Sobel, A. H., Nilsson, J., & Polvani, L. M. (2001, December). The Weak Temperature Gradient Approximation and Balanced Tropical Moisture Waves. Retrieved 2025-02-18, from `https://journals.ametsoc.org/view/journals/atsc/58/23/1520-0469`$_2001_058_3650_twtgaa_2.0.co_2.xml$

Stevens, B., Sherwood, S. C., Bony, S., & Webb, M. J. (2016). Prospects for narrowing bounds on Earth's equilibrium climate sensitivity. *Earth's Future*, *4*(11), 512–522. Retrieved 2023-10-09, from `https://onlinelibrary.wiley.com/doi/abs/10.1002/2016EF000376` doi: 10.1002/2016EF000376

Tompkins, A. M. (2001, July). Organization of Tropical Convection in Low Vertical Wind Shears: The Role of Cold Pools. *Journal of the Atmospheric Sciences*, *58*(13), 1650–1672. Retrieved 2020-04-02, from

Tompkins, A. M., & Craig, G. C. (1998). Radiative-convective equilibrium in a three-dimensional cloud-ensemble model [Journal Article]. *Quart. J. Roy. Meteor. Soc.*, *124*(550), 2073-97.

Tompkins, A. M., & Semie, A. G. (2021). Impact of a Mixed Ocean Layer and the Diurnal Cycle on Convective Aggregation. *Journal of Advances in Modeling Earth Systems*, *13*(12), e2020MS002186. Retrieved 2022-09-13, from `https://onlinelibrary.wiley.com/doi/abs/10.1029/2020MS002186` doi: 10.1029/2020MS002186

Vecchi, G. A., & Soden, B. J. (2007). Global warming and the weakening of the tropical circulation [Journal Article]. *Journal of Climate*, *20*(17), 4316-4340. Retrieved from `<Go to ISI>://WOS:000249237700002` doi: 10.1175/jcli4258.1

Wall, C. J., Hartmann, D. L., & Norris, J. R. (2019). Is the net cloud radiative effect constrained to be uniform over the tropical warm pools? [Journal Article]. *Geophys. Res. Lett.*, *46*(21), 12495-12503. doi: 10.1029/2019gl083642

Wing, A. A. (2019). Self-Aggregation of Deep Convection and its Implications for Climate. *Current Climate Change Reports*, *5*. Retrieved 2020-01-24, from `https://www.readcube.com/articles/10.1007/s40641-019-00120-3` doi: 10.1007/s40641-019-00120-3

Wing, A. A., Emanuel, K., Holloway, C. E., & Muller, C. (2017). Convective Self-Aggregation in Numerical Simulations: A Review. *Surveys in Geophysics*, *38*(6). Retrieved 2020-04-03, from https://link.springer.com/epdf/10.1007/s10712-017-9408-4 doi: 10.1007/s10712-017-9408-4

Wood, R., & Bretherton, C. S. (2006, December). On the Relationship between Stratiform Low Cloud Cover and Lower-Tropospheric Stability. *Journal of Climate*, *19*(24), 6425–6432. Retrieved 2020-04-02, from http://journals.ametsoc.org/doi/10.1175/JCLI3988.1 doi: 10.1175/JCLI3988.1

Yano, J. I., Grabowski, W. W., & Moncrieff, M. W. (2002). Mean-state convective circulations over large-scale tropical sst gradients [Journal Article]. *J. Atmos. Sci.*, *59 (9)*(MAY 2002), 1578-1592.

Zhang, C., McGauley, M., & Bond, N. A. (2004, January). Shallow Meridional Circulation in the Tropical Eastern Pacific. *Journal of Climate*, *17*(1), 133–139. Retrieved 2022-10-29, from https://journals.ametsoc.org/view/journals/clim/17/1/1520-0442$_2004_017_0133_smcitt_2.0.co_2.xml$ (Publisher: American Meteorological Society Section: Journal of Climate) doi: 10.1175/1520-0442(2004)017¡0133:SMCITT¿2.0.CO;2

Zhang, C., Nolan, D. S., Thorncroft, C. D., & Nguyen, H. (2008a, July). Shallow Meridional Circulations in the Tropical Atmosphere. *Journal of Climate*, *21*(14), 3453–3470. Retrieved 2022-10-25, from https://journals.ametsoc.org/view/journals/clim/21/14/2007jcli1870.1.xml (Publisher: American Meteorological Society Section: Journal of Climate) doi: 10.1175/2007JCLI1870.1

Zhang, C., Nolan, D. S., Thorncroft, C. D., & Nguyen, H. (2008b, July). Shallow Meridional Circulations in the Tropical Atmosphere. *Journal of Climate*, *21*(14), 3453–3470. Retrieved 2024-02-20, from https://journals.ametsoc.org/view/journals/clim/21/14/2007jcli1870.1.xml doi: 10.1175/2007JCLI1870.1

Zhou, C., Zelinka, M. D., & Klein, S. A. (2016, December). Impact of decadal cloud variations on the Earth's energy budget. *Nature Geoscience*, *9*(12), 871–874. Retrieved 2020-02-21, from https://www.nature.com/articles/ngeo2828 doi:

10.1038/ngeo2828

Zhou, W., & Xie, S.-P. (2019, September). A Conceptual Spectral Plume Model for Understanding Tropical Temperature Profile and Convective Updraft Velocities. *Journal of the Atmospheric Sciences*, *76*(9), 2801–2814. Retrieved 2021-02-17, from `https://journals.ametsoc.org/view/journals/atsc/76/9/jas-d-18-0330.1.xml` doi: 10.1175/JAS-D-18-0330.1